Early grinding wheels – millstones on Stanage Edge, Peak District, England.

Then the Philistines seized him, gouged out his eyes and took him down to Gaza. Binding him with bronze shackles, they set him to grinding in the prison.

Judges 16:21

King James Version

MODELING OF THE FORCES IN GRINDING
FROM GRINDING WHEEL TOPOGRAPHY

Thesis submitted to Trinity College Dublin for the degree of doctor of philosophy.

by

Jeffrey Kavanaugh Badger

22 October 1999

Department of Mechanical and Manufacturing Engineering

Trinity College

Dublin, Ireland
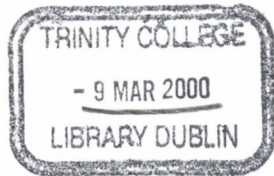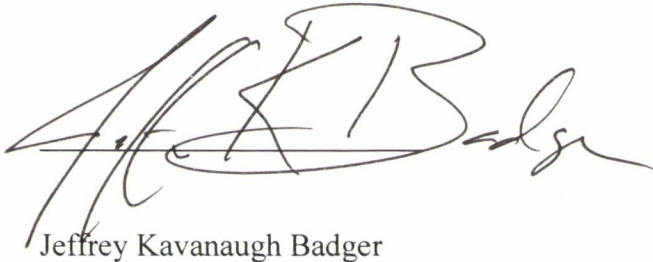
DECLARATION

This thesis has not been submitted as an exercise for a degree at any other university. Except where otherwise stated, the work described herein has been carried out by the author alone.

This thesis may be borrowed or copied upon request with the permission of the librarian, Trinity College, University of Dublin. The copyright belongs jointly to the University of Dublin and Jeffrey Badger

Jeffrey Kavanaugh Badger

22 October, 1999

ACKNOWLEDGEMENTS

I would like to thank Dr. Andrew Torrance for teaching me the finer points in grinding and especially for his words of wisdom both in and out of the laboratory.

I would like to thank Ge Wang for his comradeship and Conor McCormick for his friendship.

Much thanks goes out to all the partners in the Brite-Euram consortium, particularly Peter Ward of Dormer Tools.

Most importantly, I would like to thank my mother and father for their support in all my endeavors.

PREFACE

As the world becomes more industrialized and competition for fast, high quality production increases, the need to obtain faster manufacturing processes, while simultaneously increasing product quality, becomes increasingly important. To accomplish this, an increased understanding of the mechanics of the processes is necessary.

Of all the machining processes in use today, grinding is certainly the least understood. It has commonly been believed that, because of the complexities involved in grinding with its large number of seemingly random cutting events and their irregular geometry, any attempt to analyze the mechanics of grinding is, at the very least, an extremely complicated task. Consequently, there is a large mystique that still surrounds the grinding process.

As a result, engineers and technicians have largely relied upon rules of thumb, anecdotal observations and trial and error in their approach to grinding. The numerous variables involved such as dressing lead, dressing depth, wheel type, wheel grade, grain size, table speed, depth of cut, wheel diameter, workpiece properties, coolant type, coolant flow, *etc.* make determining the optimum conditions in grinding a formidable task.

Hitherto, models of the mechanisms of wear in the grinding process have typically been extensions of the two-dimensional chip formation cutting models or three-dimensional models with significant assumptions of the process – or they have been based on empirical measurements for a given set of conditions. Excellent work has been done in modeling the mechanisms of grinding. However, the numerous assumptions that are made sometimes do not reflect an accurate representation of what is actually occurring at the grit/workpiece interface.

The work presented in this thesis describes the development and application of two models of abrasion to grinding, one two-dimensional model based on slip-line fields and one three-dimensional model based on pyramidal indenters.

These two models can be used to predict the forces generated in grinding and to calculate theoretical grinding charts. The first model is based on Challen and Oxley's two-dimensional plane-strain slip-line field theory [1]. The second model is based on Xie and Williams's three-dimensional, pyramid-shaped asperity quasi-upper-bound model [2,3,4]. Both models use a distribution of cutting slopes based on surface profiles taken from the grinding wheels.

Comparisons are made between the predicted forces from each model and the measured forces from grinding experiments. Observations are made between the wear of the wheel and the changes in the topography. The correlation between the theoretical forces from both models and the experimental forces from grinding tests was satisfactory. The most accurate predictions were achieved with the three-dimensional model.

In addition, predictions were also made for forces published previously in the literature by developing a dressing model of grit fracture to predict the wheel topography. Lastly, a criterion was developed for quantifying the sharpness of the grinding wheel.

As opposed to other models, which usually define distinct regimes of wear as either/or scenarios of cutting, rubbing or plowing in two or three dimensions on an initially flat surface, the three-dimensional model presented here describes the mechanics of metal removal as a unique single regime of mixed mechanisms of metal deformation in three-dimensions while taking into account the strain hardening of the workpiece and the overlapping wear tracks that occur.

The higher accuracy of the three-dimensional model is attributed to the fact that it is a more realistic representation of the geometry and the mechanisms that occur during grinding and that it takes into account the simultaneous cutting, rubbing and plowing of the workpiece and the presence of overlapping wear tracks.

The primary assumptions and simplifications of the three-dimensional model are the simplified indenter geometry, the effect of high temperatures and high strain rates on hardness, the consideration of stain-hardening and the interfacial film strength. In addition, the model has not been proven on more ductile materials. These assumptions are addressed in the thesis.

This thesis explains the development and the application of the models and experimentally assesses their validity. The author is satisfied with the results – particularly of the three-dimensional model – and believes the work presented here to be a valuable addition to the understanding of grinding and a valuable tool to the grinding engineer.

TABLE OF CONTENTS

LIST OF FIGURES

LIST OF TABLES

NOMENCLATURE

a	half scratch width
a_{diam}	tip radius of the diamond
a_c	grinding in-feed
a_d	dressing in-feed
A%	percentage wear flat area in wheel
A_f	projected area of crushed grits.
A_p	projected area of pointed grits
A_{ridges}	Area displaced to side ridges
A_{total}	Total area of undeformed chip
b	constant in hyperbolic profile fit
b_w	cutting width of grain
b_a	fraction of wheel surface in contact with workpiece
c	constant in hyperbolic profile fit
C	$\dfrac{42\sigma_c r s_d}{F_0 \sqrt{a}}$
C'	Constraint factor
d_{grit}	distance between grits
d	scratch depth
d^*	depth
d_w	depth into wheel from peak asperity
d_p	minimum distance between adjacent asperity peaks
D_e	equivalent diameter $[1/(1/D_w+1/D_s)]$
$D_{g,mean}$	mean grit diameter
D_p	degree of penetration
D_{wheel}	wheel diameter
D_{work}	workpiece diameter for cylindrical grinding
$e_{0.1}$	specific energy when h_{eq}=0.1
e	abrasive efficiency – K/K_{max}
f	τ/k, the ratio of the shear strength of the lubricant film to the shear strength of the workpiece

f^H	τ/H, the ratio of the shear strength of the lubricant film to the hardness of the workpiece
f	force exponent in grinding chart
f_g	fraction of the grits missed by the diamond
f_n	normal force on grit
f_s	fraction of grits surviving one pass of the dressing diamond
F_0	characteristic strength of the bond
F_1	intercept on grinding chart
F_n	normal grinding force
$F_{n,grit}$	normal grinding force on a single grit
F'_n	normal grinding force per unit width
F_t	tangential grinding force
$F_{t,grit}$	tangential grinding force on a single grit
F'_t	tangential grinding force per unit width
g	gravity constant
h	depth of penetration
h'	pre-existing ridge height
h_{eq}	equivalent chip thickness
H_b	bulk hardness of workpiece
H_s	surface hardness of workpiece
I	statistical factor
j	number of passes of dressing diamond
k	shear strength
k_s	shear flow stress
K	specific wear rate
K_{max}	maximum abrasive wear coefficient
l	dimensionless distance between adjacent tracks
l_a	geometrical length of arc of cut
l_t	dimensionless distance between adjacent tracks for transition from plowing to cutting
L	distance between adjacent tracks
$L_{scratch}$	length slid by scratch
m	Weibull modulus of bond strength

n	areal density – number of asperity summits per unit area
n_0	number of grits per unit area in the wheel surface
n_d	linear density – number of asperity peaks per unit length
N	normal load of asperity
N_s	number of wheel passages to remove a depth d
p	average pressure over arc of cut
P	power consumed
$P(s)$	normal probability distribution function
P_n	normal stress on contact face of grit
P_t	tangential stress on contact face of grit
Q_w	metal removal rate
r	average grit radius
$r_{grit-tip}$	radius of the grit tip
R_a	CLA roughness of workpiece
R_{qs}	RMS slope of the grits in contact
s	mean slope of asperity, tan α
s	mean attack angle
s_d	dressing lead
s_0	slope of crushed grit surface
s_m	RMS slope of grit facets
S	structure number of wheel
t	depth of penetration into workpiece
V_s	wheel speed
V_w	work speed
V_g	volume fraction of grit in the wheel
$\dot{V}'$	wear equation per unit time
W	wear volume
Z'	specific metal removal rate
Z_g	metal removal rate per grit
ε	strain
$\dot{\varepsilon}$	strain rate
α	attack angle, slope of cutting asperity
α_{NR}	negative rake angle

α_{trans}	transition angle from wave formation to cutting in orthogonal models, transitional angle from plowing to cutting in oblique models
$\alpha_{p, trans}$	transitional attack angle from plowing to cutting regardless of dimensionless distance between adjacent tracks
β_{eff}	cutting efficiency ratio
β	angle in pyramidal indenter
σ_c	crushing strength of the grit
α_{NR}	negative rake angle of cutting asperity
α_{qs}	RMS slope of attack angle for pyramid-shaped asperity
Δt	change in time
σ_y	yield strength of workpiece
ψ	semi-angle of dressing diamond
λ	wavelength corresponding to the spacing of the grits
τ	shear strength of lubricant film at interface
τ	distance mean line of the surface below the top of the side ridges
τ_f	shear strength of the boundary film
τ_0	true shear strength
μ	ratio of tangential force to normal force
μ_0	coefficient of friction on the grit rake face

CHAPTER 1. INTRODUCTION.

1.1. Overview and Scope of Present Investigation.

Overview

Grinding is an extremely complex process of abrasion. There are a huge number of variables that can affect grinding which include but are not limited to:

- Abrasive type
- Grit size
- Bond type
- Bond strength
- Grit friability
- Dressing diamond radius
- Dressing depth
- Dressing lead
- Depth of cut

- Wheel speed
- Work speed
- Wheel diameter
- Workpiece hardness
- Workpiece ductility
- Workpiece carbide structure
- Coolant type
- Coolant speed
- Coolant flow

In practice, engineers and technicians largely rely on anecdotal observations, rules of thumb and trial and error to determine the correct choice of grinding parameters. This is partly due to the seemingly random nature of the grits in the wheel and the huge number of interactions in grinding.

For example, if we consider the grinding of a flute in a large diameter drill, we have an area of approximately 5400 mm^2 in the grinding zone arc of cut, a density of approximately 2 asperity cutting points per square millimeter on a machine running at 50 revolutions per second. From this we can calculate

$$5400 \bullet 2 \bullet 3000 = 540,000 \text{ possible abrasive interactions per second.}$$

(parameters used: drill diameter=50 mm, wheel diameter=400 mm, depth of cut=15 mm, wheel RPM=3000, asperity density = 2 /mm^2 from [5])

Clearly, the grinding process is a complicated one and a better understanding of the complexities of the process would be an enormous scientific and economic benefit.

One of the primary difficulties encountered in grinding is determining how a given type of grinding wheel, dressing condition and set of workpiece material properties will affect the forces and power generated. There are two main methods of presenting the results of grinding measurements. The first was used by Lindsay [6,7,8,9]. Here the independent variable is taken to be the normal force between the wheel and the workpiece and the other variables (metal removal rate, wheelhead power, surface finish, wheel wear) are plotted against it to give a "system characteristic chart". For a specific set of conditions (wheel and work speeds, wheel type, coolant type, workpiece material) the results can be fit to straight lines. The gradients of these can be used as the basis of semi-empirical equations for controlling the process. The primary disadvantage of this method is that tests are run on an extremely narrow set of grinding conditions so that separate charts must be made to cover all possible combinations for a given workpiece.

A second method is the "equivalent chip thickness" method used by Peters *et al.* [10,11]. Here the normal and tangential forces, the surface roughness and the grinding ratio can be plotted against the equivalent chip thickness to give a straight line on log-log scale [12]. Peters defined the equivalent chip thickness as

$$h_{eq} = \frac{a_c \cdot V_w}{V_s} \tag{1}$$

where h_{eq} is the equivalent chip thickness measured in μm, a_c is the depth of cut measured in μm, V_w is the work speed measured in m/s, and V_s is the wheel speed measured in m/s [11]. The relation between the normal and tangential forces per unit length in grinding (F'_n and F'_t) and h_{eq} can be represented by:

$$F'_n = C_1 \cdot h_{eq}^f \tag{2}$$

$$F'_t = C_2 \cdot h_{eq}^f \tag{3}$$

2

where the constants C_1 and C_2 are the intercept of the graph on log-log scale and f, the slope of the graph on log-log scale, can be considered the grindability of the material. Malkin [13, 14] stated that the maximum energy that can be absorbed by the chips in grinding is the melting energy which is usually small compared to the actual energy of grinding. The specific energy, e, measured in J/mm^3, is defined as

$$e = \frac{P}{Q_w} \tag{4}$$

where P is the power consumed in grinding measured in Watts and Q_w is the volumetric metal removal rate measured in mm^3/s [13]. As described by Peters *et al.*, as h_{eq} increases, the specific energy decreases because the grits dig deeper into the workpiece with a greater extent of cutting instead of rubbing and plowing which results in more efficient metal removal. The drawback of this empirical method is that there is an enormous number of parameters that can affect the forces. These include but are not limited to the wheel grade, the wheel grain type, grain size, the workpiece material, the grinding speed, the wheel speed, the dressing depth and the dressing lead – and grinding charts do not exist for every possible grinding scenario. The development of a realistic model of the mechanics of metal removal and the forces involved that would account for the peculiarities of the process would be of great assistance.

Measurement of forces and specific energies began in the 1950s [15,16] and showed that grinding specific energies were much larger than in other methods of metal cutting. Malkin discussed normal and tangential forces being composed of a cutting component and a sliding component – of which the sliding component depends on the friction at the interface and the extent of the development of wear flats at the tips of the grits [17]. Malkin also studied the relationship between the development of wear flats and increasing metal removal and how the development of wear flats affected the forces. The correlation between the geometry of the grain and the forces has been studied through single-grit tests [18] and the effect of wheel loading on forces has been studied using fiber optics [19]. McAdams measured the profile of abrasives to correlate their performance with the number of lands and voids present [20]. Shaw proposed a new grinding mechanism [21] in place of the classic chip

formation mechanism developed by Merchant [22]. Shaw likened the mechanism of grinding to an extrusion process rather than the usual process of chip formation by shearing. Both of these consider the mechanism of wear as a single cutting tool with a large negative rake angle – in contrast to Malkin's use of percentage wear flat area. Although apparently different, Malkin's wear flat area could be considered to be grits with small rake angles at the grain tips. Malkin's relationship between forces and wear flat area has become a classic piece of work. Nevertheless, it is still particular to a given set of wheel, workpiece, dressing and grinding conditions. The numerous pieces of work that have evolved from Merchant's chip formation model go a step farther, relating abrasive slopes and material properties. Yet they do not account for the complicated nature of wheel slopes, the relationship between wear and wheel slope – and wheel slope and forces – nor the complex interaction of cutting, rubbing and plowing that is present.

Considering this, the development of a quantitative model that realistically describes the mechanisms of grinding based on the wheel topography and can relate grinding forces and power with the grinding parameters and the dynamic wheel topography would be of great assistance.

Scope of Present Investigation

A starting point, first published by Brenner and Torrance [23] and Badger and Torrance [24] for grinding, is a model that represents the deformation imposed on the workpiece by the grit with a set of three slip-line fields: one for cutting, one for rubbing and one for plowing. Challen and Oxley have published such a set of slip-line fields [1]. This has been exploited successfully to predict friction and wear coefficients by Lacey and Torrance for ordinary sliding [25] and by Torrance and Buckley for abrasion [26]. The abrasion model was then simply adapted to predict forces in grinding as shown by Brenner and Torrance [23] and Badger and Torrance [24]. The main disadvantage with this approach is that plane-strain is assumed, which will not generally be realistic. This is balanced by the advantage of having a model of all three contact mechanisms where the interaction of the grit with the workpiece depends only on its slope and the coefficient of friction. The distribution of grit slopes can be measured from a profile of the wheel and, using the rules given by Torrance and Buckley [26], the proportion of cutting, rubbing and plowing can

be found. Application of the three contact models then gives forces and metal removal rates, which are presented as grinding charts. A comparison of predictions of the model to experimental results from grinding tests on bearing steel workpieces was given by Badger and Torrance [24]. This therefore required a method of measuring grit slopes for its application which was achieved through profilometry. The results were satisfactory, but the assumption of plane-strain along with several assumptions of material properties limited its practicality. The mechanism of wear is not governed by an either/or situation – cutting or rubbing or plowing – in two dimensions. More realistically, the mechanism of wear is more complex, where the grit may rub the workpiece within the elastic zone of the material, plow material to the sides or cut material to the sides or front of the grit in the form of one or two chips – with the possibility of two or all three interactions occurring at once.

Xie and Williams published a three-dimensional model of abrasion that assumes a single, regular pyramid-shaped asperity with metal removal by either cutting, plowing or rubbing – or all three simultaneously – depending on the attack angle and the coefficient of friction [2,3,4]. Using a quasi-upper-bound method of energy minimization, they fit the results to a parametric equation. The three regimes of contact were given as elastic shakedown, plowing and cutting. Elastic shakedown was defined as the rubbing of the grit against the interface with no permanent plastic deformation. Plowing was defined as the generation of ridges to either side of the grit without metal removal. Cutting was defined as the generation of side ridges and the removal of material from side ridges in the form of a prow. Moreover, even within the cutting regime, all three interactions were allowed to occur as material was simultaneously rubbed in the contact, pushed forward in front of the asperity in the form of a wave, plowed to the side, and removed to either or both sides in the form of a chip. This depended on the attack angle, the lubrication, the distance between adjacent overlapping tracks and the material properties of the workpiece. They applied a Gaussian distribution to the heights of the abrasive peaks and successfully predicted friction and wear coefficients for several sets of previously published experimental results of abrasion [4].

It would be possible to use the techniques of Brenner and Torrance [23] and Badger and Torrance [24] for measuring wheel topography and, instead of applying the two-

dimensional slip-line field model of abrasion, to apply the three-dimensional model of Xie and Williams [2,3,4] to achieve a more realistic model of the mechanisms of grinding.

This thesis proposes such an approach, applies it and verifies it with experimental measurements of forces in grinding. It is also used to predict forces previously published in the literature by applying a model of dressing to predict the wheel topography. The two-dimensional model is also used to predict forces and comparisons are made between the results from the 2-D model and the 3-D model. Lastly, a method for quantifying the sharpness of the wheel is proposed.

1.2. Introduction to Grinding.

1.2.1. Wheel Wear in Grinding.

A grinding wheel is composed of abrasive grits, bonding matrix and voids. The naturally occurring materials, aluminum oxide and silicon carbide, are the most commonly used types of grits. Cubic boron nitride (CBN), a synthetic material first synthesized in the 1950's, has a very high hardness and wear resistance but its high cost places limitations on its use. Vitreous bonds are used in a large percentage of grinding wheels. Resinoid bonds are used in heavy-duty operations where large loads are present because of their high toughness and ability to withstand high wheel speeds. Rubber and metal bonds are also used in certain applications.

Wheel wear in grinding and in dressing occurs by three modes – bond fracture, grain fracture or attritious wear [13]. This is illustrated in Figure 1.1.
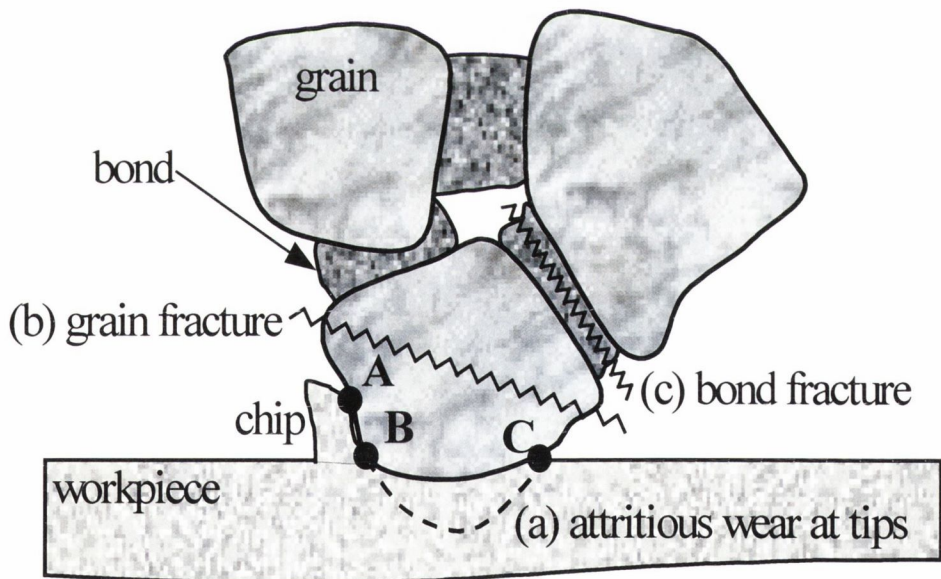
Figure 1.1. Wheel wear in grinding.

Harder grits tend to suffer less attritious wear at the tips and wheel wear is more likely to occur by bond fracture than by grit fracture. Grits that are more friable are more likely to suffer from grain fracture. Malkin [17] found that as the amount of

material removed during grinding increased, the extent of attritious wear, or wear flat area, increased leading to larger forces and larger specific energies. If the forces become large enough, the stresses on the grit can cause grit fracture or bond fracture. This leads to re-sharpening of the wheel with the exposure of new, sharp cutting edges. Higher grade wheels have a larger percentage of bonding matrix meaning that the grits are held more strongly. This leads to a stronger wheel that can maintain form more effectively but means that attritious wear can increase to a more detrimental level before forces are large enough to cause bond fracture and re-sharpening of the wheel [17, 27].

1.2.2. Wheel Dressing.

During single-point wheel dressing, a diamond is passed axially along the wheel while contacting the grits to impose a topography on the surface wheel that will lead to effective grinding. The parameters used during dressing that affect the topography are the depth of cut (a_d), the dressing lead (s_d) and the diamond radius (a_{diam}). As the diamond moves across the grinding wheel, it would appear to cut a helix in the wheel of radius a_{diam} at a distance of s_d between tracks at a depth a_d into the wheel as shown in Figure 1.2. There is general agreement [13] that increasing the dressing depth of cut increases the sharpness of the grinding wheel which leads to lower forces during grinding and larger surface roughnesses on the workpiece. As the dressing diamond wears with repeated dressing, the tip tends to become blunter with a larger radius of curvature. Some have argued that a larger tip radius should produce larger stresses on the grits causing more bond fracture and leading to a sharper wheel. However, in practice, the reverse is found to be true [13]. There is also some disagreement about the influence of the dressing lead. Verkerk [28] and Malkin [29] believe that dressing lead has a greater effect than dressing depth because of an increase in the forces on the grits – and hence produces a sharper wheel. However, Pande and Lal [31] argue that larger leads can give a blunter wheel since the dressing tool will miss some of the grits as it traverses the wheel. This difference of opinion may be due to the different ranges of leads, depths and grit sizes studied by each group. Pattinson and Chisholm [32] found that a large dressing lead increased the wheel wear rate during grinding. However, after the initial wear

stage, the wear rate was independent of dressing lead. Rowe *et al.* [33] found that the power consumed in grinding quickly drops and then gradually increases with metal removal until a steady-state value is reached which is independent of dressing conditions. This indicates that a "natural topography" of the wheel will eventually be reached with wear of the wheel during grinding. Pacitti and Rubenstein [34] found that larger dressing depths reduced wheel wear. The shape of the dressing diamond is very important. Verkerk [35] found large differences in wheel wear rates for changes in diamond shape. Rowe *et al.* [33] noted that small changes in diamond shape are significant and make predictions of grinding behavior very difficult. Whether achieved through changes in dressing depth, dressing lead or diamond radius, there is general agreement that a sharper wheel typically leads to lower forces and temperatures during grinding and a higher workpiece surface roughness.
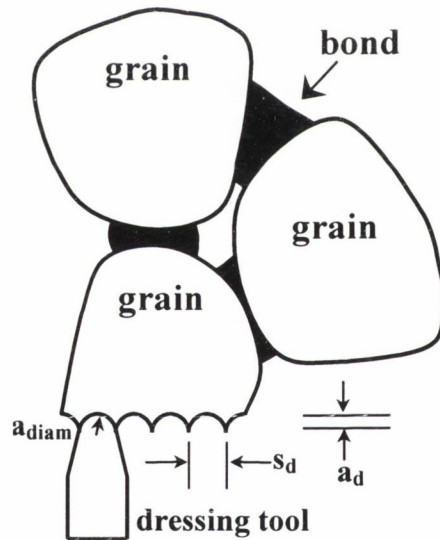
Figure 1.2. Simplified model of wheel wear.

The helices caused by the dressing lead have been identified experimentally from axial profiles of dressed wheels by Pandit and Sathyanarayanan [36] who calculated the large and small wavelengths from profiles. They stated that the large wavelength represented the spacing of the grits and found that

$$\lambda = 1.414 \cdot D_{g,\text{mean}} \tag{5}$$

where λ is the long wavelength and $D_{g,mean}$ is the mean grain diameter. They found that the small wavelength represented the cutting edges on the grain.

However, this method of describing wheel dressing appears a bit simplistic as wheel wear in dressing should occur through brittle fracture as the ceramic grains have very high yield strengths. A ductile mode of grit wear and removal does not seem realistic in light of the non-ductile material properties of the wheel and bond. This is corroborated by Malkin who dressed vitrified alumina wheels and collected the particles that were worn from the wheel during dressing [17, 27]. Malkin passed the dressed particles through a succession of sieves to determine the distribution of particle sizes. He found that the largest mass of particles had diameters that were only slightly smaller than the original mean diameter of the grains in the wheel. He found that particle diameters were much larger than the dressing in-feed and concluded that bond fracture was the dominant mode of wheel wear in dressing. Bond fracture was found to be less prevalent in harder wheels because of the higher percentage of binding matrix resulting in a corresponding increase in the probability of grain fracture.

Peklenik measured the forces required to dislodge grains by rotating the wheel at low speeds through a diamond tip at a depth equivalent to the mean grain [37]. For a range of wheel hardness values and mean grain diameters he determined the distribution of dislodgment forces and calculated the corresponding values for mean and standard deviation. As expected, a higher grade of wheel hardness (corresponding to larger percentages of bond volume) coincided with larger forces. In addition, larger mean grit diameters coincided with higher forces.

Figure 1.3 shows SEM photos of a 60 grit size ($D_{g,mean}$=254 μm) H-grade vitrified alumina wheel immediately after dressing. The large diameter of the grits indicates that the dominant mode of wheel wear is bond fracture.
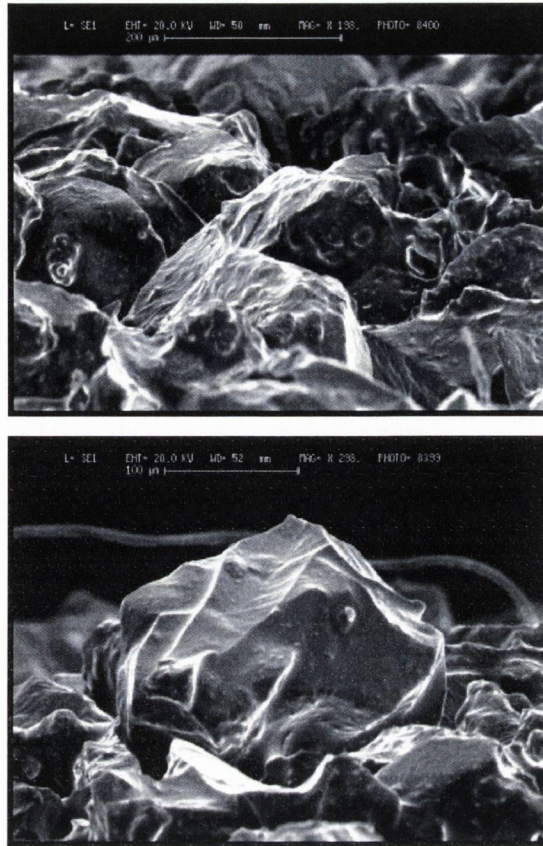
Figure 1.3. SEM photos of grits in a vitrified alumina wheel (WA 60 HV)

1.3. Forces, Friction and Wear Mechanisms in Grinding.

Material removal during abrasive processes occurs as the asperities of the harder material contact the softer material and the stresses increase until they exceed the yield stress of the material. The way the grit and workpiece interact depends on the geometry of the grit, the geometry of the workpiece, the material properties of both, the extent of lubrication between the two and the speed and geometry at which they contact. For grinding, there are several methods by which to study the mechanisms behind the grit/workpiece interface. One is to examine the swarf generated in grinding under a microscope to give clues as to the mechanism behind the material removal as was done by Wetton [38]. Komanduri and Shaw [39] examined the swarf generated from grinding hard tool steel and found chips of less than 1 μm thickness and platelets. The presence of the chips indicated that grinding causes metal removal through a process of cutting similar to that of turning and the presence of platelets

11

indicated metal removal from a process of extensive plowing. Another method is to measure the power required in the process over a range of conditions such as workpiece type, dressing conditions, *etc*. Another method is to measure the forces present in grinding since forces can be related to power by the equation:

$$P = F_t(V_s \pm V_w) \approx F_t \cdot V_s \qquad (6)$$

where P is the power consumed, F_t is the tangential force, V_w is the work speed and V_s is the wheel speed. Since $V_s >> V_w$ we can neglect V_w to arrive at the power as a function of the tangential force and the wheel speed. Forces were measured as early as the 1950's by Backer *et al.* using a resistance strain gage dynamometer [16]. On a more microscopic level, forces can also be measured by experiments using a single grit or grit-shaped tool. This gives a more precise picture of conditions in actual grinding.

Since the forces measured can be directly related to the grinding power, the temperatures generated, the specific energies and the overall effectiveness of grinding, a greater understanding of the mechanics involved at the grit/workpiece interface is necessary.

1.3.1. Boundary Friction.

An important method of defining the forces generated between moving surfaces is the ratio of the shear strength of the interfacial contact to the shear yield stress of the material. This is also known as the friction factor and is defined as:

$$f = \frac{\tau}{k} \qquad (7)$$

where

$$0 \le f \le 1$$

and τ is the shear strength of the lubricant film at the interface and k is the shear flow strength of the deforming material [1]. In some literature, f is defined in terms of the hardness. This can be written this as

$$f^H = \frac{\tau}{H} \qquad (8)$$

where H is the hardness of the deforming material. The difference between the two definitions can be easily resolved since, for most metallic materials, these two quantities are related by [4]

$$H = 3\sqrt{3}k \approx 5k. \qquad (9)$$

Briscoe et al. [40] found that, for organic materials, the shear strength of the boundary film increased with contact pressure (P). For calcium and copper stearate, it was found to be constant at pressures below 50 MPa. This explains why the friction of solids lubricated with boundary films of long chain molecules does not depend significantly on the hardness of the solids. Black et al. [41] showed that for pressures greater than 100 MPa, the relationship between shear strength and pressure was nearly linear and can be expressed as:

$$\tau = \tau_0 + \mu_0 P \qquad (10)$$

where τ_0 is the true shear strength of the material and μ_0 is a constant so that the lowest shear strength found corresponded to a true shear strength of the layers of the unconfined material [41]. Therefore, the frictional force is a result of the shearing of the film. They suggested that the increased pressure caused the molecular chains to be squeezed closer together so that μ_0, the shear involved in sliding, increased the force necessary to produce sliding at the higher pressures. Tabor [42] successfully explained Briscoe et al.'s findings in terms of molecular processes.

1.3.2. Rubbing, Cutting and Plowing.

Malkin [13,17] divided the forces in grinding into two categories: the forces generated from chip formation and the forces generated from sliding. This is written as:

$$F_{t,\ total} = F_{t,cutting} + F_{t,\ sliding} \tag{11}$$

$$F_{n,\ total} = F_{n,cutting} + F_{n,\ sliding} \tag{12}$$

where F_t is the tangential force and F_n is the normal force. Malkin stated that at zero wear flat area, the sliding forces are zero and the grinding forces are equal to the cutting force component. Others studying wear flat area [43,44] have included the force due to plowing which was small and not included in earlier models so that

$$F_{t,\ total} = F_{t,cutting} + F_{t,\ sliding} + F_{t,\ plowing} \tag{13}$$

$$F_{n,\ total} = F_{n,cutting} + F_{n,\ sliding} + F_{n,\ plowing}. \tag{14}$$

The sliding forces (also called the rubbing forces), $F_{t,sliding}$ and $F_{n,sliding}$, were considered to be the primary cause of grinding instability as it increased with increasing attritious wear and wear flat area [43]. Werner [49] developed an expression for the normal force as a function of the static cutting edge density, the ratio of work speed to wheel speed, the depth of cut, the equivalent wheel diameter and a "loading coefficient". Younis et al. [19] applied a fiber-optic technique to measure the loaded area of the wheel to predict forces using the equations of Werner. They described a regime of contact where in the first stage of contact the only deformation of the workpiece is elastic. As the cutting edge traverses the surface, the deformation continues, while the normal and tangential forces steadily increase until a transition to plowing occurs. If the deformed surface ahead of the cutting grit edge comes into contact with the cutting edge profile, then a transition

14

from plowing to chip formation occurs. Therefore, a single grit can cause all three regimes of contact to occur within a single contact.

Malkin related the proportion of sliding forces and cutting forces to the percentage of wear flat area of the grits on the wheel seen under a microscope [17,27]. As stated previously, attritious wear accounts for only a small fraction of overall wear of the wheel – yet it has been found to be very influential in terms of grinding power, forces, heat generation and surface finish. Malkin found that the grinding force increased linearly with wear flat area until finally reaching a critical value where the forces increased dramatically, usually coinciding with the onset of workpiece burning. As stated by Rowe *et al.* [50], because the relative velocity between the grain and the chip at the interface BC (Figure 1.1, page 7) is much lower than the relative velocity along AB, it is therefore assumed that the chip-grain energy is relatively small. Therefore, it is the energy and heat generated directly at the workpiece surface at the face AB that is most important. Rentsch and Inasaki modeled the abrasive process using dynamics at a molecular level [51].

Lastly, it should be noted that both Malkin's wear flat area and the numerous other models which utilize rake angles assume that either cutting or rubbing or plowing occur for a given grit/workpiece interaction – an either/or scenario. In fact, it is likely that, as stated by Younis *et al.* [19], one, two or all three interactions may occur simultaneously. Malkin's wear flat area is based on experimental work while the chip formation/rubbing/plowing models are based on theoretical applications.

1.4. Rigid-Plastic Models Based on Challen and Oxley.

Challen and Oxley published three slip-line fields to describe possible interactions of a hard wedge with a rigid-perfectly plastic solid [1] similar to the slip-line fields proposed by Green [52]. These three slip-line fields were described as "wave formation", "wave removal" and "chip formation". The independent variables used in the construction of the slip-line field are the asperity attack angle (α) and the interfacial film strength (f) as defined in Section 1.3.1 (page 12). Which type of field

is applicable is a function of the attack angle of the wedge and the shear strength of the interfacial film. Therefore, the friction is related by a single geometric parameter (α) and a single lubrication parameter (f). As applied to the abrasive process of grinding, wave formation can correspond to rubbing, wave removal can correspond to plowing and chip formation can correspond to cutting. Therefore, all three modes of contact as defined by Malkin and others (Section 1.3.2, page 14) can be defined by a slip-line field. For all models of plane-strain contact, the asperity/deforming material contact is assumed to be rigid-perfectly plastic.

1.4.1. Wave Formation.

The slip-line field for plane-strain wave formation and the corresponding hodograph (velocity diagram) is shown in Figure 1.4 from Challen and Oxley [1]. The hard asperity is assumed to be rigid so that the plastic deformation of only the deforming surface needs to be considered. Here a wave of plastically deformed material is pushed ahead of the asperity. The field is similar to those proposed by Green [52] for a weak junction, by Collins [53] for a rolling contact and by Johnson and Rowe [54]. The plastic region is bounded by the fan ABCDE so that it extends below the surface of the material. The angle η will in general be greater than the initial slope of asperities on the soft surface while α will remain unchanged.

The coefficient of friction can be calculated from the normal force (N) and the transversal force (F) acting on the hard asperity [1] according to

$$\mu = \frac{F}{N} = \frac{(A\sin\alpha + \cos(2\varepsilon - \alpha))ED \cdot k_a}{(A\cos\alpha + \sin(2\varepsilon - \alpha))ED \cdot k_a} \tag{15}$$

where,

$$A = 1 + \frac{\pi}{2} + 2\varepsilon + 2\eta - 2\alpha \tag{16}$$

$$f = \cos(2\varepsilon) \tag{17}$$

$$\alpha + \phi = \frac{1}{2}\arccos(f) \tag{18}$$

16

$$\eta = \arcsin\left\{\sin(\alpha)\sqrt{1-f}\right\} \qquad (19)$$

where f is defined as

$$f = \frac{\tau}{k}. \qquad (20)$$

For the wave model to be valid ϕ, the angle of the region of plastic deformation, must be positive so that material can flow into and out of the wave and therefore it follows that

$$\alpha \leq \eta \leq \frac{\pi}{4}$$

and

$$0 \leq \mu \leq 1.$$

Bowden and Tabor [55] treated adhesion and plowing separately and calculated the total coefficient of friction from the arithmetic sum of the parts resulting from adhesion and plowing. While this is probably acceptable for smooth surfaces, as pointed out by Tabor [42] a proper treatment should combine both mechanisms into a single plasticity model to allow for the interaction between them. This is achieved by Challen and Oxley [1] and thus combines the adhesion and plowing mechanisms which were previously treated separately [55].

As mentioned by Johnson [56], the value for μ when $\alpha=0$ can be considered the adhesion component of friction and that for $f=0$ the plowing component; then for very small values of α the combined coefficient of friction from the two can be taken as the summation of the two as assumed from earlier theories. This is no longer true as α increases and as the plastic work rises.
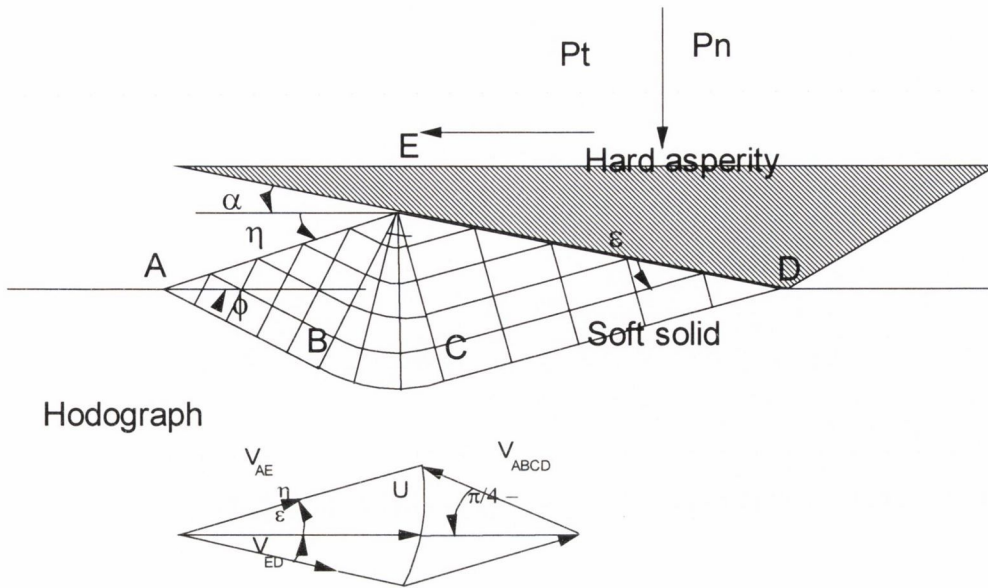
Figure 1.4. Challen & Oxley's slip-line field for wave formation.

If we apply shearing layers of the film from Section 1.3.1 ($\tau = \tau_0 + \mu_0 P$, page 12), this means that when $\alpha=0°$, $\mu= \mu_0$ [42]. Using a simple analysis based on an inclined plane model, Black showed that when $\alpha \neq 0°$

$$\mu=\tan(\alpha + \arctan \mu_0) \tag{21}$$

Therefore, for the wave model, the coefficient of friction is predicted from the geometry of the asperity, the material properties of the deforming material and the extent of lubrication at the interface. It is therefore predicted to increase with increasing α and f. The basic laws of friction are satisfied since F is proportional to N and the friction coefficient is independent of the area of contact and $\mu=1$ when $\varepsilon=\alpha$.

1.4.2. Wave Removal.

For the wave removal model shown in Figure 1.5, the wave is no longer pushed along ahead of the asperity but is torn off. It applies at larger values of α than the

wave formation model or at larger values of f corresponding to poor lubrication. The wedge is effectively "ripped away" from the bulk material. It as applicable when

$$\eta \geq \frac{\pi}{4}$$

and

$$\phi \leq 0$$

In this range the deformed material must be removed and a wear particle produced. Estimates have been made of the forces and corresponding coefficients of friction in this range by assuming that the deformation that occurs before fracture can be characterized by an increasing value of η as shown experimentally by Green [52]. Here AD is assumed to remain parallel to U during deformation with the only change in the external shape of the deforming region occurring from an increase in η with EA remaining straight. Therefore, the slip-line field consists of two regions of straight slip-lines without the centered fan of the wave model. Instead, the two regions meet at a line of stress discontinuity CE where there is a jump in the hydrostatic stress. Again, the independent variables are α and f. However, f now represents the ratio of the resolved shear stress at DE to the shear flow stress k as there is no sliding along DE. The coefficient of friction can be written as

$$\mu = \frac{\left\{1 - 2\sin\beta + (1 - f^2)^{1/2}\right\}\sin\alpha + f\cos\alpha}{\left\{1 - 2\sin\beta + (1 - f^2)^{1/2}\right\}\cos\alpha - f\sin\alpha} \tag{22}$$
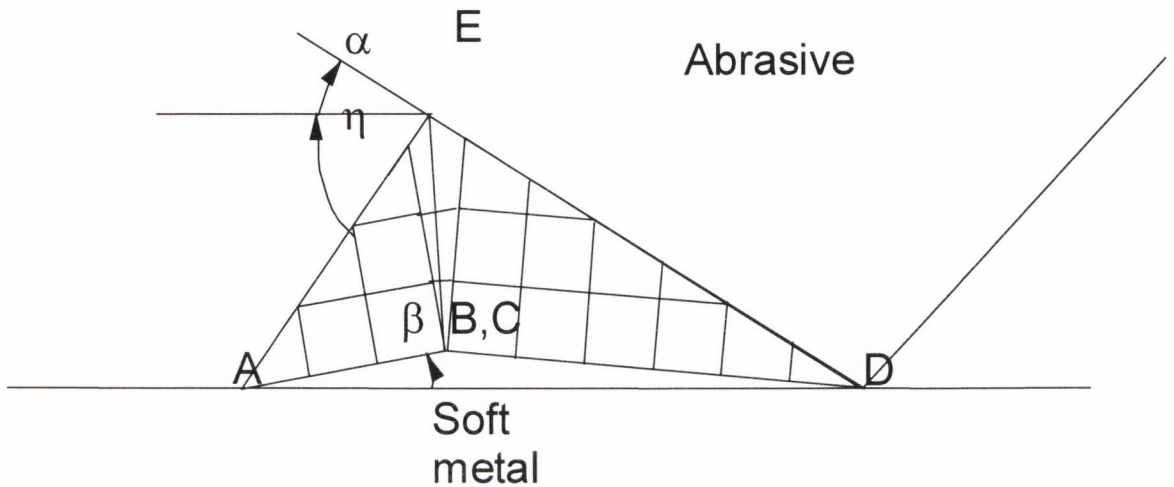
Figure 1.5. Challen & Oxley's slip-line field for wave removal.

The transition from wave formation to wave removal was addressed by Johnson both experimentally and analytically [56]. He considered a wedge penetrating a plane surface under an increasing normal load and examined how, as the wedge dug deeper, the normal force increased and was transferred from two faces onto one "bow wave" face of plastically deformed material until either a steady state wave developed or a wear particle resulted, depending on the value of f.

1.4.3. Chip Formation.

Modeling of the process of chip formation began in 1944 when Merchant [22] published his classic model where chip formation occurs by an intense shearing process in a thin zone with friction at the chip/tool interface as the chip slides up the tool. Typically, 75% of the energy is consumed in shearing and 25% of the energy is consumed in friction. In 1952, Backer *et al.* [16] used the basic chip-formation model for grinding and found stresses significantly higher, particularly at smaller undeformed chip thickness and its correspondingly higher specific energy – and from this the "size effect" theory was proposed. Although Merchant's model has been developed extensively over the years, the basic model is still considered to be a

reasonably accurate description of chip formation and has been applied to a variety of machining operations.

Challen and Oxley [1] proposed a slip-line field model for chip-formation which is illustrated in Figure 1.6. When $\alpha > \dfrac{\pi}{4}$, metal removal by means of cutting is possible when $\alpha > \dfrac{\pi}{8}$ if $f=0$. The friction coefficient by means of chip formation, applicable when $\phi > 0$, is given as

$$\mu = \cot(\vartheta - \phi) \tag{23}$$

where,

$$\tan \theta = 1 + 2\left(\frac{\pi}{4} - \phi\right) \tag{24}$$

$$\vartheta = \frac{\pi}{2} + \phi + \frac{1}{2}\arcsin(f \sin 2\vartheta) - \alpha \tag{25}$$
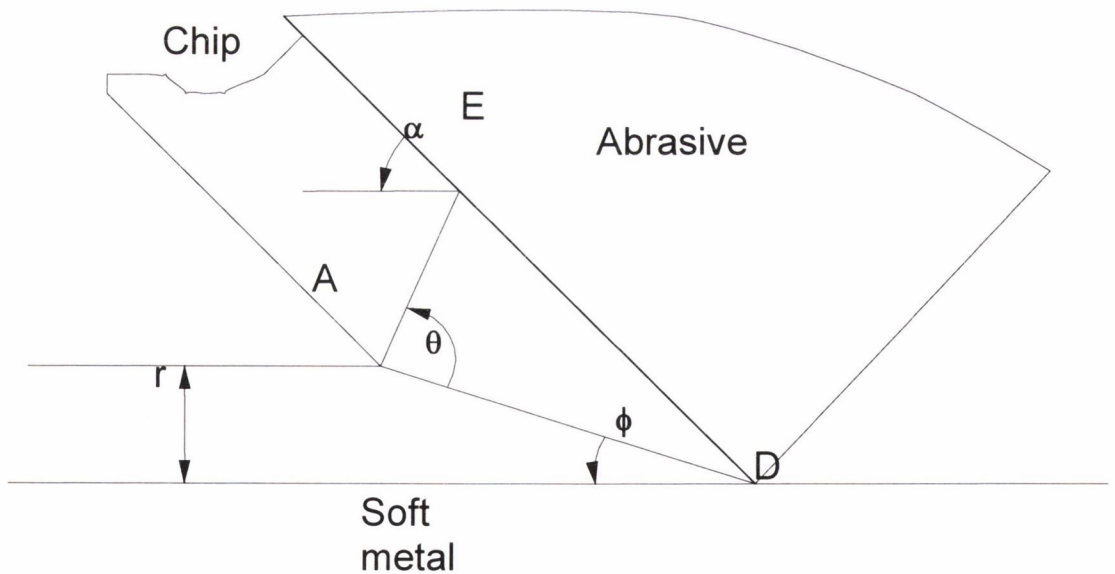
Figure 1.6. Challen & Oxley's slip-line field for chip formation.

21

1.5. Development of Challen and Oxley's Models.

The models of Challen and Oxley have been further developed to account for aspects that were not initially addressed and have been applied to several various types of abrasion. The dependence of preceding asperities, the measurement of the film strength of the lubricant, the possibility of low-cycle fatigue at small attack angles, the measurement of the attack angle for real abrasives, the effects of strain-hardening of the deforming material and applications of the model to grinding have all been investigated.

1.5.1. Real and Apparent Contact – Sawtooth Wedges.

One disadvantage of the single fan fields presented here is that they assume that each individual wedge acts independently and is isolated from the others so that the deformation fields do not interact. This is correct at low loads where plastic deformation is small. However, at high loads the fields will start to overlap. Challen and Oxley [57] took this into account and modified the slip-line field for ratios of real to apparent contact area ranging from zero to one which increase with apparent contact pressure. The asperities on the hard surface were represented by a sawtooth form because of the effect of the overlapping asperities. Because of this, Challen and Oxley concluded that the real area of contact is many times smaller than the apparent area of contact.

1.5.2. Calculation of the friction factor – f.

The value used for the friction factor is important in terms of forces and transitional attack angles. Therefore, a method of accurately measuring it is necessary. Challen *et al.* indirectly determined f experimentally by calculating τ from the measured forces and used a value of k dependent on the strain hardening of the material from the empirical plastic stress strain relation as a function of the shear flow stress [58]. Further examination of this is given in the discussion.

1.5.3. Ratchetting.

For small attack angles and good lubrication, very little plastic deformation will occur and the only means of metal removal will be from low-cycle fatigue or ratchetting. Yang and Torrance [59] applied Challen and Oxley's wave model for small angles in ratchetting and low-cycle fatigue to predict the number of strain cycles to produce wear debris for a hard steel wedge pressed against aluminum, brass and copper bars rotating slowly in a lathe. The wear rates measured were related to the strain cycle predicted from the attack angle of the wedge and the friction coefficient using the wave formation slip-line field. Yang *et al.* [60] performed similar tests and concluded that ratchetting and low-cycle fatigue were working in combination to produce wear but that low-cycle fatigue plays a more prominent role than ratchetting. This was in contrast to Kapoor [61] who stated that ratchetting and low-cycle fatigue were both occurring but were acting independently with failure determined by the mechanism that gives the shortest life. If applied to grinding, it is unlikely that either regime would make a significant contribution to friction and wear because of the relatively large attack angles involved and the need for numerous cycles at these low angles to produce wear debris.

1.5.4. Use of Profilometry to Measure Slopes.

Real abrasive surfaces consist of differing attack angles and a method of determining these angles is necessary if the models are to be applied. Torrance and Buckley [26] used Challen and Oxley's three slip-line fields and combined it with ratchetting to predict the friction coefficients in the wear of brass and aluminum with abrasive paper. They measured the slopes of the asperities by profilometry. They determined the slopes from the profiles by spectral analysis using the procedure discussed by Moalic *et al.* [62] and Torrance and Parkinson [63] and achieved good correlation between experimental and theoretical values. They discussed the limitations of stylus measurements with a maximum measurable angle of $\alpha=45°$ because of the included angle of most styli of around 90° and the possibility of "bounce" in the profile over the highest peaks. Other observations

have shown that some angles are greater than 45° in abrasives [64]. However, Torrance and Buckley measured a distribution of angles with increasing depth into the wheel and noted that, at the grain tips where abrasion occurs, the large majority of slopes were significantly lower than 45° so that the limit of attack angle imposed by the stylus should not be a hindrance in the region of contact.

1.5.5. Strain Hardening.

The slip-line fields described by Challen and Oxley [1] assume a perfectly-plastic material – i.e. one that neglects elastic effects, has no previous strain-hardening and does not strain-harden during deformation. Real materials will show some change in hardness due to the plastic flow of material at the grit/workpiece interface. This is usually an increase in hardness unless surface temperatures are detrimentally large to induce residual tensile stresses. Depending on the strain-hardenability or contact ductility of the material, some materials will strain-harden considerably. Strain-hardening will result in lower transitional attack angles between plowing and cutting and changes in the wear rate and coefficient of friction. Black $et\ al.$ [65] investigated the effect of strain-hardening by performing tests on aluminum specimens in the as-received condition as well as specimens in which the test surface had been plastically worked prior to testing (estimated shear strain=2.8 in a surface layer of approximately 1.00 mm depth). The effect of plastic working of the specimens would be to increase their hardness and decrease the strain-hardening rate. They found that, for specimens in the as-received condition, the value of α for the transition from wave formation to chip formation (α_{trans}) occurred at a α_{trans}=45° for Molykote boundary lubricant, α_{trans}=45° Shell Vitrea oil lubricant and α_{trans}=55° for dry contact. For the hardened specimens, the corresponding values were α_{trans}=35°, α_{trans}=25° and α_{trans}=45°, respectively. This is shown in the table below.

Table 1.1. Effect of strain-hardening on transitional angle.

	α_{trans} – non-strain-hardened	α_{trans} – strain-hardened
Molykote lubricant	45°	35°
Shell Vitrea oil lubricant	45°	25°
Dry contact	55°	45°

Therefore, prior strain hardening had the effect of lowering the transition angle for all cases. Next they included a strain-hardening index in the chip formation model to significantly improve the accuracy of the predicted values of α_{trans}. They therefore concluded that the perfectly plastic assumption is inadequate and that account must be taken of the strain-hardening properties of the deforming material. They also found that, for wave formation, when shear strains were less than 10 no cracks could be detected but cracks were always present when strains were above this value. It was reasoned that, for a non-hardened specimen, cracks would occur at a somewhat lower strain (prior shear strain=2.8, crack initiation at strain=10, therefore required strain to initiate cracks in hardened specimen=7.2). In other work, Black et al. [66] performed experiments on as received specimens and specimens with prior plastic working and also found that the perfectly plastic assumption is inadequate and that account must be taken of the strain-hardening properties of the material.

Kopalinsky et al. [67] developed a slip-line field model of strain-hardening that could be used, although implementation was time-consuming. Kopalinsky performed experiments similar to Challen et al. [58] with a hard wedge indented vertically into a horizontal surface of a relatively soft specimen [68]. She split the specimen into two sections and printed a grid on one face and then reassembled the grid for the experiments. After experiments, the deformed grid gave a picture of the deformation and the strain distribution. Results were given for various wedge angles and lubrication conditions. She found that the sudden increase in strain predicted by the slip-line field solution does not occur in real materials so that the assumed velocity discontinuities are basically acceptable and that strain-hardening was significant and, for most materials, could not be neglected in the model. Kopalinsky

et al. [67] then used a computer-aided method to calculated the strain-rates from an experimental flow field. They used this to predict the flow stress from the empirical stress-strain relation. They then showed that tensile stresses can exist in a small region of the wave-formation field which is important in considering the processes of low cycle fatigue and fracture as wear mechanisms.

1.5.6. Applications of Slip-Line Field Models to Grinding.

Several researchers have applied Challen and Oxley's slip-line field models to grinding, in particular, to the cutting regime. Hastings and Oxley [69] applied a slip-line field model of the cutting regime to predict cutting forces. During grinding, the large temperatures present at the grit/workpiece interface will act to lower the hardness of the workpiece. Conversely, the extremely large strain rates imposed on the workpiece will act to increase the hardness. To investigate this, they took into account the dependency of the shear strength on the shear strain rate on the temperature. The approach of Fenton and Oxley [70] of taking a small number of experimental machining results for cutting forces and shear angle to calculate the strain hardening parameters and extrapolating them over a very wide range was overcome by using the data from Hastings *et al.* [71] for high speed compression tests on low carbon steels. Strain-rates ($\dot{\varepsilon}$) of $\dot{\varepsilon} \approx 450$/s were lower than that usually encountered in machining ($\dot{\varepsilon} = 10^3$ to 10^6 /s, even higher for grinding) but temperatures were over a wider range (0 °C to 1100 °C).

Kopalinsky [72] used Challen and Oxley's chip-formation slip-line field models [1] and the results of Hastings and Oxley [69] to determine the rubbing forces by subtracting the predicted average cutting forces from experimentally measured grinding forces. In calculating values for flow stress, she used the flow stress properties determined by Hastings [73] for plain carbon steel for more accurate values taking into account the effect of strain rate and temperature. She stated solutions were not available for negative rake angles (α_{NR}, $\alpha = 90° - |\alpha_{NR}|$) greater than $-55°$ ($\alpha = 35°$) and for small undeformed chip thicknesses ($h < 0.75$ µm) and that this was in agreement with others [74,75,76]. Therefore, the critical value for the

negative rake angle (the value below which a chip is not formed) is $\alpha_{NR}= -55°$ ($\alpha=35°$) for all chip thicknesses considered. Below these values, a transition from cutting to plowing or rubbing was considered to occur. In a follow up to this, Kopalinsky used these findings to calculate temperature distributions in the workpiece [72,77]. She performed tests at a series of negative rake angles to correspond to different degrees of wear (α_{NR}=-30°,-34°,-38°,-42°; correspondingly α=60°,56°,52°,48°). She used corresponding wear flat areas of A%=1.25%, 2.01%, 3.16%, 5.25%, respectively. She concluded that the predicted temperature rise with wheel wear results almost entirely from the increase in negative rake angle of the cutting edges, the influence of the increase in wear flats areas being much smaller. Samuels [78] noted average values of 70° to 30° or even smaller. Although this value seems unrealistically high for grinding, – especially at the grain tips – and does not fall into the range of slopes measured by profilometry, it is a reasonable value for the assumption of orthogonal cutting with the allowance for strain hardening.

1.5.7. Profilometry and Application of Slip-Line Fields to Grinding.

Brenner and Torrance [23] used Challen and Oxley's three slip-line fields and applied them to grinding. They measured the wheel profiles from replicas taken of the grinding wheel (stylus speed=0.0508 m/s, 40 Hz sampling frequency, 15 Hz low-pass filter, sample length 10.4 mm). The profiles were analyzed using the spectral techniques developed by Moalic *et al.* [62] and Torrance *et al.* [63]. Because of the long wavelength undulations caused by the way the replicas were formed, long wavelengths were excluded from the profiles. However, Narayanaswamy *et al.* [30], who investigated errors that results from replication, found that the shorter wavelengths in the power spectrum were well reproduced. Therefore a long-wavelength cut-off was imposed equal to the average separation of the grip tips on the wheel surface which can be calculated from the grain dimensions according to Torrance [12]. They divided the profile into 100 equal steps and the profile was passed through a differentiator filter to give slope and curvature values for every point on the profile. It was then possible to give profile slope and peak

curvature as a function of depth into the profile. Brenner and Torrance found that values of average slope did not vary much between tests because they depended mainly on the cleavage geometry of the alumina abrasive in the wheel. They did, however, see an effect on the average grit tip radius. Therefore, this led to the development of a "sharpness ratio" defined as

$$\text{sharpness ratio} = \frac{1}{2}\frac{D_{g,mean}}{r_{grit-tip}} \tag{26}$$

where $D_{g,\,mean}$ is the mean grit diameter and $r_{grit-tip}$ is the radius of the grit tip. This varied significantly from 2.09 for a fairly blunt wheel to 5.57 for a sharp wheel. Next, they applied the slope values to Challen and Oxley's three slip line fields to predict the normal and tangential forces as a function of equivalent chip thickness. The results were encouraging but did show deviation from the experimental forces measured with a dynamometer. The primary handicap of this method is that plane-strain is assumed which is not realistic. Secondly, hardness values assume that no strain-hardening occurs which was found to be unrealistic by others [65, 67, 66, 72, 73]

Badger and Torrance [24] further developed Brenner and Torrance's model by using it for hardened steel specimens. They took several circumferential profiles directly from the wheel which avoided any errors associated with replication and, because of the trueness of the wheel, alleviated the need for low-frequency filters. In addition, they took micro-hardness values at elevated temperatures and used these values from temperature estimates at the grinding interface for more accurate values of hardness – although no account was taken for the increased strain rates. They reduced the amount of scatter in experimental results by employing a unique method of overcoming wheel-head deflection inaccuracies by incrementing the in-feed before every pass until steady-state forces were reached. An improvement in results was seen compared to the previous publication [23]. However, the assumption of plane-strain and a perfectly plastic workpiece hindered its accuracy.

Hastings and Oxley [69] calculated the effect of rake angle on the ratio of normal to tangential forces in grinding. They concluded that the primary deficiencies of the slip-line field method – that plane-strain and an initially flat workpiece geometry are assumed – is not always realistic. In addition, they stated that an oblique model of the cutting tool that could utilize a statistical method for defining the cutting geometry would be useful. Lastly they stated that a more complete model would need to take into account the rubbing forces at the grain tips as discussed by Malkin [29] and also the work involved in plastic deformation not resulting in metal removal –*i.e.* plowing.

1.6. Elasto-plastic Models.

One of the earlier pieces of research on wear was done by Kruschev [79] who showed experimentally that the resistance of pure metals and non-heat-treated alloys to abrasion by abrasive paper is proportional to their hardness. A simple model of abrasion has been proposed by several researchers which explains this well and can be easily extended for heat-treated alloys. It is given in the standard textbooks [80,81]. An assumption of these models is that a constant fraction of the volume plowed in the grooves in the metal is removed as wear debris. The proportion depends on the geometry of the abrasive and not on the material being abraded. Others [82,83] assumed that all displaced material was lost which led to significant overestimates of wear rates.

Chen and Rowe [84] defined a cutting efficiency ratio, β_{eff}, as the ratio of the volume of the material removed to the volume displaced by the undeformed chip. The material that is piled up alongside the groove in the form of side ridges is the proportion $(1-\beta_{eff})$ of the volume of the undeformed chip. The material remaining on each side of the groove in the form of side ridges is

$$A_{ridges} = \frac{A_{total}}{2}(1 - \beta_{eff}) \tag{27}$$

where A_{ridges} is the area displaced to side ridges and A_{total} is the total area of the undeformed chip. Therefore, higher values of β_{eff} mean that a larger proportion of material is being removed as wear debris. They then estimated the grinding forces based on Chen [85,86] by assuming a spherical grain model as illustrated in Figure 1.7. This model uses the grain sharpness and grain depth of cut. The forces were determined by

$$F_{t,grit} = \frac{3\pi}{4}\frac{b}{t}H\frac{C^{'}}{3}A_{total}\left(\sin\alpha + \mu\cos\alpha\right) \tag{28}$$

$$F_{n,grit} = \frac{3\pi}{4}\frac{b}{t}H\frac{C^{'}}{3}A_{total}\left(\cos\alpha + \mu\sin\alpha\right) \tag{29}$$

where $F_{n,\ grit}$ is the normal force on the grain, $F_{t,\ grit}$ is the tangential force on the grain, b_w is the cutting width of the grin, t is the depth of penetration of the grain into the workpiece, H is the hardness of the workpiece, $C^{'}$ is a constraint factor, A_{total} is the cross sectional area of the undeformed chip, μ is the friction coefficient and α is the angle of the indentation force from the normal. The total grinding force can then be calculated as the summation of the tangential forces on each grit. Chen and Rowe [84] then used this to successfully predict surface roughness values in grinding. The model is noteworthy in that it takes into account both cutting and plowing simultaneously.
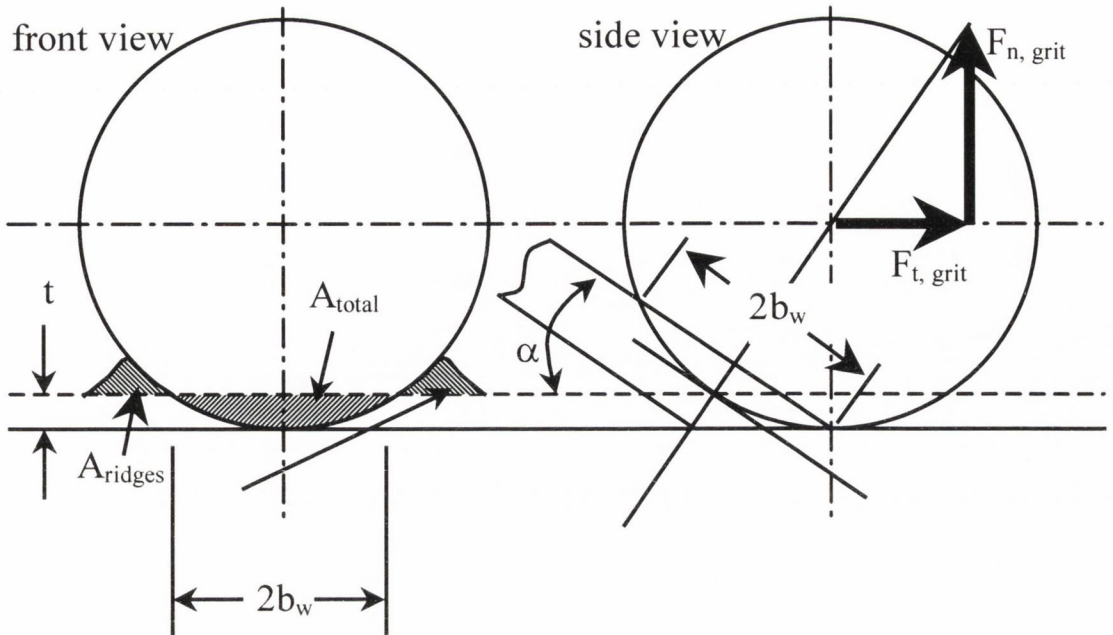
Figure 1.7. Modeling of grits as spheres with displaced areas.

Numerous researchers have published findings on the critical attack angle when chip formation can occur, α_{trans} [87,88,89,90]. Mulhearn and co-workers published several papers [64,91,92] which used hard steel pyramids to plow grooves in various metals and were able to study the effects of tool geometry and material type on wear rates. They predicted critical attack angles for the transition from no metal removal to chip formation. They stated that virtually all abrasive wear would take place by cutting. Mulhearn's tests were done with the pyramid moving orthogonal to the workpiece. Torrance [93] noted that real abrasives would move at an angle that deviates from the orthogonal as shown in Figure 1.8 below. Others [94,67] have used a Vickers indenter to simulate the shape of the grit. Childs [95] was one of the first to use cones as a three-dimensional representation of frictional resistance along with Rubenstein *et al.* who [76] who measured force ratios. Similar tests were also done by Moore [96] and Childs [97]. Lavine [98] represented a grain as a sawn-off cone with a cone attack angle of 45° and the sawn-off section of two-dimensional radius r. The radius of the sawn-off section was the source of heat generation and the partition ratio of energy into the workpiece and into the wheel was calculated by Rowe *et al.* as a function of r [50].
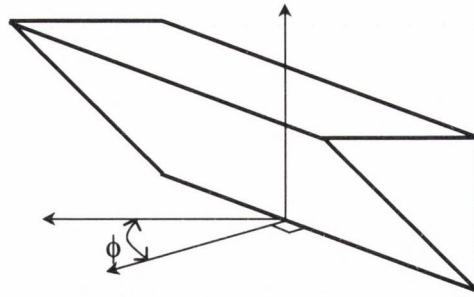
Figure 1.8. Contact at angle to sliding direction.

1.6.1. Pyramid-shaped Indenter Models.

De Vathaire *et al.* [99] published a quasi-upper bound model of abrasion for the plowing of a rigid-plastic semi-infinite body by a rigid pyramidal indenter without chip formation. Gilormini and Felder [100] then published a more complete model based on similar hypotheses but taking account of the formation of a frontal ridge and chips. They modeled abrasion by using a pyramid-shaped indenter and, using a velocity field and resolving the force vectors with the velocity vectors to calculate the rate of work per unit time in each plane, they minimized the dissipated power to calculate the forces – a quasi-upper-bound method since one of the boundaries was part of the solution. Figure 1.9 shows the geometry of the indenter. Here volume of material displaced by the indenter is distributed among a frontal ridge, two lateral ridges and two chips.

The velocity field depends on a total of six parameters. The procedure cannot be justified by the upper bound theorem of the theory of plasticity because the dimensions of the plastic region depend on the parameters of minimization. Tests were run at different attack angles for the scratching of plasticine by a pyramidal aluminum indenter under dry conditions while measuring the normal and tangential forces. The experimental tangential forces were in reasonable agreement with the predictions. They stated that minimization leads to a poor estimate for the depth of the scratch and the minimization was reduced to five parameters by using the actual measured depth of scratch from the experiments. This led to more accurate results.

The predicted normal forces were not as good with either five or six parameters. They attributed the discrepancy to adhesion of the plasticine to the indenter and to the numerical difficulty of minimizing a six variable function. A series of predictions were made for values of f ranging from 0 to 1, but the most accurate results were closest to predictions for $f=1$ which agrees with the conditions of dry contact. They then modified their model to reduce it to a two parameter function by simplifying the geometry and eliminating the chips and the frontal ridge to approximate the experimental conditions of Kudo and Tsubouchi's tests on low carbon steel with a diamond-based pyramidal indenter where no chip was observed [101]. This model was significant in that it was a more realistic representation of what occurs in abrasion. In addition, all three modes of contact are allowed to occur simultaneously. However, two of the drawbacks of the model are that it assumes that the region below the pyramid does not plastically deform and that the workpiece is initially flat, neglecting the effect of previous contacts.
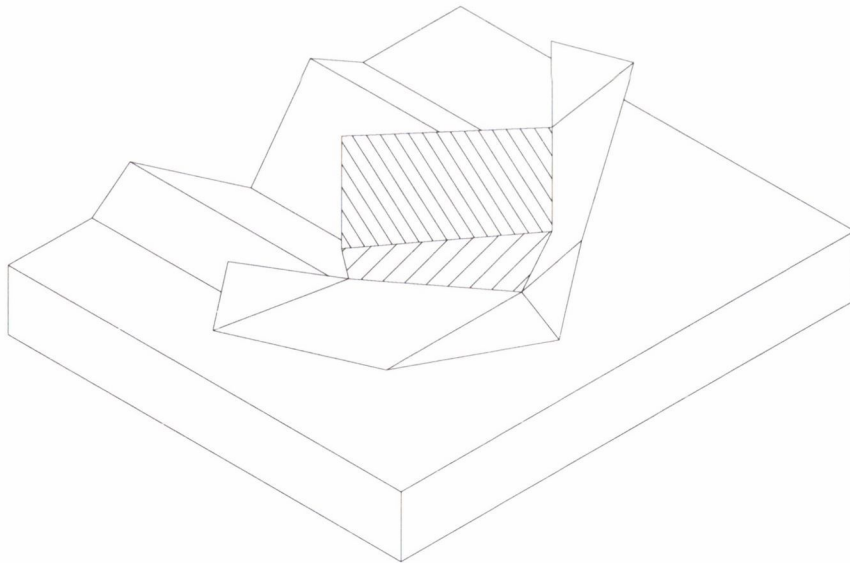
Figure 1.9. Pyramidal contact with chips, wedge and side ridges.

Kato [102] looked at the effect of the abrasive shape on wear and developed a map of wear modes based on pyramidal angles as shown in Figure 1.10 below. Torrance [103] developed a three-dimensional irregular-shaped pyramidal model of abrasive cutting and examined the effect of the shape on the surface finish and specific energy in the process. Torrance stated that, since the attack face will not be

orthogonal to its direction of motion, wear will occur by what he called "side wall stripping" where metal is extruded out to the side of the attack face rather than being forced upwards into a chip. Other researchers have referred to both scenarios as chip formation. Kato and co-workers [104,102,105] confirmed Torrance's previous conclusions [93] that this may occur over a much less restricted range of attack angles than orthogonal cutting. In other words, the critical attack angle from plowing to cutting is lower in oblique cutting than in orthogonal cutting. Torrance [103] gave a criterion to predict when a change from plowing to side wall stripping will take place. He found a transition in a Vicker's indenter in brass from plowing to stripping occurred for an included angle between 64° and 74°. Much larger local strains were required for stripping than for plowing. Therefore, it was concluded that stripping was predicted to be suppressed in materials which work harden strongly or which are strain rate sensitive. If this is applied to grinding [106], materials which work harden significantly are considered more difficult to grind so that the plowing would dominate over cutting or stripping resulting in much lower rates of abrasion and higher specific energies. This was seen earlier in Section 1.5.5 (page 24) from work by Black *et al.* [65].
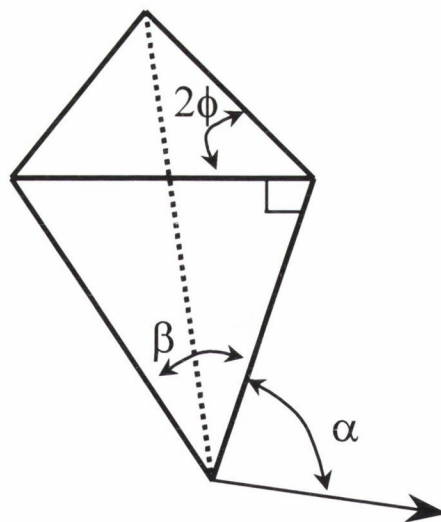
Figure 1.10. Pyramid indenter from Kato *et al.* [102].

Since the highest rates of metal removal were found with high slopes parallel to the direction of motion and low slopes perpendicular to the direction of motion (large α and large ϕ from Figure 1.10 above), Torrance [103] suggested that it would be profitable if a method could be found to dress the wheel to achieve an anisotropic distribution of grit slopes where the slopes across the lay are much less than those along the lay. Buttery [107] also stated the same from his force measurements from different grain sizes stating that larger grains produce larger forces because of their width to depth ratios so that a larger included angle would facilitate cutting. The lowest values of theoretical specific energy were found when $\alpha \approx \beta$ and $30° < \beta < 60°$ which is the range of β expected from the roughly cubic grits used in many grinding wheels. The surface slope produced at this value of β is $30°$ which was found by Hillman *et al.* to be common on ground surfaces [108]. In contrast to these values, one of the earlier researchers to measure slopes was Williamson who found slopes usually lying between $5°$ and $10°$ and occasionally as high as $25°$ with asperity heights from 10 to 300 μinches (0.25 to 7.6 μm). However, Hillman's method of measurement had much higher resolution.

Torrance [109] combined the slip-line field technique with the pyramid indenter to produce two new slip-line fields – one from Grunzweig *et al.* [110] equivalent to a wedge indentation from the front face of the edge forward pyramid and one from Challen and Oxley [1] equivalent to a wedge emanating upwards and outwards from the side of the face of the pyramid. Although a bona fide slip-line field method can only be applied for two-dimensional low strain rate problems, previous research [105] has shown that, when judiciously applied, it can give results in agreement with three-dimensional experiments. The model was accurate at low indenter semi-angles but deteriorated at higher angles. Torrance concluded that the model was valid in spite of its assumptions and that it significantly improved upon the work of de Vathaire *et al.* which agreed with experiment over a limited range of indenter angles [99]. Numerous previous researchers have noted the minimum attack angle necessary to form a chip – the transition from plowing (where material is displaced to the ridges with no material lost) to micro-machining (also known as chip-formation or side wall stripping by Torrance where material is plowed to the side and also lost in the form of side chips). Torrance [109] found that the value of

critical attack angle from plowing to stripping changes little with f until f reached a value of 0.5, when it increases very rapidly. This suggests that little is to be gained by improving lubrication in this region. This also implies that, in grinding, the benefits to improved lubrication which lie in this region, say for example between water and oil, is very small at least in terms of chip formation – although not necessarily in terms of the reduction of plowing and rubbing forces generated. Xie and Williams [2] found lower transitional angles between plowing and cutting for oil than for dry contact

- 32°-44° for dry contact
- 24°-33° for oil

which would cross over this region (dry contact approaching f=1.0 while oil in the region of f=0.5).

Lortz [111] discussed a dead zone in the region ahead of the grain. If the cutting depth of the grain was below some minimum value, no material removal will occur. The critical depth of the dead zone depended on the grain shape and the friction at the grit/workpiece interface. Inasaki [112] used a pyramid-shaped asperity model on a molecular level and showed the deformation of 150000 atoms in his model and the effect of moving edge-forward versus face forward. Kato and coworkers [113,104,105] performed experiments on brass, carbon steel and austenitic stainless steel. They produced wear maps defining the transitional regions between cutting, plowing and wedge formation as a function of the shear strength at the contact interface (f) and the parameter for the degree of penetration (D_p). For a semi-spherical contact, the degree of penetration is defined as that ratio of the depth of penetration to the radius of contact. They used spheres in the experiments and modeled them as wedges. They therefore developed the relationship

$$D_p = 0.8 \frac{1 - \cos\alpha}{\sin\alpha} \tag{30}$$

to relate the degree of penetration to an angle (α) which can be considered analogous to the attack angle. A constant of 0.8 was experimentally found to model the two-dimensional models and the experimental values with three-dimensional models. It can be seen in Figure 1.11 below that in the region of small values of f, the transition from plowing to cutting occurs at a value of $D_p \approx 0.15$ corresponding to an angle of about 21° (slope=0.4) in agreement with Challen and Oxley and Xie and Williams [2] above.
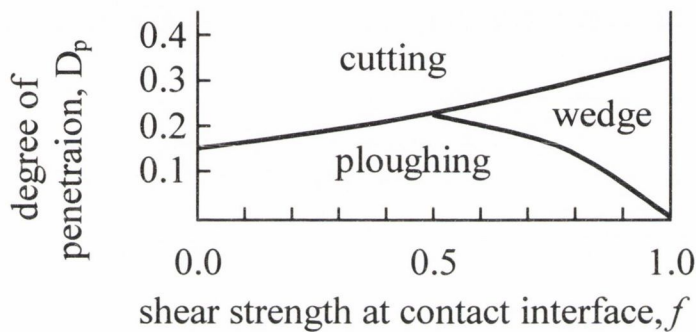
Figure 1.11. Kato's regimes of abrasive wear.

Kato *et al.* [102] later developed his model for an asperity with an attack angle and a dihedral angle. They performed scratch tests on aluminum and brass at various combinations of angle and noted the mode of wear. They took profiles of the worn sections and determined the amount of wear by assuming incompressibility and subtracting the area of the side ridges from plowing from the area of the valley. They then used an electron microscope to examine the worn surface and developed a map of the mode of wear as shown in Figure 1.12 below for aluminum under dry conditions.
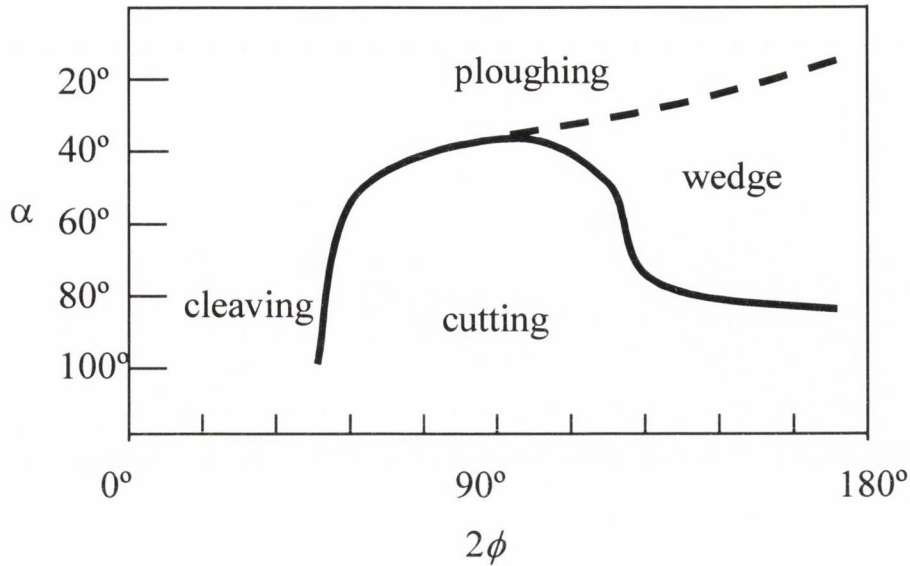
Figure 1.12. Wear map for abrasion of Aluminum – dry conditions.

From the map we can see that, for small values of 2φ, the wedge is long and narrow, similar to a knife moving forward, which results in a region of large cleavage. As the angle increases, the mode of contact turns to cutting for large values of α and plowing or small values of α. For large values of 2φ approaching 180°, this is effectively a "face-forward" contact with the creation of a wedge.

For lubricated conditions, the regions of cutting, cleaving, plowing and wedge formation will change. This is shown in Figure 1.13 below. From the map, we can see that better lubrication caused the region of cutting to extend to smaller attack angles and included angles than with dry contact. Also, at larger dihedral angles the region of wedge formation decreased being replaced with cutting at larger attack angles and plowing at smaller attack angles.
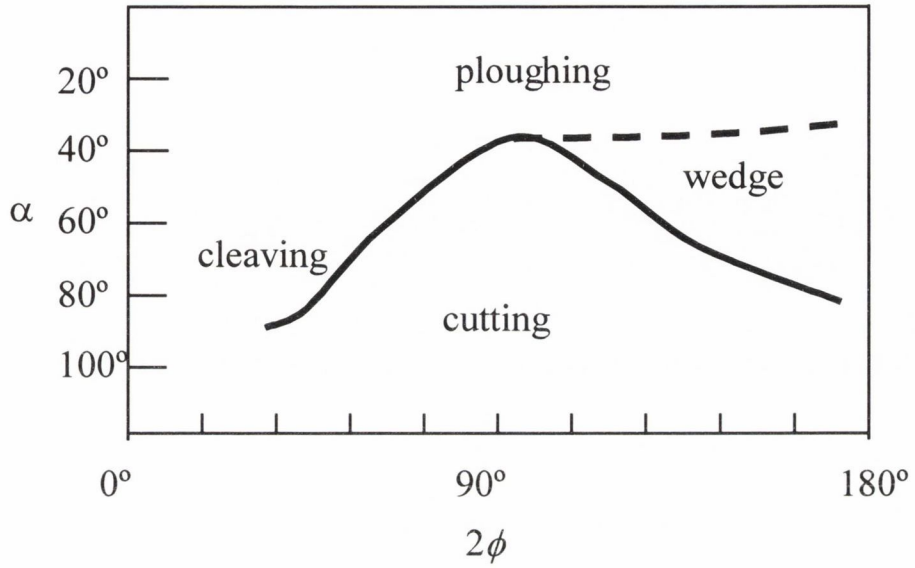
Figure 1.13. Wear map for abrasion of Aluminum - lubricated conditions

1.7. Xie and Williams Three-Dimensional Model of Abrasion.

Xie and Williams used a quasi-upper bound method [2] for a pyramid-shaped indenter similar to that of Gilormini and Felder [100] but took into account plastic deformation below the tip of the pyramid. The depth of penetration was set to unity resulting in seven independent parameters that were needed to describe the geometry of the system. They were defined as:

- the height and width of the side ridge (1,2)
- the height and length of the prow (3,4)
- the point where these join (5,6)
- the coordinate of the point of lowest plastic deformation (7).

The geometry of the edge-forward pyramid-shaped indenter is defined by the two angles ψ, the included angle, and ϕ, the dihedral angle, as shown in Figure 1.14 below. When ψ is small, the indenter is narrow and knife-like. As 2ϕ increases the asperity becomes more "bluff". When 2ϕ has its maximum value of 180°, the two leading faces have coalesced into one and the indenter is effectively moving in the "face-forward" mode. The asperity can be presented to the surface with its vertical axis tipped forward or backward relative to the normal direction from the surface. This defines the attack angle, α.
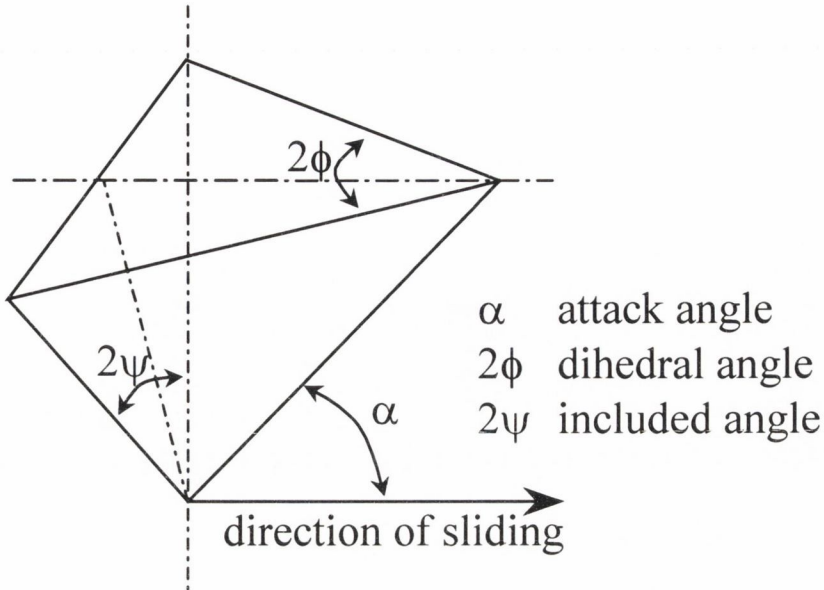
Figure 1.14. Geometry of pyramid-shaped asperity of Xie and Williams.

Resolving the velocity vectors in the system for volume conservation of the incompressible material and connecting them to the seven geometric parameters, the rate of working per unit time from the applied load can be set equal to the sum of the force vectors and the velocity vectors in each plane of contact. By searching for the combination of the seven parameters that minimizes the dissipated power according to the upper bound theorem which states that this represents the most likely set of values, the frictional force can be calculated. In addition, the procedure leads to estimates of the proportion of displaced material appearing in the side ridges and the machined chips.

Xie and Williams defined the regimes of contact as follows:

(i)   elastic shakedown – involves non-permanent elastic deformation of the material

(ii)   plowing – involves permanent plastic deformation without material removal and

(iii) micro-cutting – involves material being simultaneously sheared beneath the grit, being pushed sideways and being removed as chips.

Therefore, all three interactions occur in the cutting regime. This is illustrated in Figure 1.15 from a scanning electron micrograph of a groove cut in brass by a Vickers indenter for a material with no prior grooves in the workpiece from work by Torrance [103]. Here all three modes occur simultaneously with the chips formed to both sides.
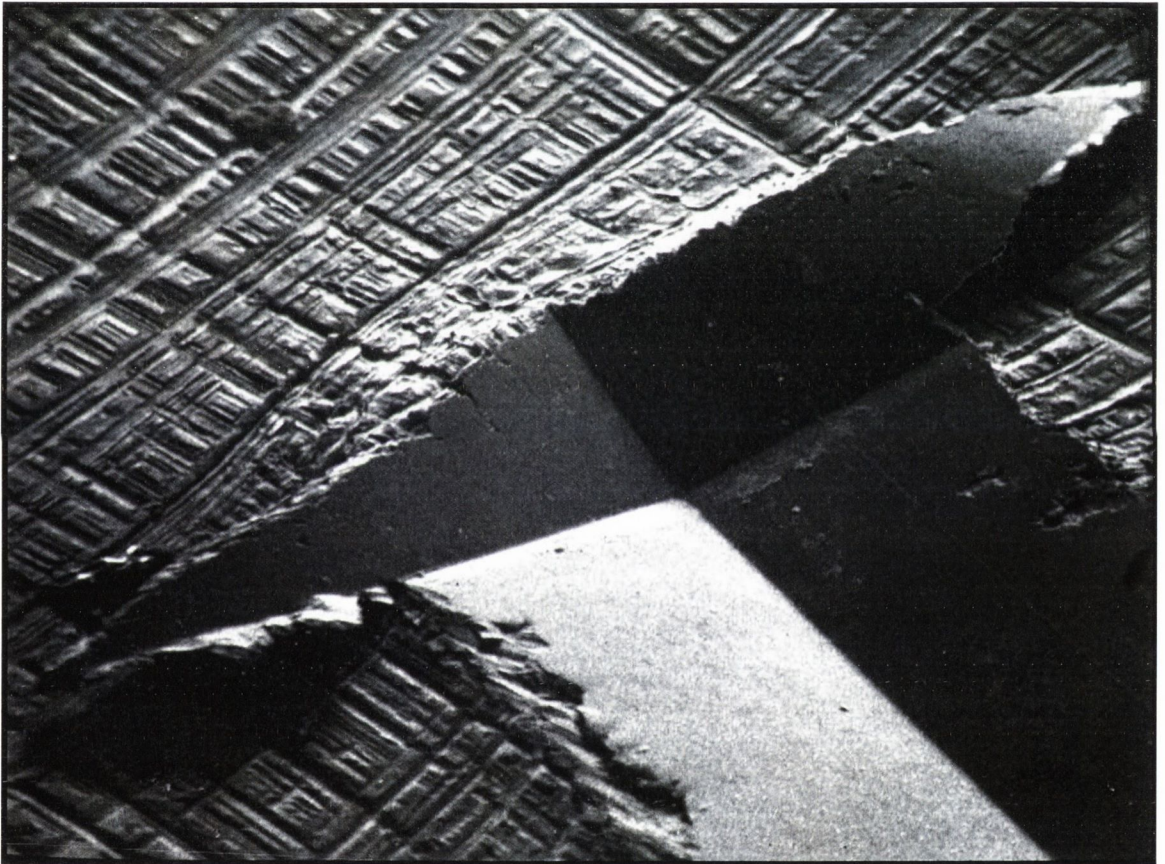
Figure 1.15. Scanning electron micrograph of a scratch in brass.

From the figure we can see the creation of side ridges due to plowing, a frontal wedge of material being pushing ahead of the asperity and the creation of two chips to either side of the asperity.

1.7.1. Parallel Wear Tracks.

Xie and Xilliams [2] stated that in actual abrasion, the geometry of the asperities will rarely be symmetrical. In addition, as material is plowed to the side of the asperity as a wear track, succeeding asperities will encounter the deformed surface so that, in actuality, asperities will constantly be moving through material that has a previously deformed structure of parallel wear tracks from previous passes. This can be seen on any abraded, ground or polished surface where the scratches are all aligned in the same direction.

If we imagine an asperity moving through material that has a previous wear track, we can define a distance L between successive wear tracks. If the following is true:

$$L \leq (h + h') \tan \psi \qquad\qquad (31)$$

where h is the depth of penetration and h' is the height of the pre-existing wear track, the indenter is always moving through material that has been already heavily changed in the formation of the preceding set of grooves as shown in Figure 1.16 below.
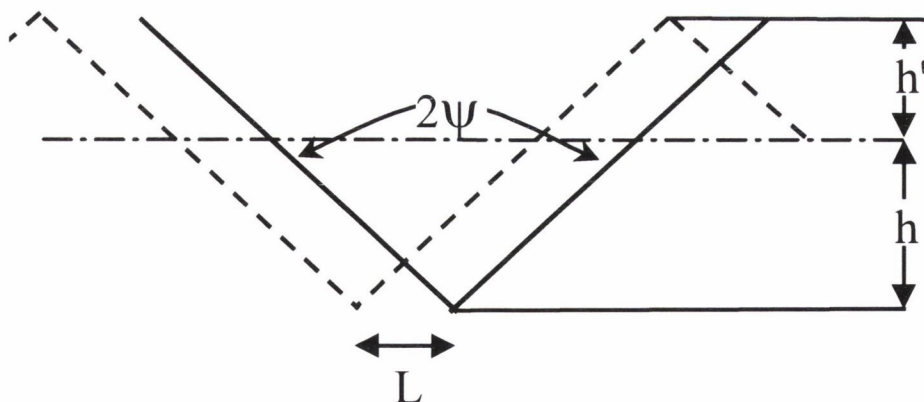
Figure 1.16. Front view of adjacent tracks of pyramid indentation.

Xie and Williams [3] defined a useful parameter, l, the dimensionless distance between tracks, which can be calculated from

$$l = \frac{L}{(h + h^{'})\tan\psi} \tag{32}$$

Therefore, an asperity with a large included angle (ψ), a large degree of penetration (h) and a high side ridge ($h^{'}$) will be more likely to overlap a pre-existing wear track. Since almost all previous researchers have assumed an initially flat surface, this could account for the fact that theoretical transitional attack angles are often much higher than those observed in practice.

1.7.2. Experiments.

Xie and Williams performed tests on work-hardened copper (effective strain=0.75) and used the stress-strain curve from Atkins and Tabor [114] with the power law relation to calculate the shear flow stress [2]. They used dry contact and Shell HV1-60 BRENT base oil lubricant for their experiments. For dry conditions they assumed a value of f=1.0 and for oil a value of f=0.25. They stated that the overall tangential force is relatively insensitive to f as most of the energy is dissipated in subsurface deformation, which was in agreement with Torrance [109]. Xie and Williams measured the tangential force for various attack angles at a constant dihedral angle so that the included angle increases with decreasing attack angle. Theoretical values for force and transitional attack angle were well-predicted. It was seen that lubrication did not have a significant effect on forces but did change the transitional angles from plowing to cutting. This occurred at attack angles of 32°-44° for dry conditions and 24°-33° for oil lubrication.

Xie and Williams then performed tests on as-received aluminum specimens and varied both the attack angle and the dihedral angle. This produced a wear map of wear mode with attack angle and dihedral angle as the axes. The predicted values of transitional attack angle and the measured values were in close agreement.

The next step was to perform experiments with parallel wear tracks to determine the effect of l on the wear mode. It was found that when the relative lateral displacement was large, almost all the material displaced was plowed into side ridges regardless of the indenter shape. However, when the relative lateral displacement was small – regardless of the included angle – some of the material was removed as micro-machined chips. A wear map was produced with l as the ordinate and the attack angle and the included angle as the abscissa (both together, since $2\psi=180-2\alpha$). It was evident that there was a clear line defining the transitional region from cutting to plowing for lateral displacement and for small values of displacement the wear mode was cutting even for small values of attack angle. Therefore, it can be concluded that a realistic model of abrasion must take into account previous deformation and parallel wear tracks.

Lastly, it was noted that the model was principally a geometric one. Although the material was allowed to work harden, no limit was place on its ductility. Since the strains were very large, the repeated passes will place a limit on its ultimate ductility resulting in a greater material loss than a specimen of assumed infinite ductility – *i.e.* strain hardening will lead to a greater likelihood of chip formation than plowing.

Next, Xie and Williams published a continuation of their work [3] with tests in strain-hardened copper ($\varepsilon=0.75$). They introduced the dimensionless distance between tracks to the upper-bound minimization and predicted material removal rate (MRR) as a function of the dimensionless distance between tracks and the included angle (with attack angle, from $2\psi=180-2\alpha$). They fit this to a parametric equation to give MRR as a function of l and ψ.

1.7.3. Transitional Angles.

In Xie and William's most recent work [4], they performed numerous simulations similar to those described in [3] and developed a map of when the transition between plowing and micro-cutting occurs which is shown in Figure 1.17. For the calculations leading to these curves, the stress-strain relation of the wearing material

was required. Xie and Williams found it easier to measure the bulk hardness (H_b) and the surface hardness (H_s) than to make estimates of stress based on strains in the material. Expressions for the curves can be given by the close approximations:

$$l_t \approx \left(\frac{\alpha - \alpha_p}{\alpha_c - \alpha_p} \right)^{H_b/H_s} \quad (\alpha_p \leq \alpha \leq \alpha_c) \tag{33}$$

$$a_p \approx \frac{1}{10 f^H} \left[18.6^\circ - \left(\frac{H_b}{H_s} \right)^4 \cdot 10^\circ \right] \tag{34}$$

$$\alpha_{c,trans} \approx \sqrt{10 f^H} \left[35.9^\circ - \left(\frac{H_b}{H_s} \right)^4 \cdot 15.5^\circ \right] \tag{35}$$

where

- α is the attack angle of an asperity at the edge of contact
- $\alpha_{p,\ trans}$ is the minimum attack angle when cutting may take place
- $\alpha_{c,\ trans}$ is the minimum attack angle where cutting may take place for any value of the dimensionless distance between adjacent tracks
- l_t is the transitional dimensionless distance between adjacent tracks corresponding to the transition from plowing to micro-cutting at a given attack angle
- f^H is the interfacial coefficient of friction between the hard asperity and the soft material as defined by $f^H = \tau/H$ (Section 1.3.1, page 12)
- H_b is the bulk hardness of the soft material
- H_s is the surface hardness of the material after wear

The ratio H_s to H_b represents the work-hardening ability of the material. From the figure, we can see that the value of l required for cutting decreases with decreasing attack angle. Conversely, the angle required for cutting is smaller when the distance between adjacent tracks becomes smaller. We can also see that materials that work-harden significantly (large value of H_s/H_b) require larger attack angles for cutting –

i.e. the material is more amenable to plowing. For materials with many overlapping tracks (small l), the angle required for cutting is very small ($\alpha \approx 6.5°$ for H_s/H_b=1.0 and $\alpha \approx 12°$ for H_s/H_b=1.25). This is much smaller than the angles predicted by orthogonal cutting. These values are for f=0.5. Xie also [115] performed sliding experiments for copper and EN24 steel for various states of work hardening or heat treatment with both dry and lubricated conditions.
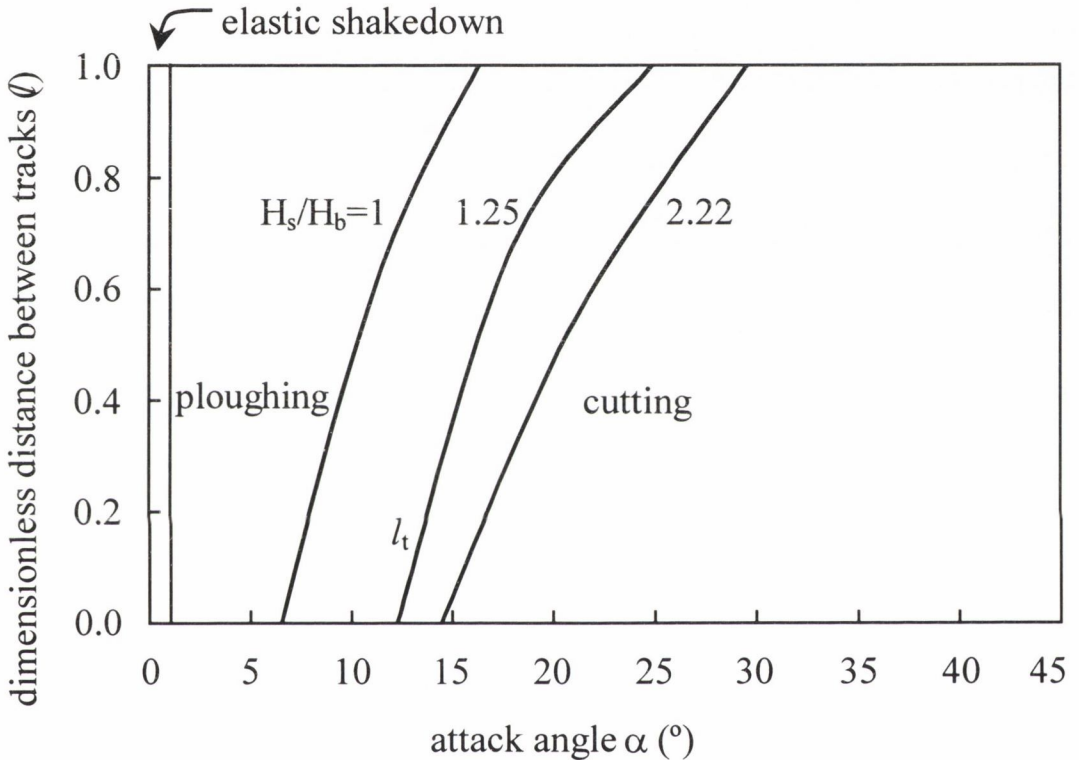
Figure 1.17. Deformation mode map for metallic sliding (f=0.5 from [4])

1.7.4. Calculation of Friction and Specific Wear Rate.

Xie and Williams ran simulations for numerous combinations of geometry, workpiece properties, lubricant type and distance between adjacent tracks. They fit parametric formulae for the specific wear rate, K, and the friction coefficient, μ. Formulae were given for the region of elastic shakedown, micro-cutting and ratcheting failure for ranges of attack angle.

For micro-cutting, the coefficient of friction was given as

47

$$\mu_{cutting} \approx \sqrt{\frac{2}{\pi}} \frac{\tan\alpha}{l^{0.25}} \left\{ 1 - f \left(1 + \frac{\pi}{4\tan^2\alpha} \right)^{0.5} \right\} \tag{36}$$

for conditions when

$$\alpha < 60°$$

and the specific wear rate was given as

$$K_{cutting} \approx 0.003 \frac{\tan^3\alpha}{fkl^{0.5}} \sqrt{\frac{H_b}{H_s}} \tag{37}$$

for conditions when

$$\alpha < 45°$$

where

$$K_{max} = \frac{\tan\alpha}{H_s}. \tag{38}$$

Xie and Williams found that for values of the dimensionless distance between adjacent tracks (l) less than 0.2, the values of μ and K cease to change with any further decrease in l [4] so that l can be given a value for 0.2 when its actual value is less than 0.2.

To validate their formulae, Xie and Williams applied a Gaussian distribution of asperity peak heights to previously published results of abrasion. They assumed the asperity peaks to be capped with a spherical top of constant radius and a cutting point density (asperities per unit area). They then applied their model of abrasion to successfully predict friction and wear rates

In contrast to other models of abrasion, where only a single mode of contact is present for a given set of conditions (α, f, H_s, etc), it is interesting to note how the model of Xie and Williams includes all modes simultaneously. If we plot μ versus α and K versus α for a range of f values, we can see how they vary in Figure 1.18 below.
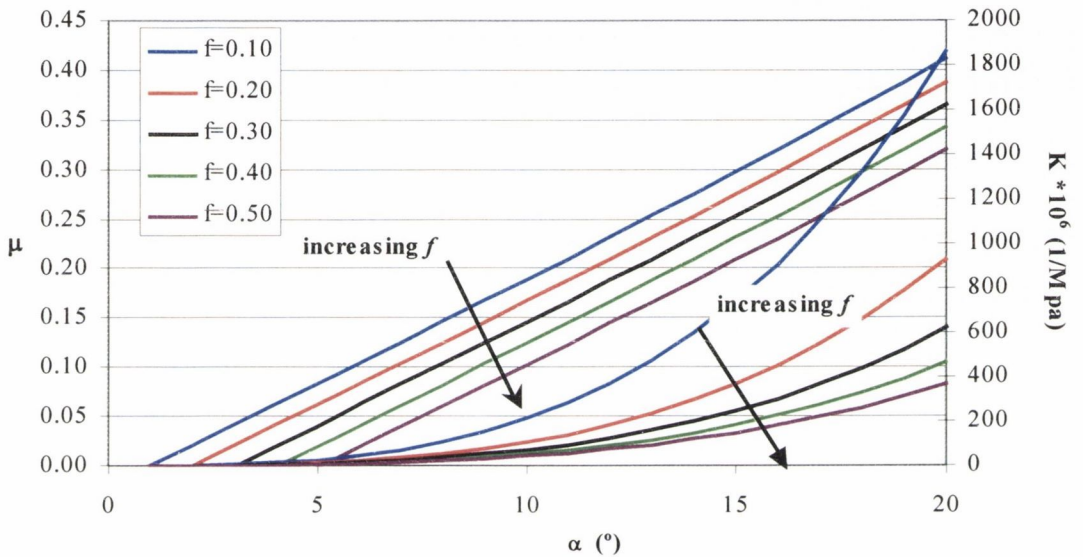
Figure 1.18. Relationship between μ, K and α.

The equation for μ is linear with α and the equation for K is cubic with α. Considering the significance of this, we can see that at small values of α, μ is small yet K is disproportionately small, approaching zero for values of $\alpha < 5°$. As α increases, μ increases proportionately – yet K increases as the cube of α. This means that at small values of α, there is still a significant contribution to μ – whereas wear is not significant at these small values of α. However, as α increases, μ increases linearly while K increases at a faster rate than μ. This indicates that more efficient abrasion occurs at larger angles.

This means that at small angles, the dominant modes of contact are rubbing and plowing so that forces are still significant but wear is negligible. If this reasoning is applied to grinding, a blunt wheel or a small chip thickness where contact occurs at

the small-slope grain tips will lead to significant frictional forces but low wear. Malkin [13] discussed a "size factor" where specific energies were extremely large for small depths of cut. This phenomenon could possibly be explained by the inefficient cutting and dominant rubbing and plowing that occurs at small angles.

We can also see from the figure that both μ and K decrease with increasing α so that it is difficult to see the effect of μ as a function of wear – i.e. the efficiency of the process.

Therefore, it would be interesting to note the change in friction as a function of specific wear rate to illustrate the efficiency of the process with attack angle. This is given in the figure below.
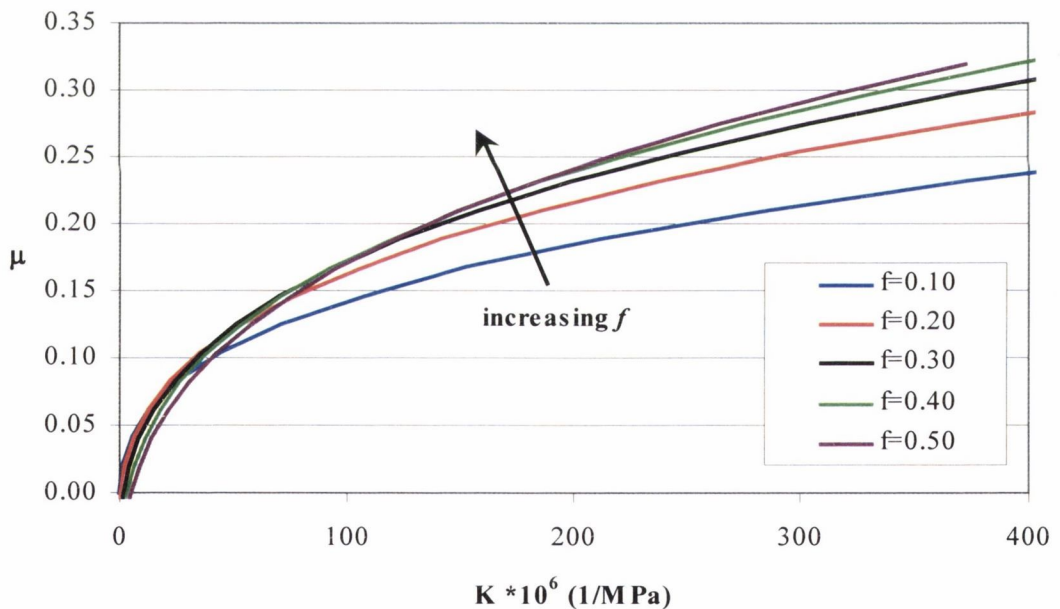
Figure 1.19. Theoretical friction coefficient versus specific wear rate.

Here we can see that as the specific wear rate increases, the coefficient of friction increases non-linearly. If the function was fit to the curve

$$\mu = C \bullet K^n \qquad (39)$$

where C and n are constant, then n would be less than 1 so that more efficient metal removal would occur at larger values of α. This is particularly true at small values of f which facilitate chip formation over plowing. If this reasoning is applied to grinding, specific energies would be smaller at large angles (and, in turn, larger values of equivalent chip thickness).

In order to apply Xie and Williams's model of abrasion to grinding, it is necessary to understand the topography of the abrading surface, the grinding wheel, and the method used to measure the attack angles of the surface.

1.8. Surface Analysis.

1.8.1. Surface Types.

A three-dimensional surface can be defined by its height (z) at a given position (x,y) as shown in (a) in Figure 1.20. If a plane section is taken through the surface, then it can be represented in two dimensions as in (b).

(a)   **(b)**
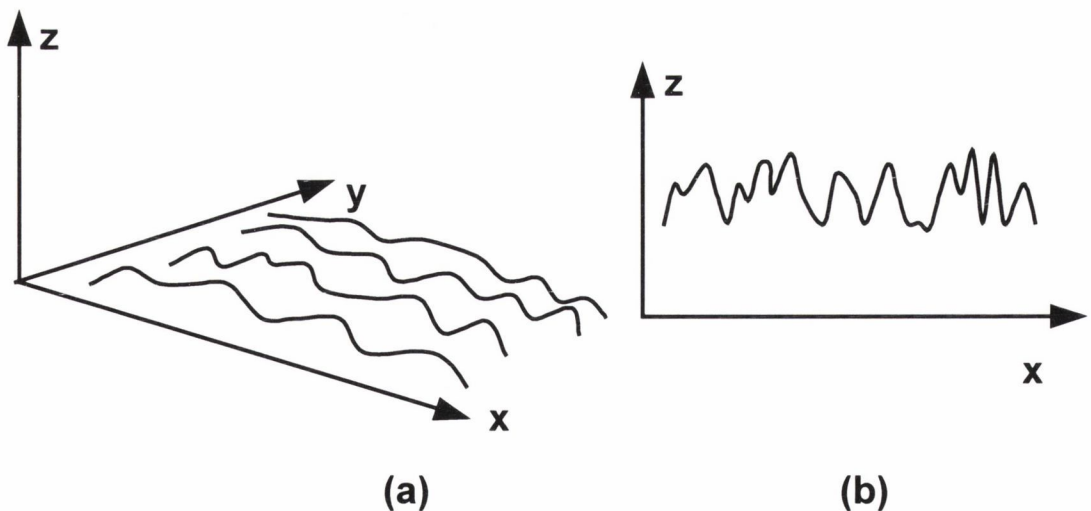
Figure 1.20. 3-D and 2-D representation of a surface.

Nayak classified surface topography into three broad categories [116] which were defined as:

(i)   *Homogeneous* versus *Inhomogeneous*: A homogeneous surface has the same surface characteristics for all regions of the surface. Inhomogeneous surfaces have variations from one region to another. Inhomogeneous effects are not amenable to analytical analysis.

(ii) *Isotropic* versus *Anisotropic*: Isotropic surfaces have the same characteristics in all directions. Few real surfaces, particularly those formed by machining methods, are isotropic. Surfaces produced by grinding are strongly anisotropic due to the consistent direction of scratches produced by the wheel.

(iii) *Deterministic* versus *Random*. Deterministic surfaces have characteristics that can be predicted to some extent by the parameters used in the machining process. Few real surfaces are perfectly deterministic and even simple processes such as turning have a very large random component.

A high-quality grinding wheel should be largely homogeneous and isotropic before dressing. As the wheel is dressed, the wheel surface becomes anisotropic as the dressing action of the diamond occurs in a single direction. The workpiece may be homogeneous or inhomogeneous depending on the heat-treating process, the extent of segregation during cooling, and the resulting microstructure and carbide distribution. Inhomogeneous steels with large clusters of carbides tend to be more difficult to grind than homogeneous steels with evenly distributed carbides. A ground surface is largely anisotropic due to the series of parallel scratches. The complex process of dressing with grit and bond fracture appear to make the surface extremely random, although attempts have been made by Terry and Brown [117] to numerically quantify wheel topography and workpiece topography with parameters such as fractals, dressing lead, abrasive type, grade and structure with limited success. This requires a knowledge of the wheel surface in terms of the density of the grits and the geometry of these grits.

1.8.2. Profiles – Peaks and Summits.

When a cross-section is taken through a 3-D surface as done, for example by a stylus, the resulting profile is a 2-D representation of that cross section. The profile represents the trace seen by the stylus as it traverses the workpiece. In that trace, a peak taken from the profile does not necessarily represent a summit on the surface. More specifically, it represents a peak on the profile which is most likely not a summit. This is illustrated in Figure 1.21, Therefore, it is necessary to differentiate between a peak from the profile and a summit from the surface.
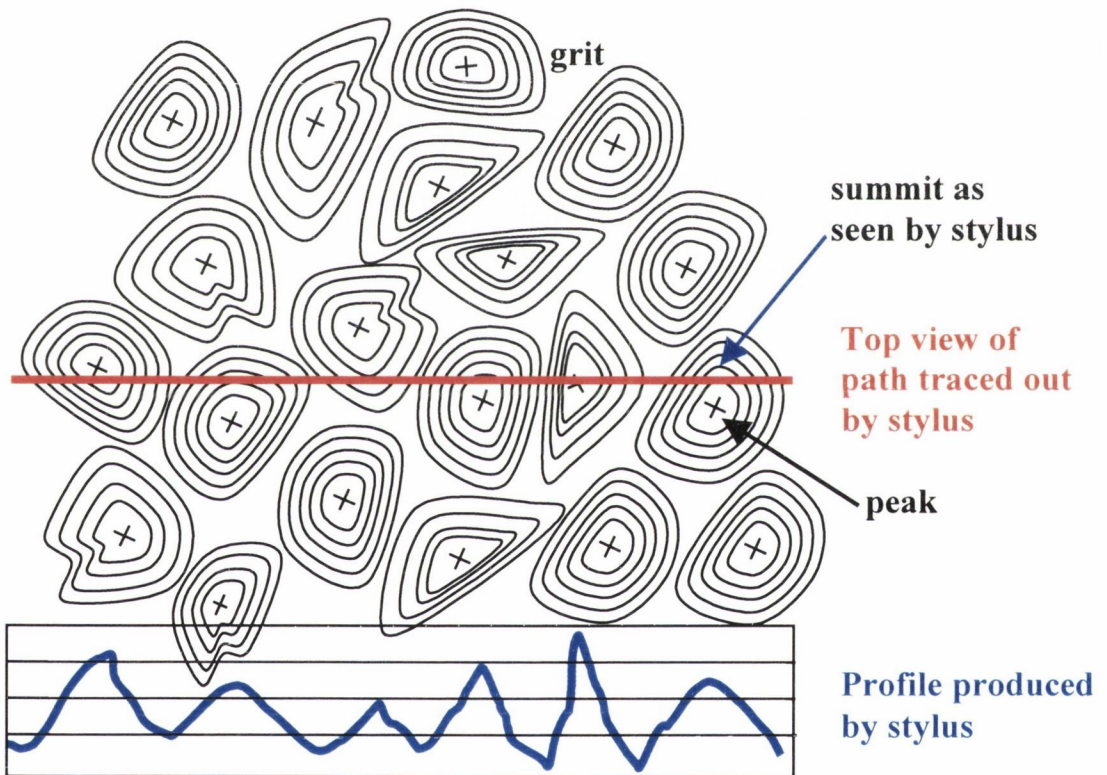
Figure 1.21. Top view and side view of section taken through surface.

1.8.3. Surface Measurement.

Measurement of surfaces has been performed using a variety of techniques, the most common being optical methods and stylus methods. Surface analysis by means of stylus methods has been used since the 1920s and Abbott *et al.* reviewed the method in 1938 [118]. In the 1980's, surface measurement by optical means became more

common. Whitehouse [119] compared the two and concluded that optical methods were progressing in the in-process direction while stylus methods were progressing in the integrated direction. Stylus methods remain the most common and research into numerical methods to quantify surfaces has been extensive ranging from centerline and RMS averaging to frequency distributions [120].

A real surface can be considered to be made up of many bands of various wavelengths [121]. Longuet-Higgins first used spectral methods to characterize the wavelength distribution of sea waves [122]. The same approach can be used in the grinding wheel surface. The wheel profile will be made up of a series of wavelengths – or frequencies – depending on the grit diameter and spacing and the dressing conditions such as dressing lead [36]. In standard profilometry, errors are introduced such as misalignment between the motion of the stylus and the surface (usually low frequency) and electrical noise (usually high frequency). High-pass filters can be used to alleviate stylus/workpiece misalignment and low-pass filters can be used to alleviate electrical noise and vibration.

1.8.4. Asperity Density.

The surface topography of the wheel is a combination of random grits, bond, and voids in the matrix acted upon by the non-random action of the dressing diamond. Using statistics, Nayak modeled rough surfaces as two-dimensional, isotropic, Gaussian random processes and calculated the probabilities of encountering peaks and summits in them [116]. Although the surface of the grinding wheel is not random, Greenwood [120] applied Nayak's methods and discussed calculating the areal density of summits from the linear density of peaks and stated that

$$ n \approx 1.2\, n_d^2 \tag{40} $$

where n is the areal density of summits measured in summits/mm^2 and n_d is the linear density of peaks measured in peaks/mm. The constant of 1.2 takes into account the difference between the peaks traced out by the stylus – thus

underestimating the density of summits for a given elevation – and the summits in the real surface. Shaw and Komanduri [123] stated that there does not appear to be a way of directly determining the linear density without first determining the areal density. They examined the role of stylus curvature in determining the linear density of grits and calculated the areal density from the measured linear density by using a chisel-shaped stylus and dividing by the stylus width.

Backer [16] and Reichenbach [124] determined the number of active cutting asperities per unit area of the grinding wheel by rolling a dressed wheel over a soot-coated glass plate (estimated thickness 25 μm) and counting the number of contacts. For a grit size of 60 and a wheel grade of H, the value obtained was 4.5 aperities/mm^2 to 6.5 aperities/mm^2 depending on the dressing. However, as stated by Shaw [125], these values were too high. Malkin determined n by counting the number of wear flats produced on a grinding wheel by lighting the wheel surface at a glancing angle [27] and found approximately 1 active grain/mm^2 for an H grade wheel (wheel: 32A461-H8VG). Inasaki [126] and Suzuki and Inasaki [127] used optical profilometry and measured values of n ranging from 0.7 cutting edges/mm^2 to 1.9 cutting edges/mm^2 at a depth of 12 μm depending on the dressing conditions (wheel: MD140-N100M40). A CIRP co-operative study [128] differentiated between the number of cutting *grains* and cutting *points* per unit length and also between the number of *static* and *dynamic* cutting grains per unit length taking into account the kinematical trajectories of successive cutting points. It was found that the number of static grains at 10 μm depth was approximately 0.15 grains/mm and the number of static cutting points ranged from 0.4 points/mm to 2.5 points/mm depending on the laboratory doing the testing and the method used (wheel type: AA 54 K8 V). Comparisons between the values measured by various researchers are given in the table below.

Table 1.2. Asperity cutting point densities.

Reference	Grain size and grade	Density	Depth
[16][124]	60H	4.5 to 6.5 (/mm^2)*	25 μm
[27]	46H	1.0 (/mm^2)	***
[126]	140N	0.7 to 1.9 (/mm^2)*	12 μm
[128]	54K	0.15 (/mm) static grain	25 μm
[16] [124]	60H	0.4 to 2.5 (/mm) static point**	25 μm

*dressing dependent   **laboratory dependent   ***visible wear flat area

It can be concluded that, while asperity density is an important parameter in quantifying a grinding wheel, different approaches to measurement, different methods of differentiating static from dynamic cutting points and cutting points from grains, and different methods of calculating areal density from linear density can lead to large differences in values of areal cutting point density.

1.8.5. Asperity Slope.

Inasaki [126] and Suzuki and Inasaki [127] used optical profilometry to measure distributions of asperity angles for various dressing conditions. Using a cone-shaped model, they found a distribution of included angles ranging from 95° to 165° (attack angles 42.5° to 7.5°) with the majority of angles falling in the middle of the distribution with a mean included angle of 140° (attack angle 20°). They also found that, while a change in dressing lead did affect asperity densities, it did not significantly affect the distribution of asperity angles. As discussed earlier, numerous others have assumed attack angles in their models based on conical [95,127] or pyramid-shaped [100,110,102,2,3,4] asperities or spherical asperities [113,104,105] with attack angles tangent to the surface. Others have measured angles from profilometry [23,24,5,26] to be used in slip-line field models. Malkin discussed wear flat areas [17,27], which could be considered as changes in attack angles at the grain tips and Kopalinsky [77] discussed the differences between the two in temperature modeling. Whichever method of modeling of the grits is

employed, it is evident that the angle of the cutting asperities is important [129,23,24,130,5,65,1,57,86,100,113,102,104,105,72,77,68,67,17,47,63,103,109,48, 3,4,49,82,45,131,132] and a method of accurately measuring them would be of great assistance. Currently, profilometry appears to be the most useful, direct and easy to use.

CHAPTER 2. MODELS OF GRINDING WEAR.

The models described in CHAPTER 1 apply to abrasive processes in general. In applying a model of abrasion to the specific abrasive process of grinding, the slip-line field model of Challen and Oxley and the upper-bound method of Xie and Williams were each chosen to be used to predict the forces in grinding. The attack angles were measured by profilometry. The method of applying each of these models to grinding is discussed below.

The two models described here use a measured circumferential wheel profile to calculate the mean asperity attack angle (α) as a function of depth into the wheel (d_w). In addition, the 3-D model uses the areal asperity summit density (n) as a function of depth into the wheel from the profile. These distributions, the wheel and workpiece properties, the lubrication, and the grinding parameters are used to predict the normal force per unit width (F'_n) and the tangential force per unit width (F'_t) as a function of the equivalent chip thickness (h_{eq}). The equivalent chip thickness was as defined by Peters [11] as

$$h_{eq} = a_c \frac{V_w}{V_s} \tag{41}$$

where a_c is the depth of cut, V_w is the work speed and V_s is the wheel speed.

2.1. Application of 2-D Challen and Oxley Model to Grinding.

In applying the slip-line field models of Challen and Oxley, the grits in a grinding wheel can be represented as hard wedges. The equations for the normal and tangential force on each grit can be calculated from four parameters:

    (1) the depth it penetrates into the workpiece

    (2) the attack angle

    (3) the hardness of the workpiece and

(4) the shear strength of the lubricant film.

For cutting and plowing, the amount of metal removed can be simply related to the geometry of the field from Lacy and Torrance [25], Torrance and Parkinson [63] and Torrance and Buckley [26]. For rubbing, the forces generated are significant yet the wear rate is low. Any metal removal is by a process of low-cycle fatigue which is related to the contact ductility of the workpiece and the strain calculated to be imposed on the workpiece by the passage of a grit [25]. The hardness of the workpiece can be measured and the contact ductility can be approximately related to it and the melting energy of the workpiece material [25]. Previous tests have given figures for the shear strength of the interface [58,25,66,151]. Therefore, forces and metal removal rates can be related to the grinding parameters if the attack angles (grit slopes) can be measured from the wheel surface profile.

For each field, the normal and tangential stresses on the contact face of the grit, P_n and P_t, can be related to the attack angle of the grit, α, the friction factor at the interface between the grit and workpiece, f, and the shear yield strength of the workpiece, σ_y. The wear coefficient of the workpiece, K, can be related to the same parameters, plus the strain to failure of the workpiece material. The equations for F_n and F_t are given by Black, Kopalinsky and Oxley [66], whilst those for K are given by Torrance and Buckley [26]. Which of the fields applies for a particular combination of f and α can be determined by using the rules given by Torrance and Buckley [26].

A real grinding wheel will consist of an array of grits having a distribution of slopes which can be measured by profilometry [26]. If the probability of finding a slope between α and $\alpha + \delta\alpha$ is $P_\alpha \cdot \delta\alpha$, and the friction for a slope of α is μ_α, then for the abrasive surface the friction can be found approximately by the summation:

$$\mu = \frac{P_t}{P_n} = \Sigma\left(\mu_\alpha \cdot P_\alpha \cdot \delta\alpha\right) \qquad (42)$$

Similarly, the overall wear coefficient can be found as:

$$K = \Sigma\left(K_\alpha . P_\alpha . \delta\alpha\right) \tag{43}$$

An Abbott Curve is a function that gives the fraction of the length of the wheel/workpiece contact to the total profile length (b_a) versus depth into the wheel [134] – the bearing area – as shown in Figure 2.1.
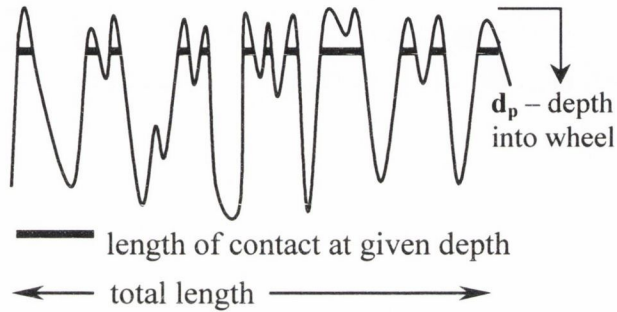
Figure 2.1. Bearing area.

It has been found that the fraction of length in contact is the same as the fraction of area in contact [134]. The average contact pressure over the arc of cut, p, is then given by $p = P_n \cdot b_a$. Therefore, the fraction of area of contact can be used with the average contact pressure over the arc of cut and the length of the arc of contact (l_a) to find the total normal force according to

$$F_n' = P_n \cdot b_a \cdot l_a \tag{44}$$

where l_a is the length of the arc of cut in the grinding wheel calculated from

$$l_a = \sqrt{a_c D_{wheel}} \tag{45}$$

Similarly, we can calculate the tangential force according to

$$F_t' = P_t b_a l_a \tag{46}$$

Beginning with the basic wear equation, the metal removal rate per unit length per unit time (Z') can be expressed as

$$Z' = K \cdot V_s \cdot F'_n \qquad (47)$$

and since the metal removal rate per unit width in grinding is defined as

$$Z' = a_c \cdot V_w \qquad (48)$$

We can substitute into the equation for h_{eq} to get

$$h_{eq} = \frac{Z'}{V_s} \qquad (49)$$

Substituting this back into the basic wear equation (47) we get

$$h_{eq} = K \cdot F'_n \qquad (50)$$

where the yield stress can be calculated approximately from the Vicker's hardness measurements by

$$\sigma_y = \frac{H \cdot g}{3} \qquad (51)$$

where g is the gravity constant (9.81 m/s^2).

Using this method, a software program has been written at Trinity College that predicts the normal and tangential forces in grinding as a function of the equivalent chip thickness. The inputs to the program are the measured wheel surface profile, the wheel dimensions and wheel grade, the material properties of the workpiece including the micro-hardness of the workpiece, the estimated interfacial friction based on the lubrication conditions, and the grinding speeds. To calculate the mean slope at a given depth, the program divides the profile into three sections from the

top peak to the lowest valley and then divides the top section of the wheel profile into two hundred intervals. Within each interval, the slope of the asperity is found and a distribution of mean slope with increasing depth into the wheel is determined. This mean slope is used as the attack angle in the model. For a given depth, the corresponding equivalent chip thickness is calculated, the corresponding mean attack angle is found and, using the estimated value of f, the normal and tangential forces are calculated as a function of the equivalent chip thickness from the above equations. In effect, a theoretical grinding chart of F'_n and F'_t versus h_{eq} is created. The results of the model for grinding of EN31 specimens for three dressing conditions were first published in [24]. These results, along with additional results for other material types and wheel types, are given here.

The model uses values taken from surface hardness measurements on the workpieces. It does not take into account the effect of strain-hardening. As was found by previous researchers [65,66,58,68,67], the effects of strain-hardening can be significant. Although hardened steels do not have a large degree of strain-hardenability, it is, nevertheless, a handicap that these effects are not considered. Secondly, the model does not take into account the effects of the elevated temperatures on the hardness values. Temperatures in the grinding zone can be 900 °C and higher causing hardness to drop. In contrast, the large strain rates imposed by grinding have the effect of raising the yield stress and hardness values. Therefore, it is assumed in this model that, although these parameters are significant, they tend to cancel each other out. Further development of the model would investigate if one of these parameters may be dominant. This is given further attention in the discussion (Section 5.2.9, page 129).

Brenner and Torrance [23] used Challen and Oxley's slip-line field method and applied it to grinding to predict grinding forces from measured wheel profiles. Badger and Torrance [24] further developed the model and applied it to the grinding of hardened steel. Results were satisfactory, but because of the assumptions of plane-strain, it was decided to also apply the three-dimensional model of Xie and Williams [4] to further develop the model and assess the validity of the assumptions in the two-dimensional model.

2.2. Application of 3-D Xie and Williams Model to Grinding.

Xie and Williams model of abrasion takes into account the simultaneous rubbing, plowing and cutting that is present in grinding. The parametric formulae for friction and wear rates make it applicable to many abrasive processes. It uses surface and bulk hardness which is more readily available than determining yield stress as a function of strain and estimating the corresponding strains. The use of overlapping wear tracks appears to be a more realistic representation of the real wear process. Most notably, the model allows for the simultaneous plowing, rubbing, prow formation and cutting which is more realistic than the either/or scenario of other models. For these reasons, it seemed prudent to apply this work in the development of the model of abrasion to the measured topography and grinding force measurements to see how well it could predict the forces in grinding.

A software program based on the model of Xie and Williams has been developed at Trinity College that predicts the normal and tangential forces in grinding as a function of the equivalent chip thickness. The inputs to the model are the asperity slope and density distributions from the measured wheel profiles, the grinding conditions, the estimated value of f, and the workpiece material properties. The method of applying Xie and Williams model and equations for abrasion to grinding are described below.

2.2.1. Calculation of Forces and Equivalent Chip Thickness.

The first step in applying Xie and Williams equations for friction coefficient and specific wear rate (page 48) to grinding is to relate the normal and tangential forces and equivalent chip thickness found in grinding to those parameters used by Xie and Williams for single grit tests.

The metal removal per grit per unit time (Z_g) can be expressed from the basic wear equation as

$$Z_g = K \cdot V_s \cdot N \qquad (52)$$

where N is the load of the asperity and V_s is velocity of the contact (the wheel speed in grinding). If we assume that the load is equal to the product of the hardness of the workpiece and the area of contact equal to the square of half the scratch width, we get

$$Z_g = K \cdot V_s \cdot a^2 \cdot H_s \tag{53}$$

where H_s is the surface hardness of the material and a is the half scratch width defined by

$$a = \frac{h}{\tan \alpha} \tag{54}$$

where h is the depth of penetration and α is the attack angle. If we introduce the areal asperity density (n_g, asperity points per unit area) to change the wear rate from a per grit form to a per unit area form and then normalize it per unit width we get

$$Z' = K \cdot V_s \cdot a^2 \cdot H_s \cdot l_a \cdot n_g \tag{55}$$

where l_a is the length of the arc of cut in the grinding wheel calculated from

$$l_a = \sqrt{a_c \cdot D_{wheel}} \tag{56}$$

and D_{wheel} is the wheel diameter and a_c is the depth of cut. The equivalent chip thickness was defined earlier as

$$h_{eq} = \frac{a_c \cdot V_w}{V_s} \tag{57}$$

where V_w is the work speed. If we solve for a_c in (57) and substitute it into (56) we get

$$l_a = \sqrt{\frac{D_{wheel} \cdot V_s \cdot h_{eq}}{V_w}} \qquad (58)$$

Since the metal removal rate per unit width is defined as

$$Z' = a_c \cdot V_w \qquad (59)$$

we can substitute into the equation for h_{eq} to get

$$h_{eq} = \frac{Z'}{V_s} \qquad (60)$$

Substituting the original equation for Z' into the above gives

$$h_{eq} = K \cdot a^2 \cdot H_s \cdot l_a \cdot n_g \qquad (61)$$

If we substitute in the basic equation for l_a we get

$$h_{eq} = \left(K \cdot a^2 \cdot H_s \cdot n_g\right)\sqrt{a_c \cdot D_{wheel}} \qquad (62)$$

We can now substitute the equation for h_{eq} into the a_c term to get

$$h_{eq} = \left(Ka^2 H_s n_g\right)\sqrt{\frac{h_{eq}V_s}{V_w} D_{wheel}} \qquad (63)$$

If we square both sides and solve for h_{eq} we get

$$h_{eq} = \left(Ka^2 H_s n_g\right)^2 \frac{V_s \cdot D_{wheel}}{V_w} \qquad (64)$$

so that now we have for a grinding chart an independent variable h_{eq} which is in terms of parameters that are known or that can be measured. To find the dependent variables F'_n and F'_t we start with the basic wear equation to get

$$\dot{V}' = K \cdot \frac{L_{scratch}}{\Delta t} \cdot F_n' = K \cdot V_s \cdot F_n' = K \cdot \frac{a_c V_w}{h_{eq}} \cdot F_n' \qquad (65)$$

where $\dot{V}'$ is the wear per unit time per unit width.

We can use the fact that $\dot{V}' = Z' = a_c \cdot V_w$ to get

$$K \cdot \frac{a_c V_w}{h_{eq}} \cdot F_n' = a_c \cdot V_w \qquad (66)$$

Now we can solve for the dependent variable F_n' in terms of the equivalent chip thickness and F_t' from the basic equation to get

$$F_n' = \frac{h_{eq}}{K} \qquad (67)$$

$$F_t' = \mu \cdot F_n'. \qquad (68)$$

so that all necessary parameters are either known or can be measured. F_n' and F_t' and h_{eq} are the variables in the grinding chart and the equations for K and μ from Xie and Williams are available. The equations are valid when F_n' and F_t' are in N/mm, h_{eq} is in mm, K is in (1/MPa) and V_w and V_s are in m/s.

2.2.2. Transitional Attack Angles, Friction and Wear Tracks.

Once the asperity slope distribution and the asperity density distribution have been measured, the forces can be calculated as a function of the equivalent chip thickness. An approximation can be made for f from previous results. Therefore, an estimate for the dimensionless distance between adjacent tracks needs to be made. Xie and Williams found that for values of the dimensionless distance between adjacent

tracks (l) less than 0.2, the values of μ and K cease to change with any further decrease in l [4]. They also stated that for small values of l, the transition from plowing to cutting occurred at an attack angle of $\alpha \approx 6°$ for H_s/H_b=1.0 and $\alpha \approx 12°$ for H_s/H_b=1.25 (Section 1.7.3, page 45). These values were for conditions when f=0.5. Xie and Williams defined f^H in [2] as $f^H=\tau/H$ and consistently stated in [4] that $f^H \approx 0.1$ for oils and $f^H \approx 0.2$ for dry contact. Therefore, converting to

$$f = \frac{\tau}{k}$$

from

$$f^H = \frac{\tau}{H}$$

as discussed in Section 1.3.1 (page 12), we can use the fact that for most metallic materials

$$k = \frac{H}{3\sqrt{3}}. \tag{69}$$

They gave a value for oil of

$$f=0.5.$$

This value seems unreasonably high for oil-lubricated contact. If we consider the wear map given in Figure 1.17 (page 47), the transitional angles for cutting at l=0.2 are about 7° for no strain-hardening and about 12° for strain hardening of H_s/H_b=1.25.

The materials tested here are hardened steel which does not strain-harden appreciably. The angles measured by previous researchers in grinding and for the angles measured here through profilometry lie in the region to the right of the transitional angle from plowing to cutting on the map. Considering this, the fact that

in grinding the lubrication conditions will be much better than those in Xie and Williams's wear map with f=0.5,. and the fact that the conditions in grinding will produce many overlapping tracks, it is reasonable to assume that the regime of wear is micro-cutting and a value of l=0.2 can be used in Xie and Williams's equations for μ and K for micro-cutting.

Therefore, for a given depth into the wheel, all the parameters are known for calculating μ and K. The values of surface and bulk hardness and shear yield stress can be measured, the attack angles can be measured through profilometry, f can be estimated from previous measurements and l=0.2 can be used for the dimensionless distance between tracks. Once K and μ are known, h_{eq}, F'_n and F'_t can be calculated as shown in Section 2.2.1 (page 63) and a theoretical grinding chart can be plotted for a given set of grinding conditions.

2.2.3. Effect of Using Mean Slope on Specific Wear Rate Equation.

In the application of Xie and Williams's equation for μ and K to grinding, a mean slope for a given depth into the wheel was used in the calculations. In reality, there will be some distribution of slopes at a given depth into the wheel. Since the equation of μ depends linearly on $\tan(\alpha)$, applying a distribution of $\tan(\alpha)$ around the mean value in the equation of μ will still yield the same results as using the mean value of $\tan(\alpha)$ provided the distribution is symmetrical. However, the equation for K depends on $\tan^3(\alpha)$ so that it is no longer adequate to calculate K from the mean absolute slope. We can resolve this by applying a normal distribution around α and determining how K would vary with this change.

Setting $\tan \alpha = s$, we can evaluate the following integral:

$$I = \left(\int_{-\infty}^{\infty} P(s) \cdot s^3 ds \right)^{\frac{1}{3}} \frac{1}{\alpha_{qs}} \tag{70}$$

where α_{qs} is the RMS slope of the grits in contact. If *P(s)* represents a normal probability distribution, then the result of evaluating the integral is

$$I = 1.185.$$

Therefore, considering a normal distribution around $\tan(\alpha)$ effectively increases it. This is because values to the right of the mean line in the distribution will be affected by the cubic term to a greater extent than those values to the left of the mean line. We may then calculate *K* by modifying equation (37)

$$K_{cutting} \approx 0.003 \frac{\left(I \cdot \alpha_{qs}\right)^3}{fkl^{0.5}} \sqrt{\frac{H_b}{H_s}} \tag{71}$$

where, as stated earlier,

$$k = \frac{H_b}{3\sqrt{3}}.$$

If we plot the values of *K* as a function of cutting angle with and without the applied normal distribution we can see the effect. This is shown in Figure 2.2 (values for H_s, H_b, *f*, *etc.* the same as those used in calculations for EN31 experiments). Here we can see that the effect of distributed angles is not insignificant and therefore should be included in the calculations. The use of the normal distribution resulted in an effective increase in *K* of 66%.
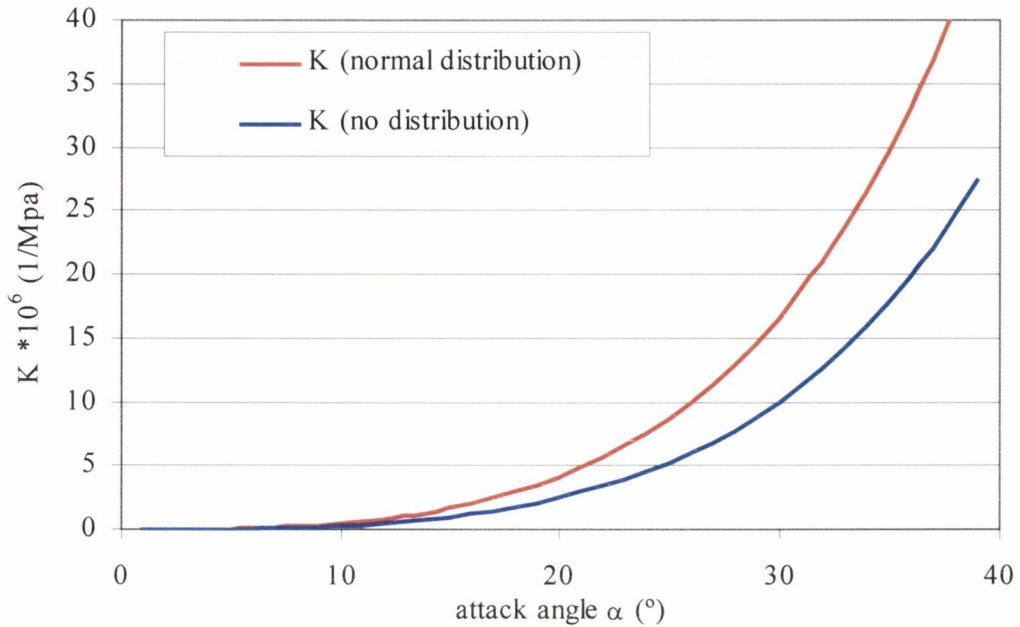
Figure 2.2. Effect of distribution on specific wear rate.

2.2.4. Effect of Strain-Hardening.

Xie and Williams developed their model to use values of surface and bulk hardness rather than a stress-strain relation because, in practice, they are easier to measure. As discussed earlier, materials that have a higher strain-hardening ability have a larger transitional angle (α_{trans}) from plowing to cutting. In other words, ductile materials have a higher tolerance to being displaced (plowed) before breaking free. This is illustrated in Figure 2.3, a plot of the minimum attack angle where cutting may occur regardless of the dimensionless distance between adjacent tracks, $\alpha_{c, trans}$, versus the ratio H_s/H_b from Xie and Williams's equations for minimum attack angle, page 46. Here we can see that as the material strain-hardens, the required angle for cutting gets larger. In addition, as lubrication improves, the transitional angle from cutting to plowing gets smaller. For lubrication conditions appropriate to grinding of hardened steels ($f \approx 0.1$ for oil, $f \approx 0.4$ for water-based soluble oil, $H_s/H_b \approx 1.0$ to 1.2), the attack angle is about $9 \sim 12°$ for oil and about $18 \sim 25°$ for soluble oil.

70
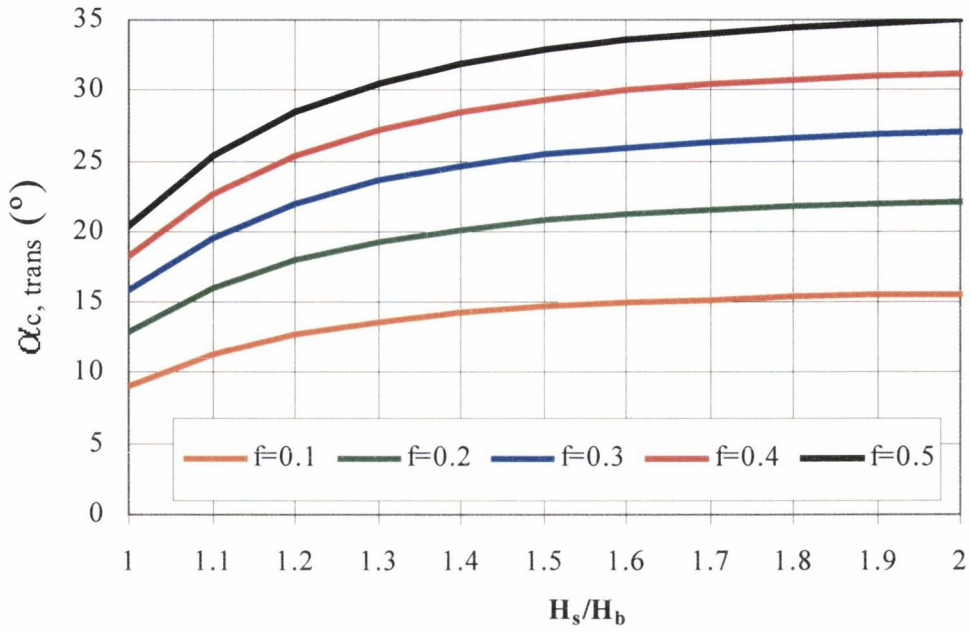
Figure 2.3. Effect of strain-hardening on transitional attack angle.

The effect of strain hardening on specific wear rates is plotted in Figure 2.4 below (for EN31 tests, H_s/H_b=1.1). It shows that, while the coefficient of friction is independent of H_s/H_b, the specific wear rate, which depends on H_s/H_b, is affected to some extent by the strain-hardening that occurs when grinding bearing steel specimens.
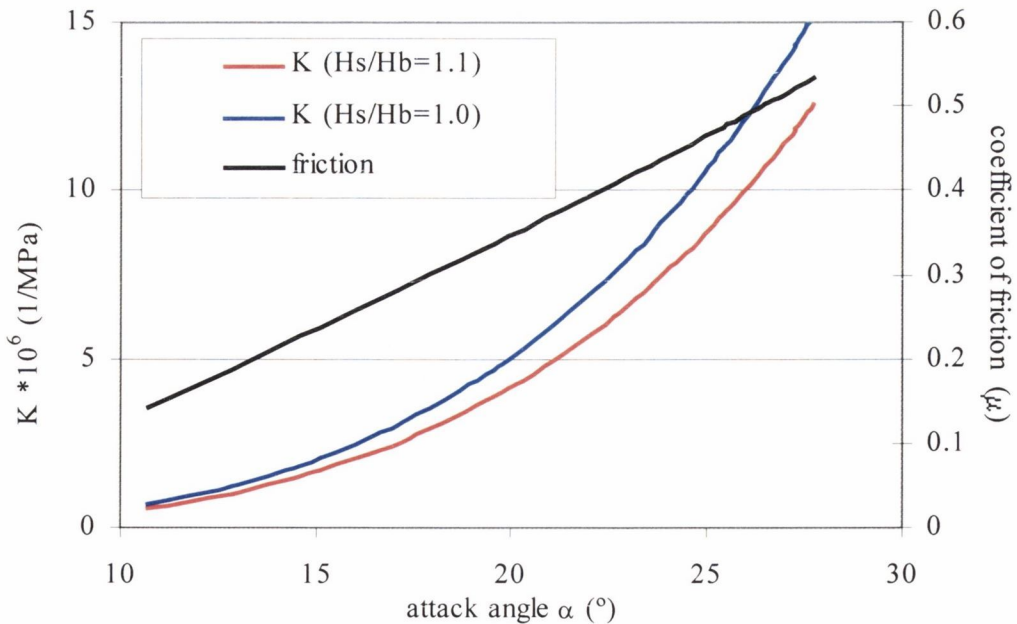
Figure 2.4. Effect of strain hardening on specific wear rate and friction.

2.2.5. Efficiency and Specific Energy.

If we look at the efficiency of the abrasive process as applied to grinding, we can begin with the definition of specific energy and use the equations given in Section 2.2.1 (page 63) to arrive at

$$e = \frac{F_t' \cdot V_s}{a_c \cdot V_w} = \frac{F_t'}{h_{eq}} = \frac{\mu \cdot F_n'}{h_{eq}} = \frac{\mu \cdot}{K} \tag{72}$$

where the specific energy, e, is in J/mm^3, h_{eq} is in mm and V_w and V_s are in m/s. From this, we can plot specific energy versus μ as shown in Figure 2.5 below. Here we can see that as the ratio of F_t to F_n (μ) increases, the specific energy decreases. This is because cutting is a more efficient metal removal process than rubbing and plowing. The value of μ is much higher for cutting – say, for example, as in turning – than is the value of μ for plowing. In the equation, larger values in the top term, μ, will tend to increase specific energy. Typical values for μ in grinding with neat oil tend to be around 0.3 and typical values for grinding with water-based soluble oil tend to be around 0.5. The reduced frictional forces and the enhancement of cutting that results in grinding with oil tend to decrease the value of μ. In contrast, increased lubrication will also tend to increase specific wear rates in the bottom term. According to the plot, this means that grinding with oil should lead to lower specific energies. This was found to be true in the results of Snoeys and Peters [10] who found, for the same grinding conditions, the specific energy drop from 48 J/mm^3 for soluble oil to 28 J/mm^3 for neat oil, which happen to line up well with the values in the graph.
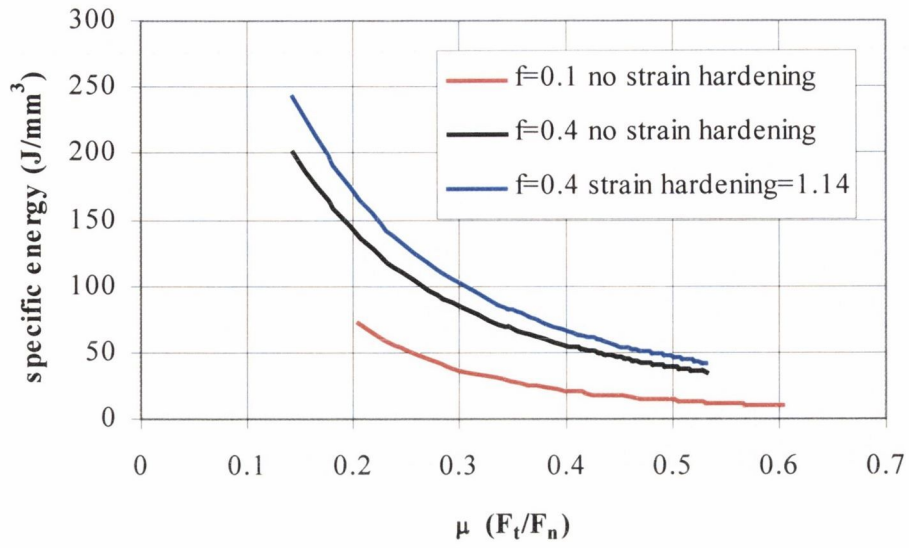
Figure 2.5. Efficiency of abrasive process.

CHAPTER 3. GRINDING EXPERIMENTAL SET-UP.

The experimental set-up consisted of a surface grinder which used a dynamometer to measure grinding forces and an LVDT to measure table speeds. A profilometer was used to measure the circumferential surface profiles of the wheel.

3.1. Grinding Machine.

The grinding machine used for the experimental work was a Jones and Shipman 540P that was modified to accommodate creep-feed grinding as shown in Figure 3.1. The wheel was driven by a 6 horsepower (4.5 kW) motor capable of wheel speeds of 15 m/s or 31 m/s (D_{wheel}=200 mm, 1440 RPM or 2910 RPM). The table traverse was driven hydraulically. Reliable and steady creep-feed speeds were achieved as low as 5 mm/s.

Coolant was supplied by a Hydra-Cell D10 positive displacement pump with a constant flow rate of 26 liters/minute with a relief valve capable of pressures up to 70 bar. The nozzle used for tests with soluble oil coolant was a 10 mm diameter copper pipe located just in front of the grinding zone with a coolant flow rate of 18.9 liters/minute which produced an average coolant velocity of 4.0 m/s. In creep-feed grinding, it is highly desirable to have coolant velocities approaching wheel velocities in order to avoid workpiece burn [135,46,136]. Therefore, for creep-feed grinding and tests using neat oil, the nozzle was crimped to a rectangular shape (width=11.4 mm, height=1.0 mm) and directed into the grinding zone yielding a coolant flow rate of 12.6 liters/minute which produced an average coolant velocity of 18.4 m/s.

The specimen (length=110mm, width=18 mm, height=20 mm) was mounted in a housing that was bolted to a Kistler 3-axis piezoelectric dynamometer as shown in Figure 3.2 and Figure 3.3. During grinding, the dynamometer measures the normal and tangential forces on the workpiece (F_n and F_t) and the LVDT measures table velocity (V_w). The signals are sent to a PC. A fume extractor is used to remove atomized coolant and dust.
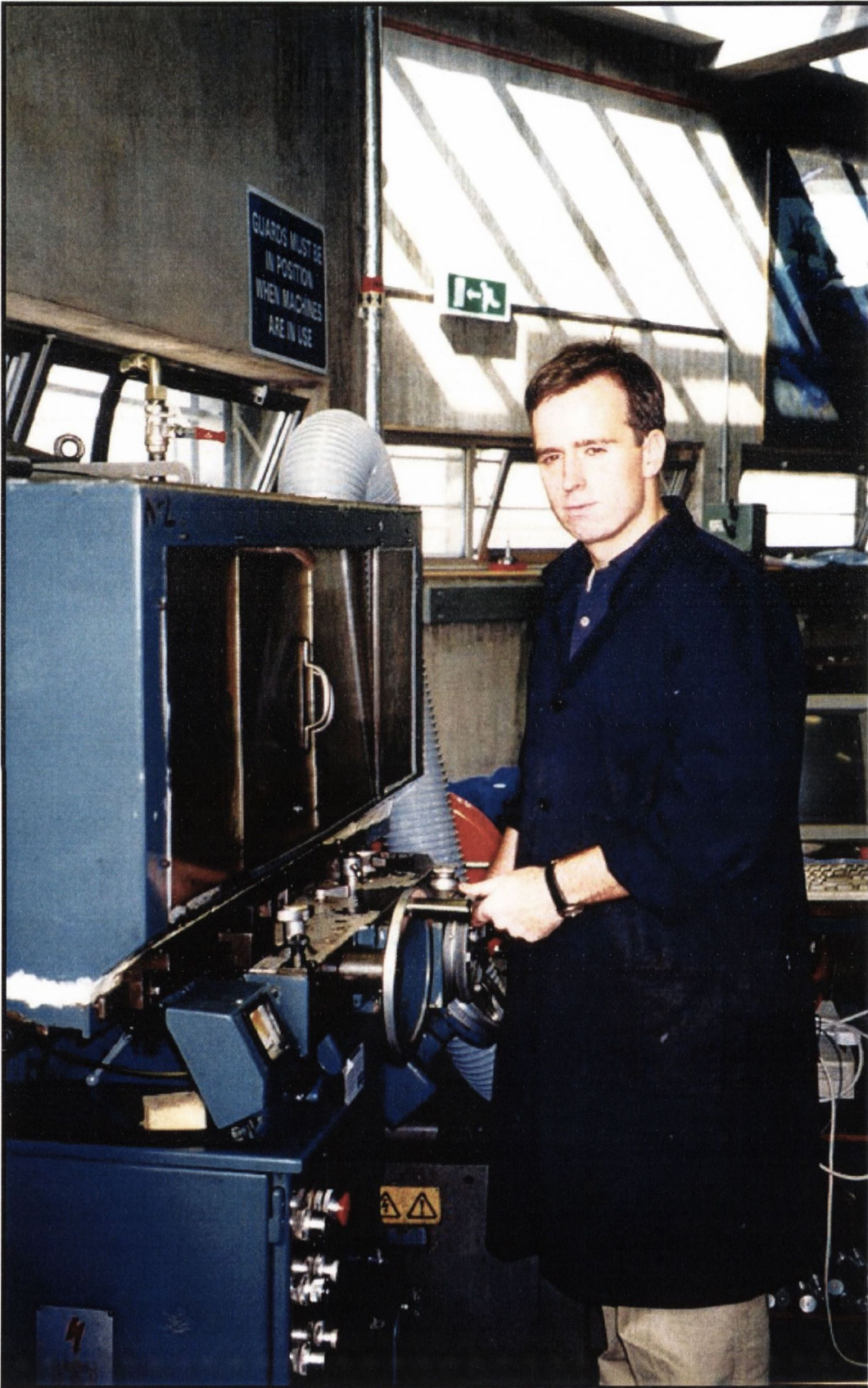
Figure 3.1. Jones & Shipman surface grinder used in experiments.
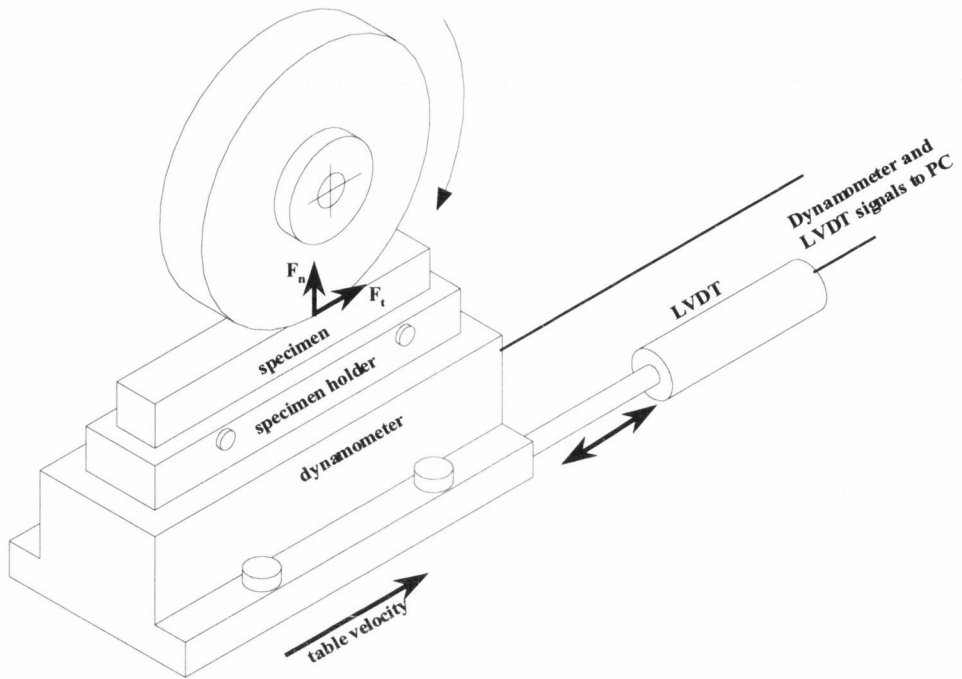
Figure 3.2. Measurement of grinding forces and speeds.
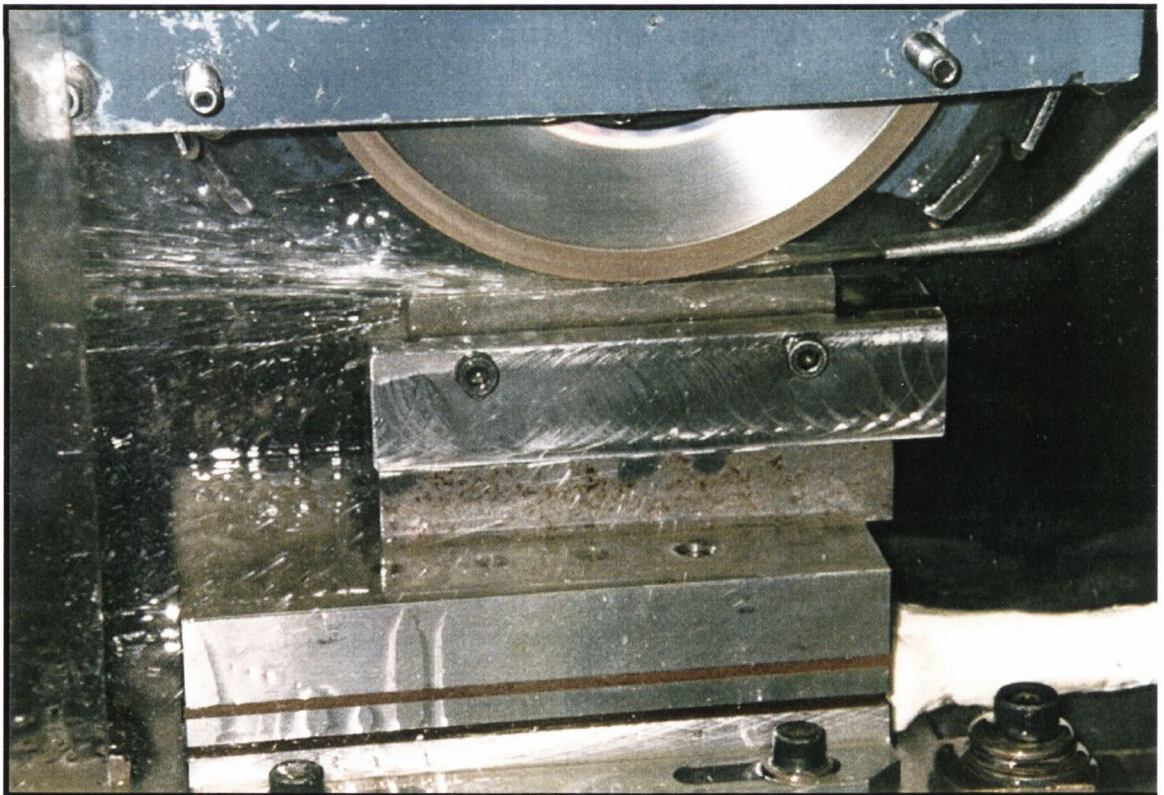
Figure 3.3. Specimen mounted to dynamometer.

3.2. Wheel Truing and Dressing.

The truing and dressing of the wheel was performed before each set of grinding tests. For the vitrified alumina and resinoid alumina wheels, a three-diamond Unicorn D25 in-line dressing tool was used. Each of the three diamonds had a base diameter of 0.8 mm. In order to ensure constant dressing velocities and accurate and repeatable dressing, a stepping-motor was affixed to the cross-feed hand wheel. The stepping-motor was connected to a PC which controlled the speed. The procedure was as follows. The appropriate dressing velocity was determined for the desired dressing lead and programmed into the stepping-motor controller. The dressing tool was passed under the wheel by means of the stepping-motor arrangement. Before each pass, the in-feed was incremented to the desired dressing depth. Several dressing passes were made while incrementing the in-feed before every pass until a total dressing depth greater than the mean grit diameter was achieved to ensure any residual loading of the wheel was dressed away. Finally, a reverse dressing pass and another forward dressing pass were made without incrementing the in-feed. Coolant was used throughout. For the CBN wheel, a rotary brake rotary diamond dresses was used with the stepping-motor used for the table cross-feed.

3.3. Experimental Procedure.

The experimental procedure was as follows. The wheel was dressed according to the procedure described above and then brought into contact with the workpiece. The desired table velocity was set. The wheel was brought into contact with the workpiece. For pendulum grinding the entire wheel width was used (20 mm). For creep-feed grinding a smaller width of cut was used ($\approx$2 to 3 mm). For pendulum grinding, several grinding passes were taken while incrementing the in-feed before every pass. Normal and tangential forces and table velocities were measured throughout. Grinding continued while incrementing the in-feed before every pass until forces increased to a steady-state value, after which grinding was halted. This usually required three to five passes. Because of the stiffness of the wheelhead and the tendency of the wheel to "climb" over the workpiece until spark-out was

achieved, this procedure was necessary to ensure that the in-feed that was set on the machine was the same as the actual grinding depth of cut. It is assumed that, after the forces reached a steady-state value, the incremented in-feed taken before each pass was the same as the actual depth of cut during grinding. This method was validated by comparing the total in-feed to the actual measured depth of cut. This method was used to avoid the difficulty of measuring the actual depth of cut after every pass and successfully avoided the large scatter observed by other researchers [11,7,26]. For creep-feed grinding, a single pass was taken and the actual depth of cut was measured with a micrometer. This was more than sufficient for achieving the desired accuracy.

3.4. Data Acquisition.

Data acquisition was performed using the DASH300 data acquisition software with a PC26AT analogue-to-digital card on a PC with a 486 processor. Each of the two signals from the dynamometer was sent to a charge amplifier where it was amplified 20 times (100 times for smaller forces) and filtered using a 10 Hz low-pass filter. It was then sent to the A/D card on the PC. The output of the LVDT was sent directly to the A/D card. The data for a given grinding test were saved and then later downloaded to a spreadsheet where the voltages were converted to forces and displacements based on the calibrations. Calibration data are given in Appendices 3 and 4. An example is shown in Figure 3.4. It can be seen that the forces increase until they reach a steady-state value where the depth of cut that was set on the machine was equal to the actual depth of cut. Once this was achieved, force readings (F_n, F_t) are taken for the forward pass (up-grinding) and the average velocity was calculated from the LVDT readings.
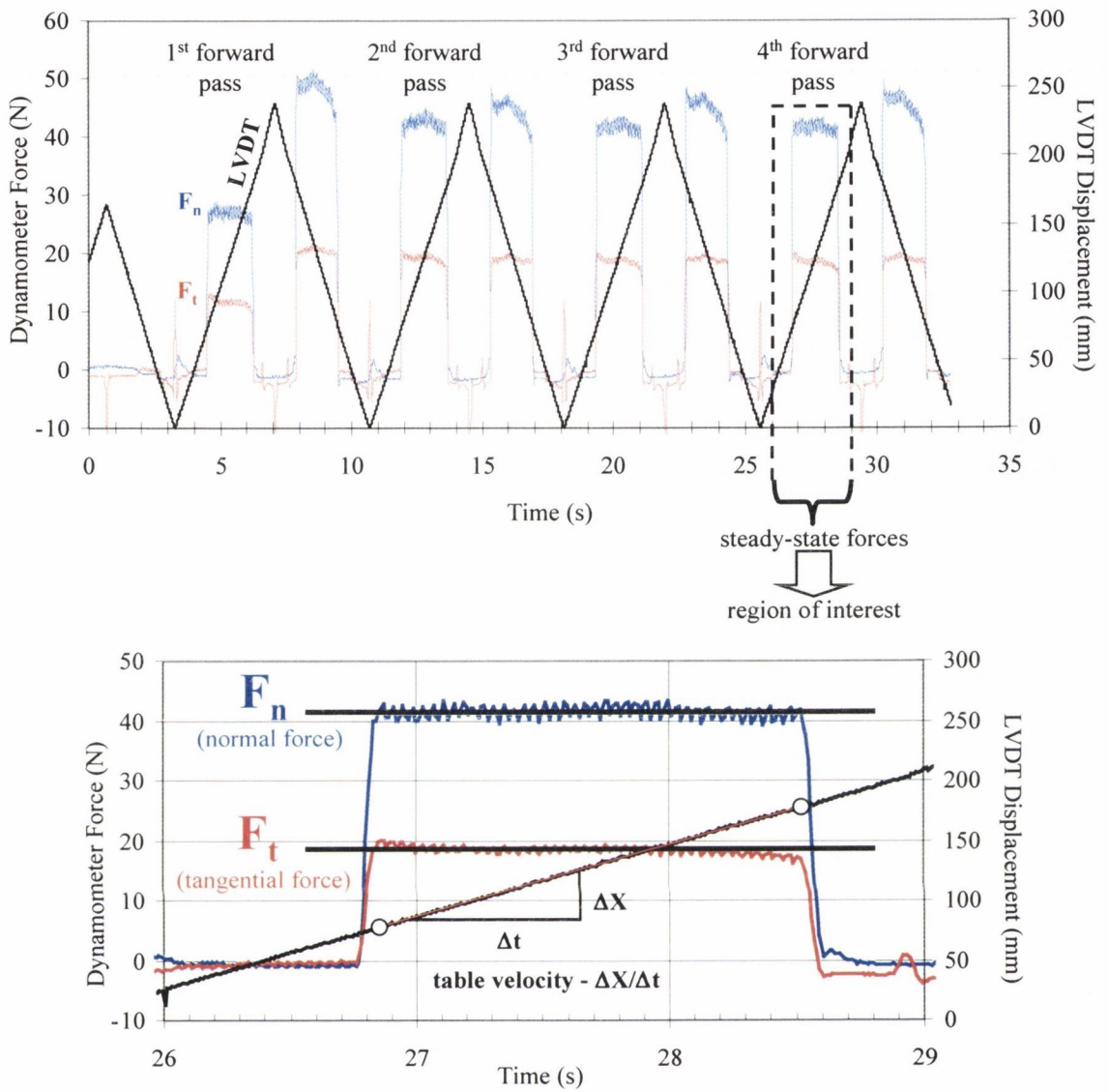
Figure 3.4. Example of grinding force and LVDT signals.

3.5. Wheel Profile Experimental Set-up.

A method of measuring the asperity density and the asperity slope was needed for the attack angle required in the models. Shaw and Komanduri [123], Verkerk [128], Torrance and Buckley [26] and Brenner and Torrance [23] successfully used profilometry to characterize the grinding wheel surface. Surface profiles of the grinding wheel were measured using a Hommel surface profilometer. The set-up is shown in Figure 3.5 and details are given in Table 3.1.
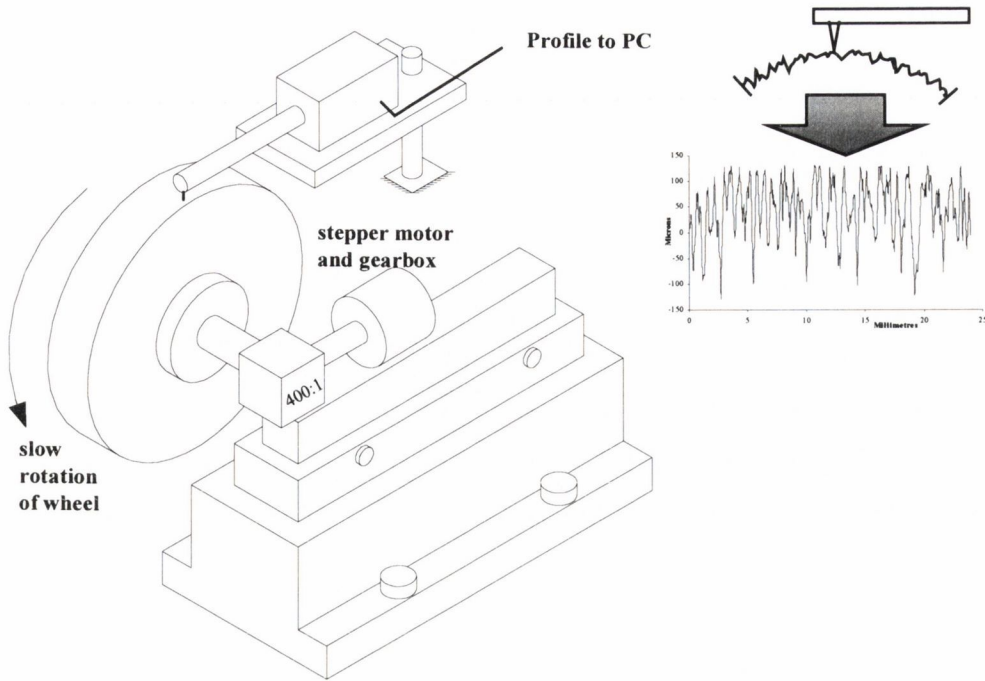
Figure 3.5. Measurement of circumferential wheel profiles.

Profiles were measured in two directions: circumferential and axial. Circumferential profiles were measured by resting the tip of the stylus on the top of the wheel and rotating the wheel at very slow speeds by means of the stepping-motor which was affixed to a 400:1 gearbox in order to achieve reliable, constant, low velocities. The rotational speed of the motor was adjusted based on the wheel diameter so that a constant surface speed of 0.2 mm/s was achieved. The signal from the profilometer was then sent to an A/D card and processed on a PC. The distance between samples was either 4 µm or 8 µm depending on wheel type. Several measurements were taken using a 1 µm distance but the increased resolution did not yield more accurate results when calculating asperity densities and asperity slopes. Further attention is given to this in the Results section. In addition, finer resolution meant much more data logging was required to achieve the same sample length. Axial profiles of the wheel were also taken. However, because the wheel was true, because axial profiles required additional filtering that was not necessary for circumferential profiles, and because the models required angles measured in the circumferential direction, circumferential profiles were therefore used. Calibration data are given in Appendix 2.

Table 3.1. Profilometer details.

Profilometer	Hommel T2-2 tip radius=2.5 μm tip included angle=90°
Maximum penetration	300 μm
Maximum slope measured	1.0 (45°)
Surface speed	0.2 mm/s
Sampling rate	50 Hz = 4 μm/sample for Resinoid Alumina Wheel 25 Hz = 8 μm/sample for Vitrified Alumina Wheel 25 Hz = 8 μm/sample for CBN Wheel
Sample length	Circumferential profiles: 32 mm for RA Wheel Circumferential profiles: 64 mm for VA Wheel Circumferential profiles: 64 mm for CBN Wheel *Several profiles taken after dressing and after grinding

CHAPTER 4. EXPERIMENTAL MATERIALS AND RESULTS.

Grinding experiments were performed for a variety of wheel types, workpiece types and coolant types. Forces were measured during grinding and wheel profiles were taken after dressing and after grinding.

4.1. Forces.

Pendulum grinding tests were performed on EN31 and case-hardened EN39B specimens with a vitrified alumina (VA) wheel and soluble oil coolant for three dressing conditions (set 1 and set 2). Creep-feed grinding tests were performed on M2 specimens with a resinoid alumina (RA) wheel and neat oil for two dressing conditions (set 3). Pendulum grinding tests of EN31 and EN39B and creep-feed grinding tests of M2 were performed using a vitrified CBN wheel and neat oil (set 4). The procedure was as follows:

- Wheel was dressed.
- Circumferential profiles were taken of the dressed wheel surface.
- Grinding tests were performed, normal and tangential forces were measured.
- Circumferential profiles were taken of the worn wheel surface.
- Surface hardness measurements were taken on the ground surface. Bulk hardness measurements were taken on the non-ground surface.
- A roughness measurement was taken of the ground workpiece.
- Surface profiles and force measurements were processed on a PC.
- Asperity density and asperity slope distributions were calculated from several wheel profiles.
- The 2-D model and the 3-D model were applied to the distributions from the profile along with the hardness values and grinding parameters to predict the normal and tangential forces as a function of equivalent chip thickness.

The composition, heat treatment and mechanical properties of the workpieces and the details of the grinding tests are given in the tables below.

Table 4.1. Composition, hardness and heat treatment of steels.

Steel	Bulk Hardness at 27°C	C	Si	Mn	Ni	Cr	Mo	S	Ph	W	V
EN31	738 Hv	1.05	0.23	0.73	0.23	1.5	0.21	0.028	0.03		
EN39B	633 Hv	0.12	0.1		3.8	1.0	0.15				
M2	860 Hv	0.90				4.2	5.0			6.4	1.8

Heat Treatment	
EN31	Harden at 450 °C 6 hours, Quench in 60 °C oil for 15 minutes, temper in air 220 °C for 90 minutes.
EN39B	Carburize at 880 °C, Refine at 850 °C, Harden at 760°C in oil, temper at 200 °C
M2	Harden at 1220 °C, Quench in salt, two annealings at 560 °C.

Table 4.2. Grinding and dressing parameters.

Set 1 and Set 2	
Wheel	Vitrified alumina: WA 60 HV (D_{wheel}=200 mm)
Workpieces	Set 1: EN31 – pendulum grinding
	Set 2: EN39B – pendulum grinding
Coolant	Castrol Hysol X Soluble Oil, 4% dilution in water
Dressing	i) s_d=200 μm, a_d=5 μm (fine dress)
	ii) s_d=200 μm, a_d=30 μm (medium dress)
	iii) s_d=200 μm, a_d=60 μm (coarse dress)
	(two finishing passes)
Grinding	Table speed: 0.05 m/s to 0.25 m/s
	In-feed: 2.5 μm to 20 μm

Set 3	
Wheel	Resinoid alumina: WA 1008 R19B HPAA (D_{wheel}=200 mm)
Workpiece	M2 – creep-feed grinding
Coolant	Castrol Vacmul 2105 Neat Oil
Dressing	s_d=200 μm, a_d=12.7 μm
	s_d=400 μm, a_d=12.7 μm
	(two finishing passes)
Grinding	Table speed: 8 mm/s to 30 mm/s
	In-feed: 0.48 mm to 1.9 mm

Set 4	
Wheel	Vitrified CBN: B91ABN200 (D_{wheel}=175 mm)
Workpiece	EN31, EN39B – pendulum grinding, M2 – creep-feed grinding
Coolant	Castrol Neat Oil
Dressing	Brake Rotary, s_d=8 μm, a_d=2.5 μm ($D_{dresser}$=84 mm)
Grinding	Same as above for respective workpieces

An example is given in Figure 4.1 which shows the results from Set 1 – grinding of EN31 with a vitrified alumina wheel for three different dressing conditions – fine, medium and coarse. Results are given on log-log scale typical of grinding charts. Experimental points are plotted and a least square fit is represented by a line. Here the linear relationship is evident. For additional clarity, results are also plotted on a standard linear scale with the least square fit from the log-log scale given again by the line.

From the figure, we can see that it is evident that the forces for the fine dressing are larger than those of the medium and coarse dressing. The forces for the medium and coarse dressing are approximately the same with the tangential forces being slightly

lower for the coarse dress. This indicates that the increase in dressing depth from 5 μm to 30 μm is significant, but that the increase from 30 μm to 60 μm has less effect.

The results from Sets 2, 3 and 4 are given later with the predictions of the dressing model.
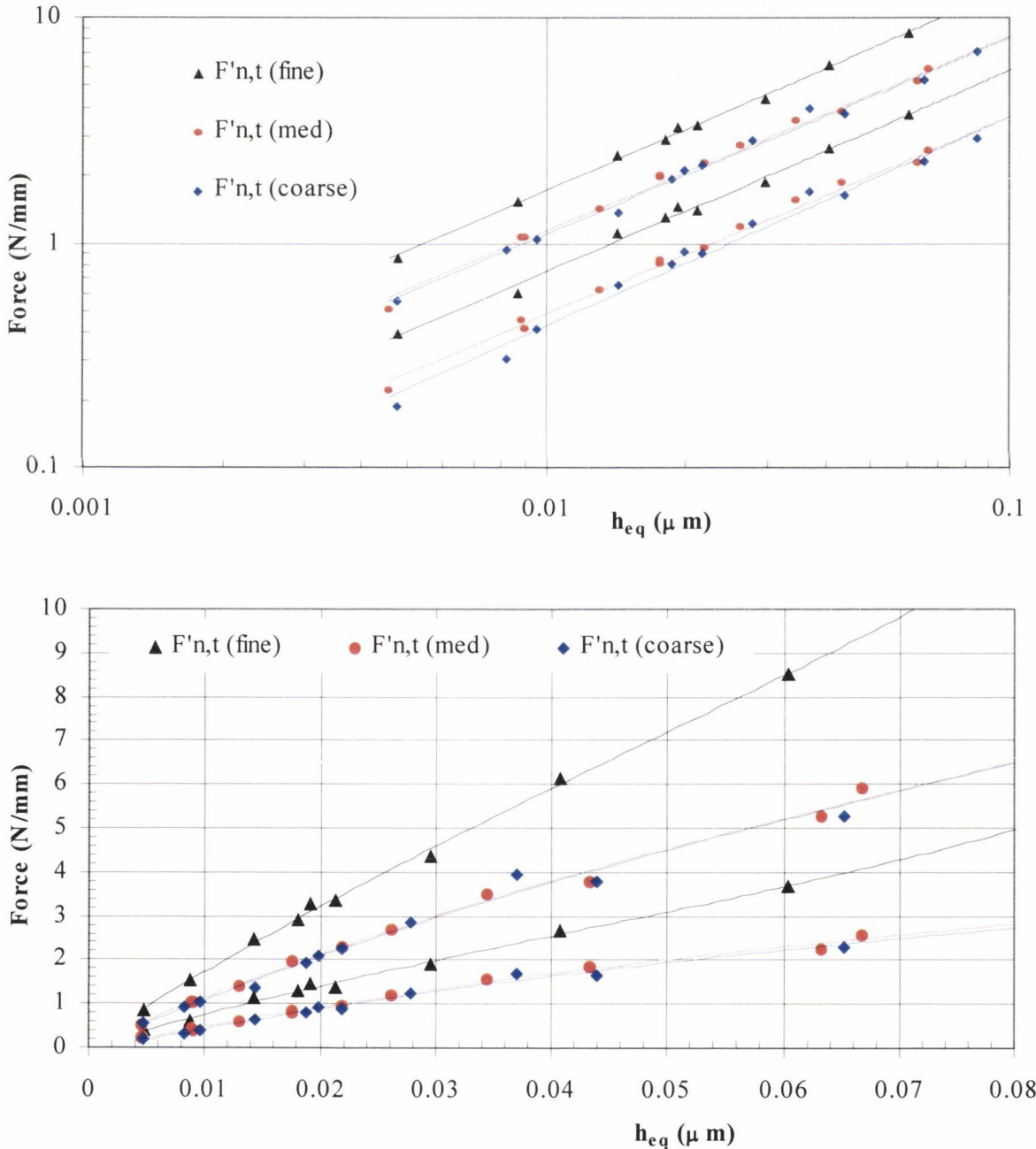
Figure 4.1. Set 1: grinding forces of EN31, VA wheel, three dressings.

4.2. Wheel Profiles.

Circumferential profiles were taken after dressing and after grinding for all tests. The profiles were recorded and downloaded to a PC where they were processed using a spreadsheet. The asperity densities and asperity slopes were calculated.

4.2.1. Filtering.

The first step in processing of the profile was to filter out any unwanted high frequency noise and unwanted low frequency waviness. An example of a profile smoothed according to Torrance [48] (smoothing length = 4 mm, 3 times) is shown in Figure 4.2 (vitrified alumina wheel, medium dressing, a_d=30 μm, s_d=200 μm). This shows a region of the profile where smoothing had the largest effect. It is evident that filtering did not significantly affect the profile. Peaks at lower depths into the wheel were elevated slightly while peaks at higher depths into the wheel were lowered slightly. This may have some very nominal effect on asperity densities and slope calculations. Since circumferential profiles were used on a wheel that was true, extensive low-frequency smoothing was not necessary. This small amount of smoothing was chosen to filter out any voltage drift that can occur during the six minutes required for profile measurement. High frequency filters were not used because it would not have a significant effect on the density and slope calculations considering the spacing of the grits with the sampling interval used.
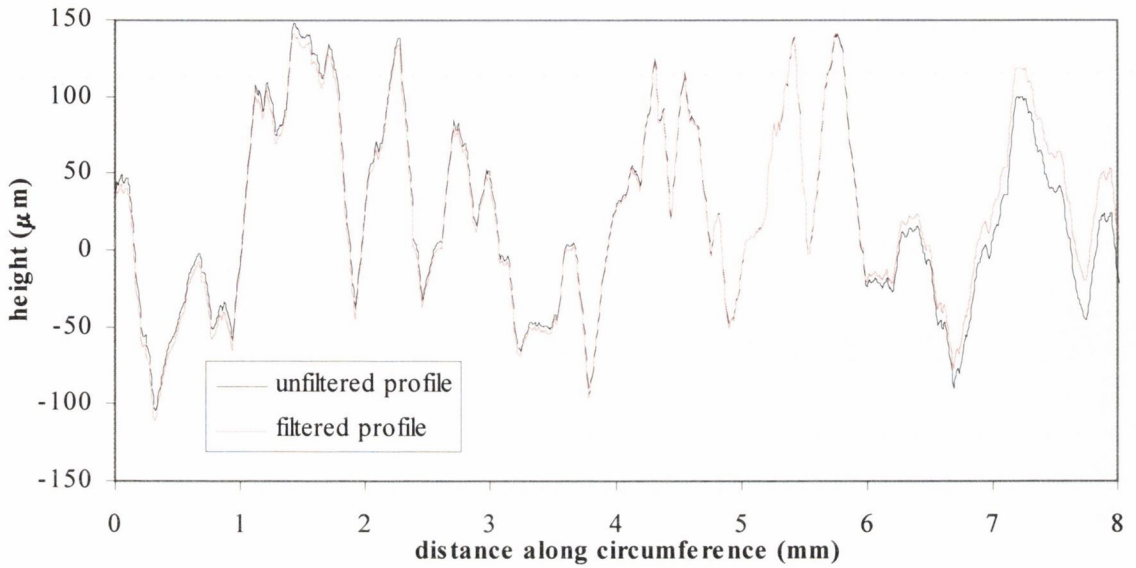
Figure 4.2. Effect of smoothing on VA wheel profile.

4.2.2. Sampling Interval.

The largest sampling interval that was used was 8 μm for the VA wheel in Set 1 and Set 2. By sampling at a given interval, say X mm long, all wavelengths shorter than a length of about 3X are ignored. Although filtering should not significantly affect the asperity density calculations, it could affect the slope distributions. To investigate this, a profile was taken with a 1 μm interval instead of the usual 8 μm interval and the profile was filtered according to Torrance [48] with a long wavelength cutoff of 4 mm and a short wavelength cutoff of either 1 μm or 20 μm. Typically, smaller sampling intervals lead to larger slopes [134]. The results of a differentiation according to these two values is shown in the power spectrum of Figure 4.3 below. It can be seen that at a value of 50 cycles/mm corresponding to a wavelength of 20 μm we see a drop in the power spectrum values. Also, the majority of slopes is in the longer wavelengths corresponding to values less than about 40 cycles/mm (40 cycles/mm corresponds to 0.025 mm which is greater than 20 μm). Therefore, a 8 μm sampling length corresponds to a scratch width of 24 μm (the product 3 and 8 μm=24 μm). The RMS slope for the 1 μm wavelength cutoff was 0.618 and the RMS slope for the 20 μm wavelength cutoff was 0.605. Therefore,

87

there was not a significant difference between the two and it was assumed that the filtering routine used was adequate. It is interesting to note that this value of slope (0.605) is almost exactly the value as found by Suzuki and Inasaki [127] who gave values ranging from 7° to 43° with an average of 30° (corresponding to a slope of 0.58).
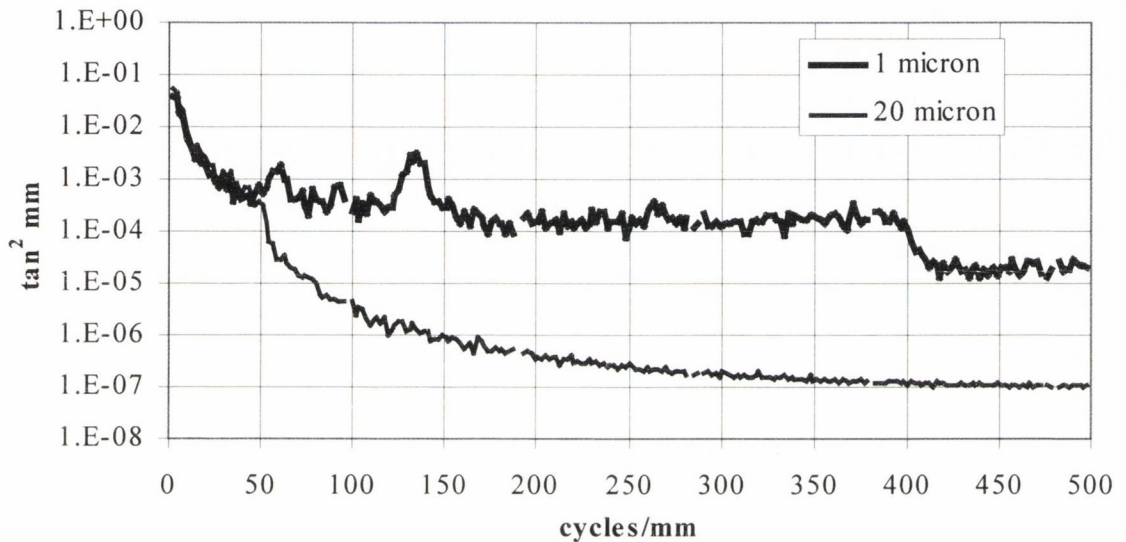
Figure 4.3. Effect of wavelength cutoff.

4.2.3. Calculation of Asperity Density from Profiles.

After smoothing, the next step was to calculate the asperity density. Figure 4.4 shows the top half of a smoothed circumferential profile taken of the dressed grinding wheel for a vitrified alumina (VA) wheel. If the peak asperity in the profile is found, the profile can be divided into several layers of equal distance beneath the peak asperity. For a given layer of depth beneath the peak asperity, the density of the cutting grits as a function of depth into the wheel, d_w, can be found by counting the number of asperity peaks protruding above each layer. A peak is considered an asperity if its height is greater than all values 64 μm to either side of it. This criterion allows for the fact that the highest point of one grit may be a distance of less than one grit radius from its neighbors and that a single grit may have multiple

cutting asperities. Further examination of this subject is given in the discussion. This will yield a linear density of peaks per unit length, n_d, measured in peaks/mm.
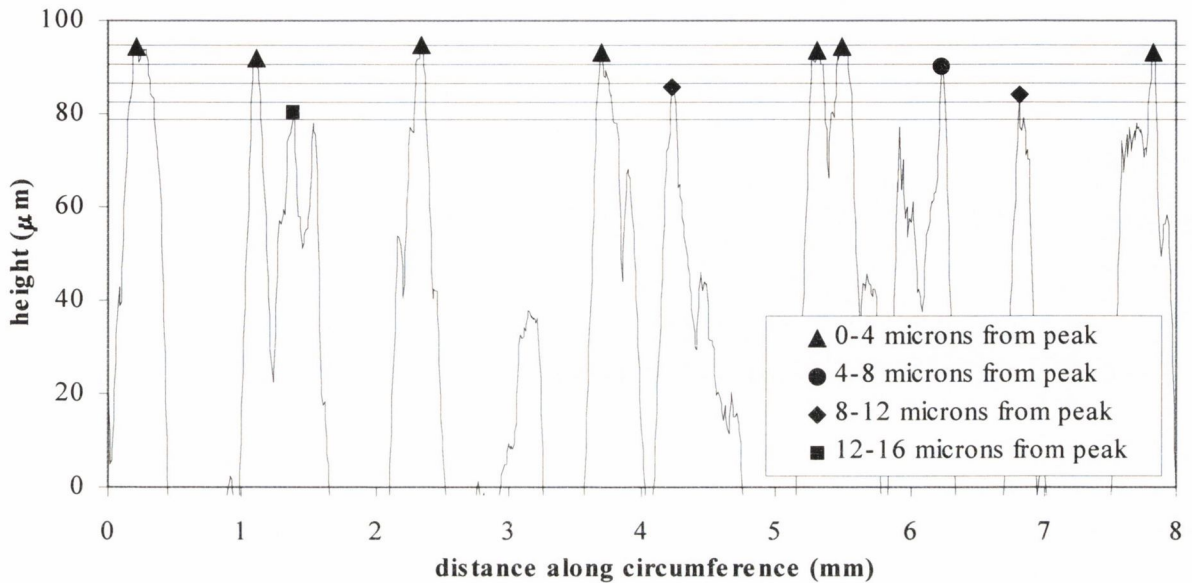
Figure 4.4. Asperity cutting point selection (VA wheel – fine dress).

If Nayak's [116] and Greenwood's [120] method of calculating areal density from linear density ($n \approx 1.2\ n_d^2$) is used (Section 1.8.4, page 54), then a plot of n versus d_w gives the results as shown in Figure 4.5 for the three dressing conditions. It can be seen that the areal density increases with increasing depth into the wheel as more cutting asperities are exposed. Also, a finer dressing produces a larger density. In addition, it appears that there is a linear relationship between n and d_w as was also found by Inasaki and co-workers [126, 127].
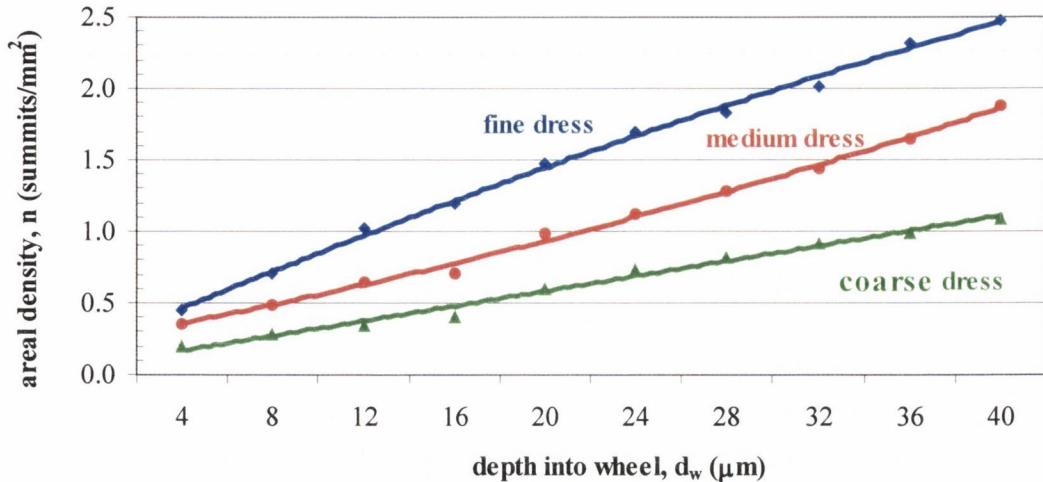
Figure 4.5. Areal cutting peak summit density – VA wheel, three dressings.

Profiles were taken after dressing and after grinding to see how asperity density changes with wear of the wheel. For softer grade wheels, there will be a greater extent of grit fracture and bond fracture that will expose fresh grits (Section 1.2.1, page 7). Harder wheels will tend develop attritious wear with blunting at the tips. This will change the density from a topography produced by dressing to a topography produced by wear from grinding. Figure 4.6 shows the three areal densities after dressing from above and the areal densities of the same three wheels after grinding.
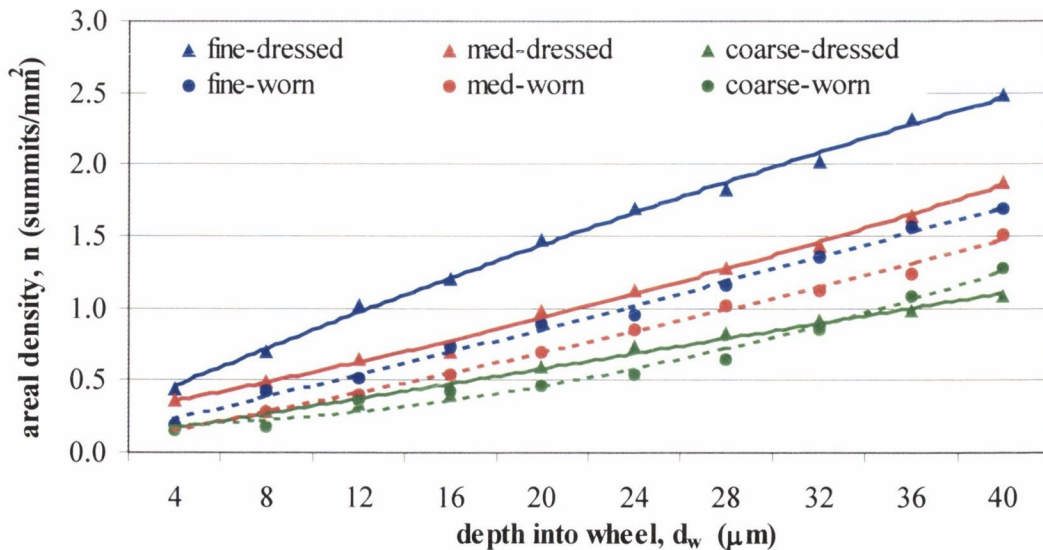
Figure 4.6. Asperity density – VA wheel, three dressings, dressed and worn.

If we compare the densities from the dressed and the worn profile for the fine dress, we can see that the density decreases considerably. This indicates that the topography generated from self-sharpening of the wheel – a self-imposed "natural topography" – has a density significantly lower than that produced by dressing. This is particularly true at small values of d_w at the grain tips. For the medium dress there was a similar change but not as pronounced. For the coarse dress the density stayed largely the same although took on a more non-linear nature. It could be concluded that there may be a "natural" areal density of the wheel that will be produced with wheel wear and that this will be approached after wear regardless of the initial dressing conditions used. This was also found by Rowe [33] and will be discussed later.

As stated by Verkerk [128], the method of defining a cutting asperity, the method of measurement used, the criterion employed for defining a peak and the method for calculating peaks/mm^2 from peaks/mm can all yield very large variations in values of density as shown in Section 1.8.4 (page 54). The values measured here fall into the range measured by previous researchers.

To further corroborate the method used here, we can consider the natural density of the grits in the wheel and determine how the calculated densities from profilometry relate to the natural density at large depths into the wheel where dressing has less effect.

At one-half the mean grit diameter into the wheel, we should see a measured areal density approximately equal to the theoretical density of the wheel. Since the volume of grits is much larger than the volume of bond for this grade of a vitrified bonded wheel [134], the theoretical spacing between grits can be approximated by

$$d_{grit} = 1.41\ D_{g,mean} \tag{73}$$

where d_{grit} =is the spacing between grits and $D_{g,mean}$ is the mean grit diameter. This same value was also found by Pandit and Sathyanarayanan [36] (Section 1.2.2, page 8) in their measurement of wavelengths. For the grit size used, $D_{g,mean}=15.2/60=253$ μm according to Malkin [13]. This gives a value of d_{grit} = 354 μm. If we assume a

91

linear relationship between n and d_w, we can extrapolate the fine profile of the worn wheel which seems to best approach the natural grit density and the value on the curve to which the others appeared to converge. Doing so yields a distance between grits of n=5.5 grits/mm^2 at a depth of $d_w = D_{g,mean}/2$=127 μm. Working backwards to get the linear density from the areal density according to $n \approx 1.2\ n_d^2$ gives a value for the linear density of n_d=2.14 grits/mm. This corresponds to a mean spacing of

$$d_{grit} = 468\ \mu m$$

which is reasonably close to the theoretical spacing of

$$d_{grit} = 354\ \mu m.$$

The discrepancy could be explained by a non-linear relationship at higher depths which appeared to be the case from the worn profiles. Using a non-linear fit would give a value even closer to the theoretical value. The difference could also be due to the assumptions made in the calculation of the distance between grits from the mean grit spacing.

Consequently, this indicates that the method of calculating grit areal density from surface profiles appears sound, particularly in light of the large variation in measurements of other researchers (page 56).

4.2.4. Calculation of Asperity Slopes from Profiles.

The second parameter analyzed from the wheel profile was the distribution of the slopes of the asperities. According to Malkin [27], increasing the dressing in-feed and dressing lead yields larger dressing particles because of a greater probability of bond fracture as opposed to grain fracture or attritious wear at the tips. Grit and bond fracture during dressing and, in particular, attritious wear during grinding produce smaller slopes at the tips of the grits where grinding occurs. Figure 4.7 shows the relationship between the average grit slope measured from the wheel profile and the

depth into the wheel for the three dressings of the VA wheel. It is clear that coarser dressing conditions produce larger asperity slopes at the grain tips and, hence, a sharper wheel. As d_w increases, all values converge to a slope of approximately 0.58 (30°). Other researchers who have measured slopes of abrasives but did not take into account changes with depth into the wheel found similar values [127].
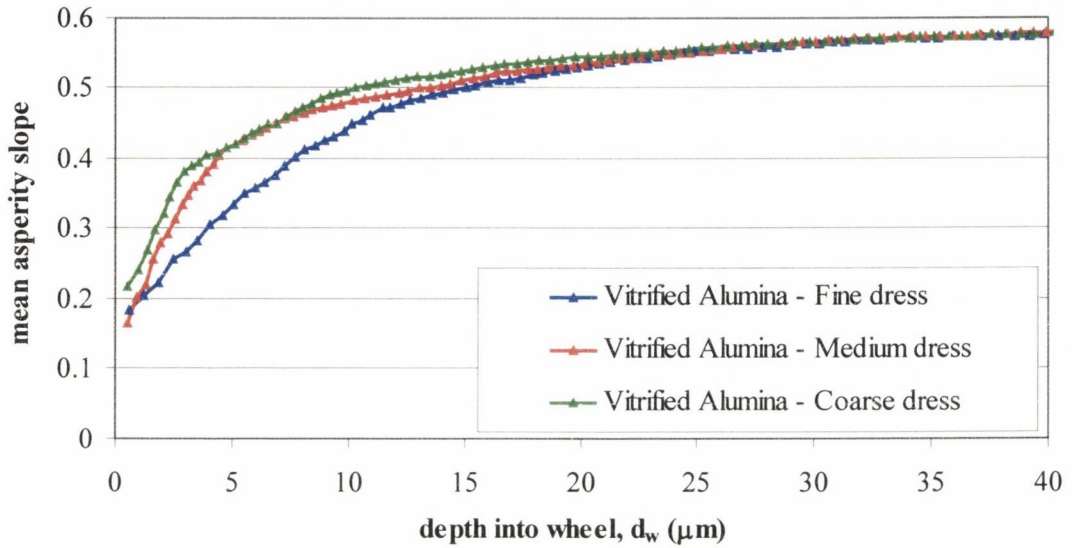
Figure 4.7. Asperity slope for three dressing conditions.
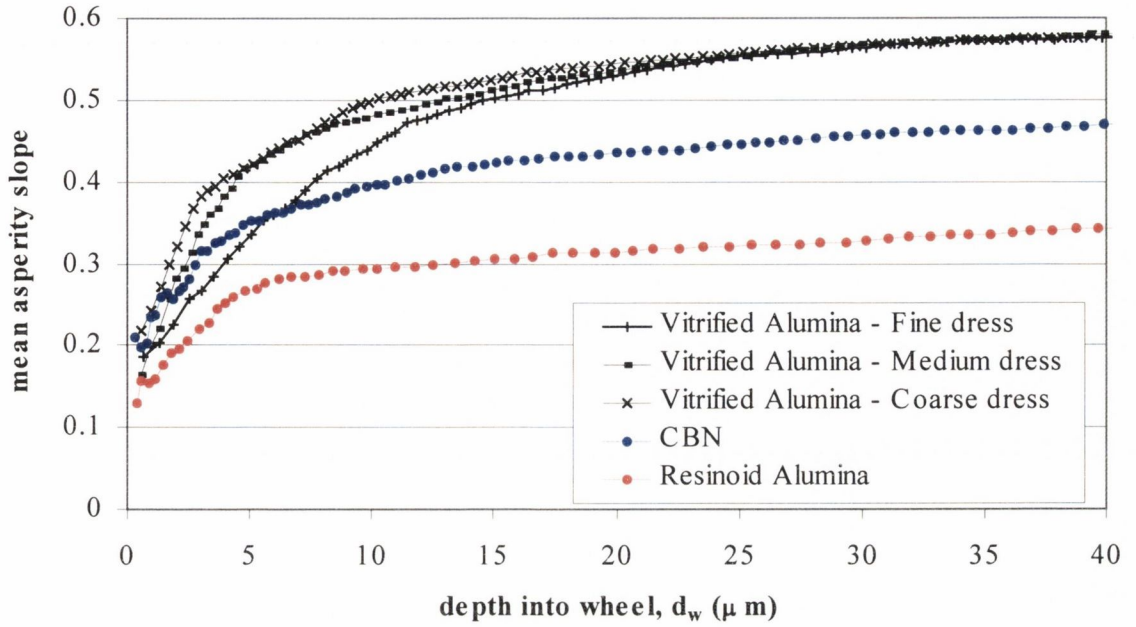
Figure 4.8. Slope versus depth into wheel for three wheel types.

Figure 4.8 above shows how slope varies for the different wheels used. The RA wheel and the CBN wheel used here have smaller mean grit diameters than the VA wheel. This smaller final value for slope is most likely due to the higher grit density inhibiting the stylus from penetrating as far into the wheel as shown in Figure 4.9 below and the lower porosity present in these bonds types. Nevertheless, at lower values of d_w where grinding occurs, the slopes were in a similar range regardless of the wheel type or grit size.
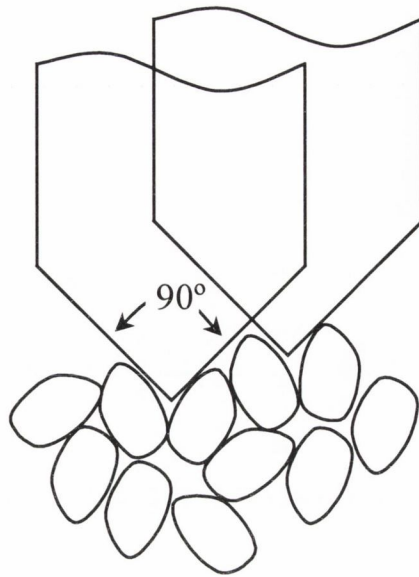
Figure 4.9. Stylus and grits – lack of full penetration at larger depths.

Malkin [17,27] discussed how percent wear flat area increased with metal removal. The attritious wear which is important in terms of forces and temperatures occurs at the grain tips. Therefore, this should also be evident in comparing the slopes of the dressed and the worn wheel. This can be seen in Figure 4.10. Here we can see that at the wear tips in the first 0-10 µm, the slope drops significantly with wear of the wheel. As d_w increases, the two curves quickly meet up converging at about 7 µm. This is because of the attritious wear occurring at the grit tips. A similar trend was seen in the other dressing conditions although not as pronounced as in the coarse dress. This indicates that, as was seen with the density calculations, self-sharpening was more prevalent. This is the reason why profiles were taken after dressing and after grinding. Since during grinding the wheel topography changes throughout, both profiles were needed to predict the changes in forces with wheel wear.
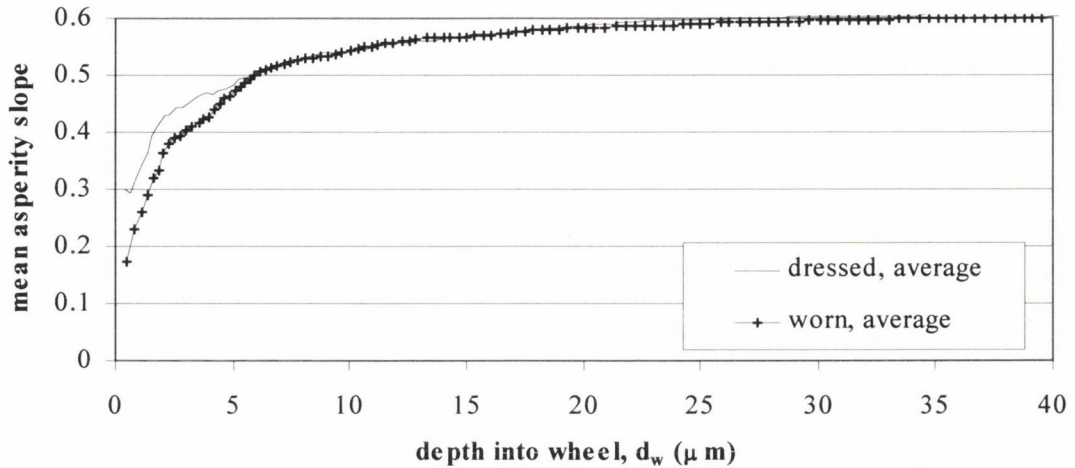
Figure 4.10. Change in slope distribution with wear of wheel – coarse dress.

4.3. Hardness Measurement.

The 2-D model of grinding uses the bulk hardness of the workpiece and the 3-D model used the bulk hardness of the material and surface hardness of the material after grinding. Therefore, bulk hardness tests were taken and surface hardness tests were taken after grinding to determine the extent of work hardening of the surface layer. Results are given in Table 4.3 showing the average values measured. Surface hardness measurements were not taken on the case-hardened EN39B specimens as hardness values will vary throughout the case and reliable results would not be obtainable. In the model, estimates were made on the extent of strain-hardening from the EN31 tests since the case-hardened surface of EN39B should have similar hardenability properties. For the EN31 and the M2 workpieces, numerous measurements were taken with a load of 50g and with a load of 200g and a mean value was calculated for each. Because of the depth of penetration into the non-strain-hardened layer, a load of 50g is expected to give larger values than a load of 200g and a more accurate value for the true surface hardness. However, small loads can also mean a greater likelihood of experimental error even on a well-polished surface. This was evident in the difference observed in the standard deviation of the 50g load measurements and the 200g measurements. The standard deviation of the 50g measurement was larger and, given the experimental scatter, it is uncertain to

what extent this difference is due to the smaller load or simply due to experimental scatter. Therefore, values from the 200g measurements were used.

Table 4.3. Hardness values.

	EN31	EN39B	M2
Bulk Hardness H_b HV	736	633	860
Surface Hardness H_s (50g) HV	870		1116
Ratio H_s/H_b (50g)	1.18		1.30
Surface Hardness H_s (200g) HV	816		1027
Ratio H_s/H_b (200g)	1.11		1.19

4.4. Force Models Applied to Grinding Results.

Using the measured wheel profiles, the workpiece and wheel properties and the grinding parameters, the 2-D Challen and Oxley model and the 3-D Xie and Williams model were both used to predict forces for each grinding condition. The procedure was as follows.

- Dressed and worn wheel profiles were filtered and calculations made for
    - asperity areal density distribution – n versus d_w.
    - asperity slope distribution – slope versus d_w.
- Bulk hardness values (used in the 2-D and 3-D models) and surface hardness values (used in the 3-D model) were taken for the workpiece.
- Force predictions were made for F'_n and F'_t versus h_{eq} for both the 2-D and the 3-D model. Experimental forces were plotted with them.

The theoretical results from the program and the measured experimental results from the grinding tests were then compared. For the 3-D model, one set of force predictions was made using an average of several dressed profiles and one set of force predictions was made using an average of several worn profiles. To some extent, this takes into account the change in wheel topography. For the 2-D model, one set of predictions was made for the dressed wheel.

4.4.1. Set 1: EN31 with Vitrified Alumina wheel – three dressings.

The theoretical forces from the 2-D model, the theoretical forces from the 3-D model and the measured experimental forces from the grinding of EN31 after fine dressing (s_d=200 µm, a_d=5 µm) are shown in Figure 4.11. The top graph is given in log-log scale and the bottom graph is given on a linear scale. The experimental points are plotted. The 2-D predicted values are shown by a bold line. The 3-D predicted values are shown by a solid line for the dressed profile and a dashed line for the worn profile.

The correlation between the predicted and the measured forces for the 2-D model is mediocre. The normal forces are over-predicted throughout and the tangential forces are over-predicted at low h_{eq} and under-predicted at high h_{eq}. For the 3-D model, the predictions are excellent throughout – predominantly falling within the range between the dressed and worn profile predictions. There is a difference between the predicted forces for the dressed and the worn profiles which was evident in the density and slope distributions as the finely dressed wheel did significantly change during wheel wear – a change that was not as pronounced in the medium and the coarsely dressed wheel.

As seen earlier, the more aggressive dress yielded lower asperity densities (Figure 4.5, page 90) and larger asperity slopes (Figure 4.7, page 93). The results from grinding after medium dressing (s_d=200 µm, a_d=30 µm) are shown in Figure 4.12. Here we see a drop in forces from the fine dress and again a more accurate prediction from the 3-D model. The results of grinding EN31 after a coarse dressing (s_d=200 µm, a_d=60 µm) are similar to those of the medium dress and are shown in Figure 4.13. As expected, the difference between the predicted values for the dressed and worn wheels is not as large.

4.4.2. Set 2: EN39B with Vitrified Alumina Wheel – Three Dressings.

The results from grinding of EN39B with a VA wheel are shown in Figure 4.14, Figure 4.15 and Figure 4.16 for the fine, medium and coarse dressings, respectively.

As stated earlier, accurate hardness values were more difficult to obtain because of the depth of the case. In addition, because the EN39B workpieces had some degree of curvature in the as-received condition, a significant amount of material had to be ground away before the workpiece was level and measurements could be taken. This meant that grinding forces were measured at a depth into the case where hardness values had dropped. Therefore, for a given set of experimental grinding forces, measurements were taken on material of varying hardness. Nevertheless, the predicted values for the fine dress, particularly for the 3-D model, are very good and largely fall into the range of dressed and worn predictions.

4.4.3. Set 3: M2 with Resinoid Alumina Wheel – Two Dressings.

The results from creep-feed grinding of M2 with a resinoid alumina wheel are shown in Figure 4.17. Grinding tests where done for two different dressing conditions. However, because creep-feed grinding with a RA wheel caused burning of the resin and pull-out of the grits, the constant self-sharpening of the wheel during grinding meant that changing the dressing conditions did not noticeably affect grinding forces nor did it affect asperity densities and slopes from the measured wheel profile. Profiles were taken after each set of tests but asperity densities and slopes were found to be much the same indicating that the original dressed wheel topography was quickly replaced by a "natural topography" resulting from self-sharpening of the wheel due to bond and grain fracture and burning of the resin. Therefore, one set of force predictions was made from the worn wheel profiles and the results from both tests are plotted together.

4.5. Set 4: EN31, EN39B and M2 with CBN Wheel – One Dressing.

The results of grinding the EN31, the case-hardened EN39B and the M2 with the vitrified CBN wheel and neat oil are shown in and Figure 4.18, Figure 4.19 and Figure 4.20. Because CBN wheels are harder and do not show near as much wheel wear with metal removal and exhibit very large G-ratios [13], the difference

between profiles taken after dressing and after grinding was found to be insignificant and profiles taken after grinding were used.
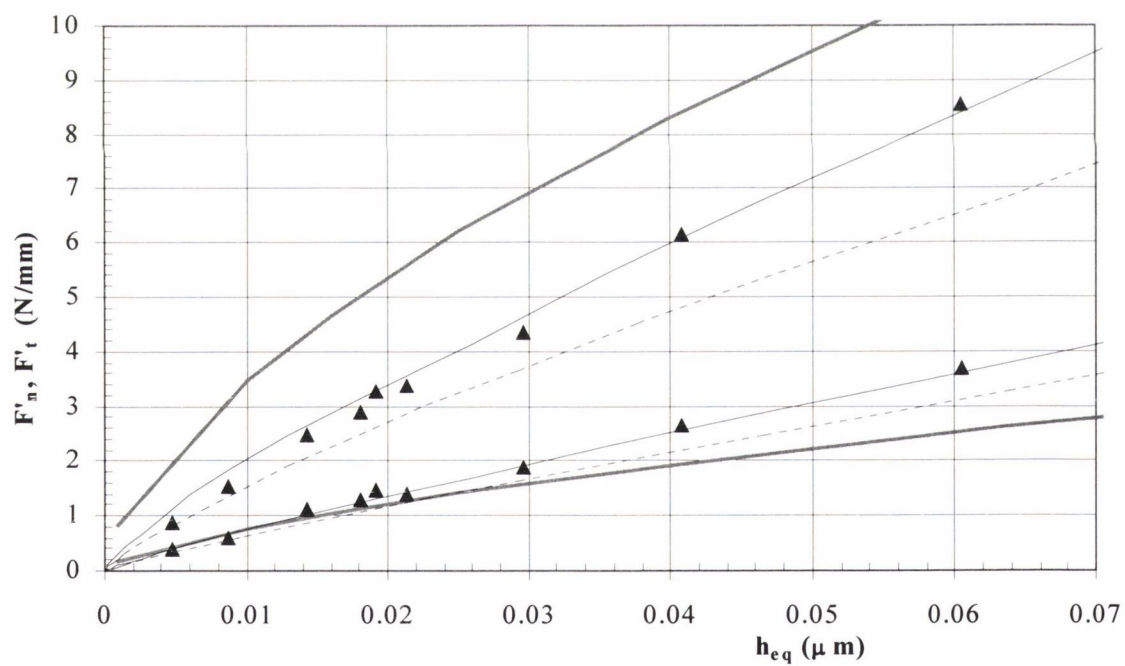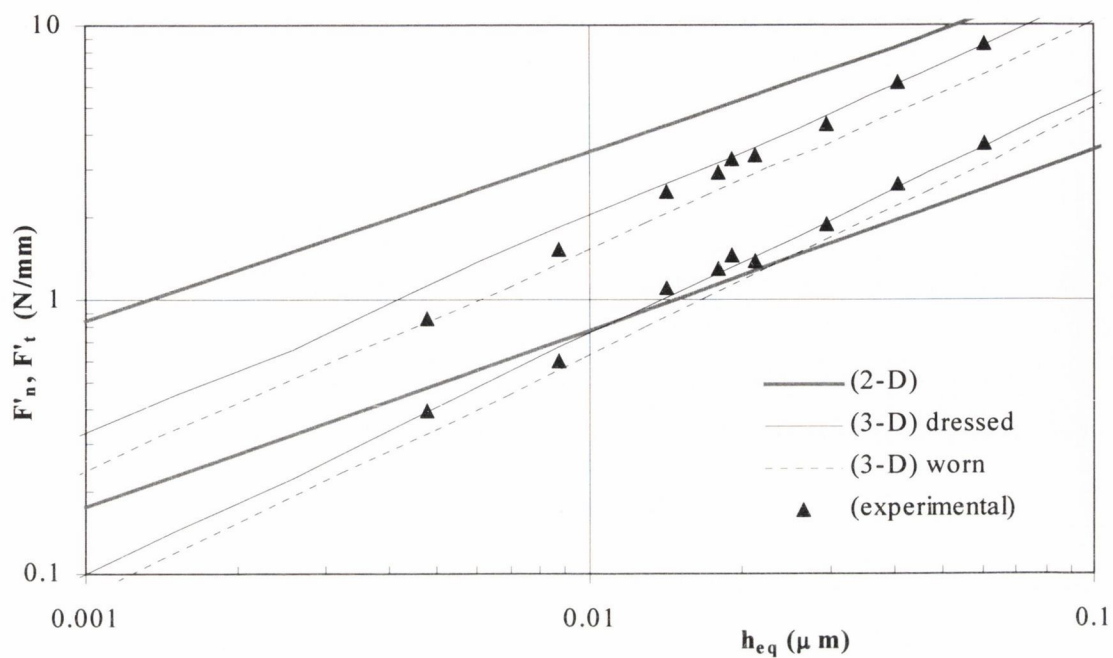
Figure 4.11. Predicted and measured forces for EN31 – Fine dress.
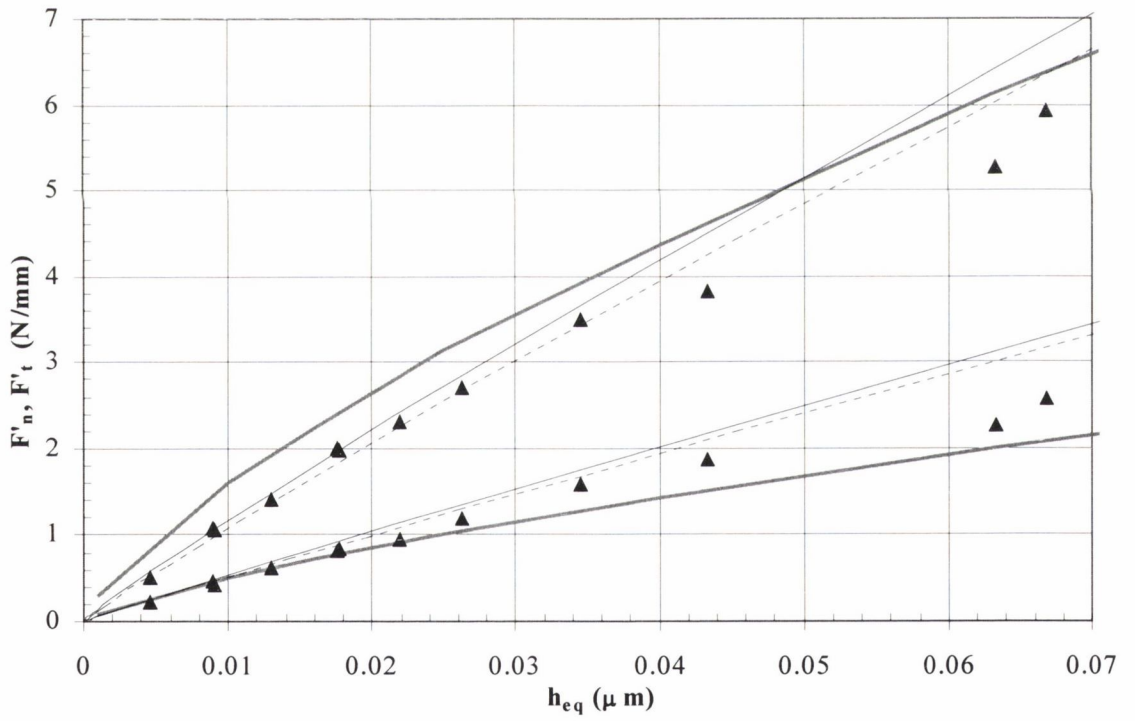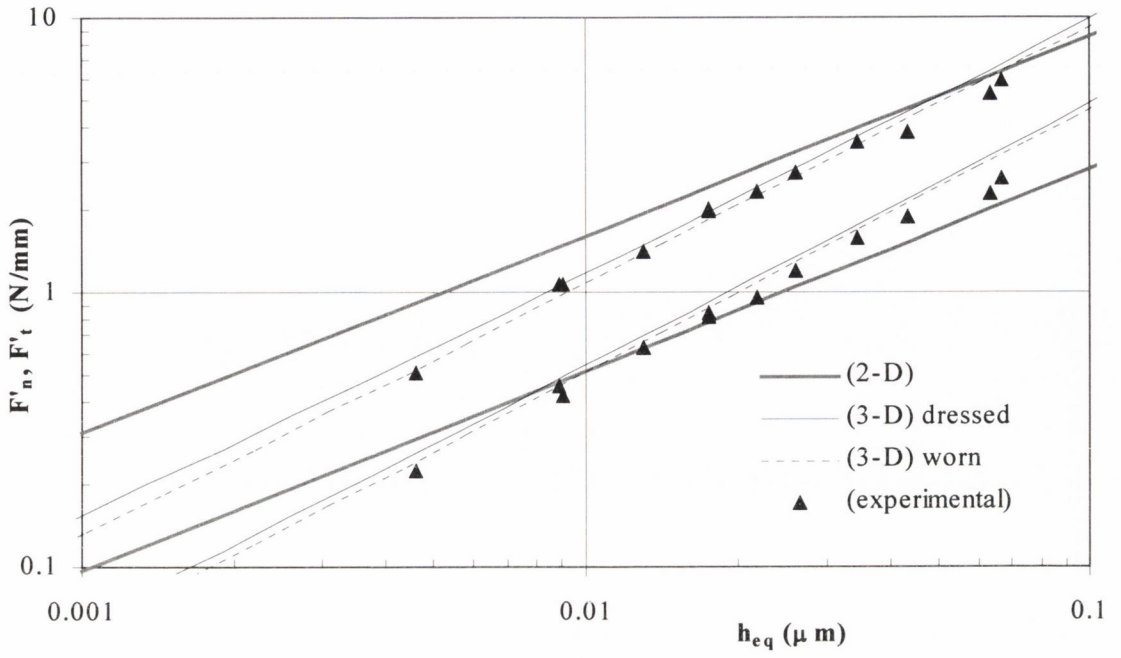
Figure 4.12. Predicted and measured forces for EN31 – Medium dress.
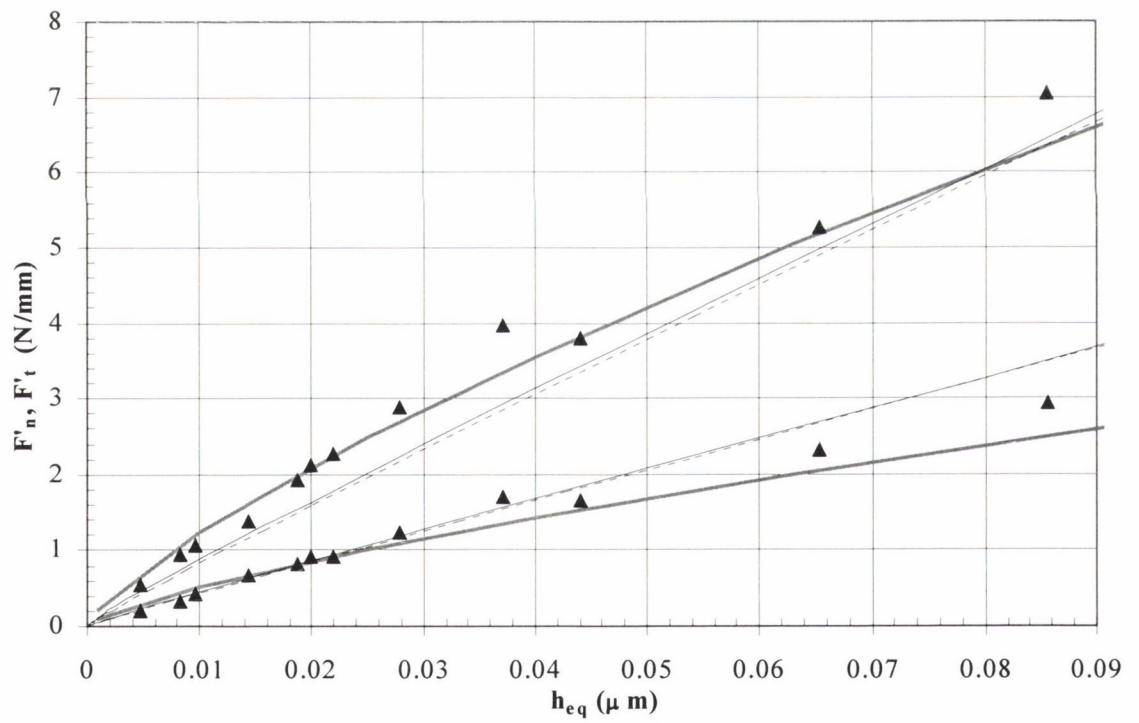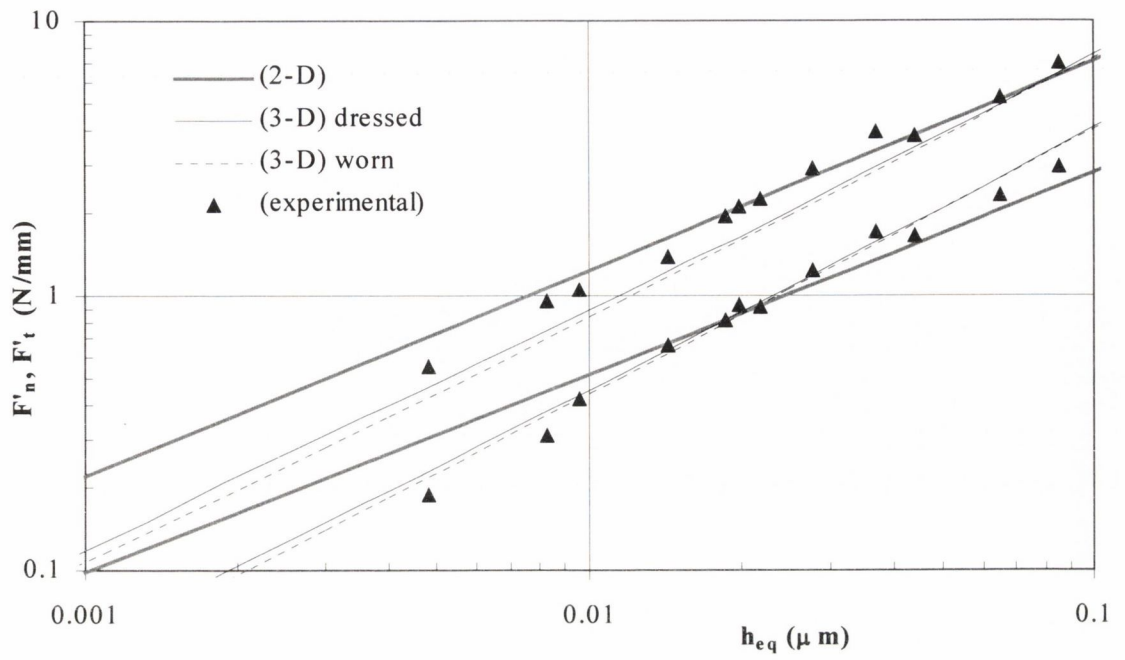
Figure 4.13. Predicted and measured forces for EN31 – Coarse dress.
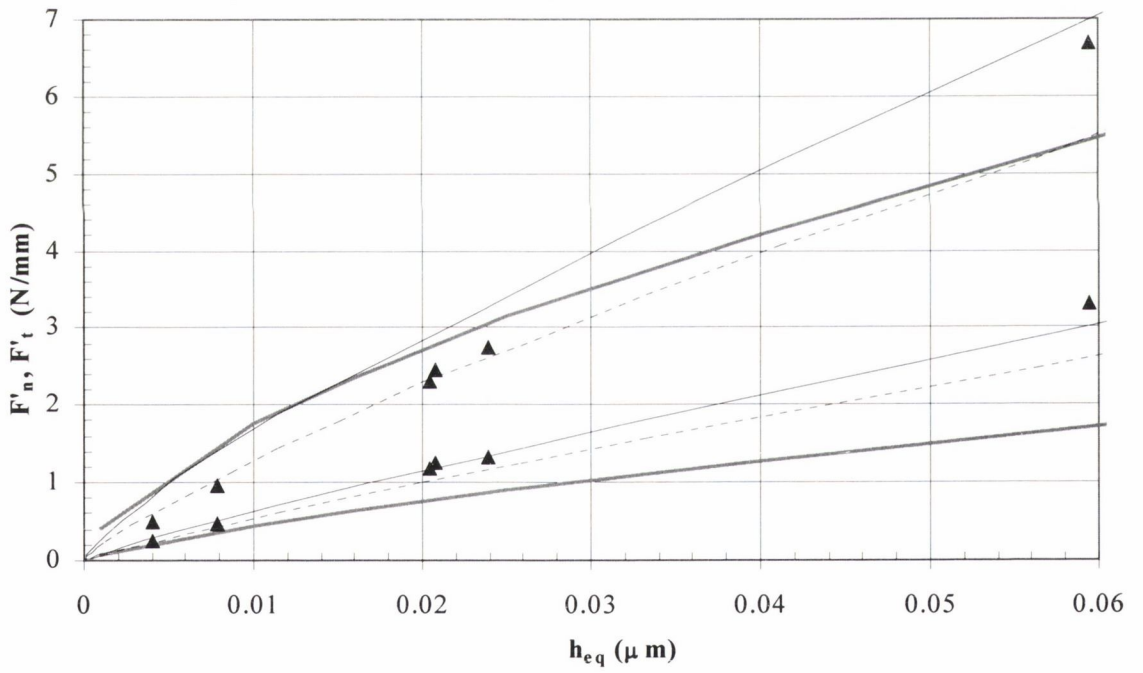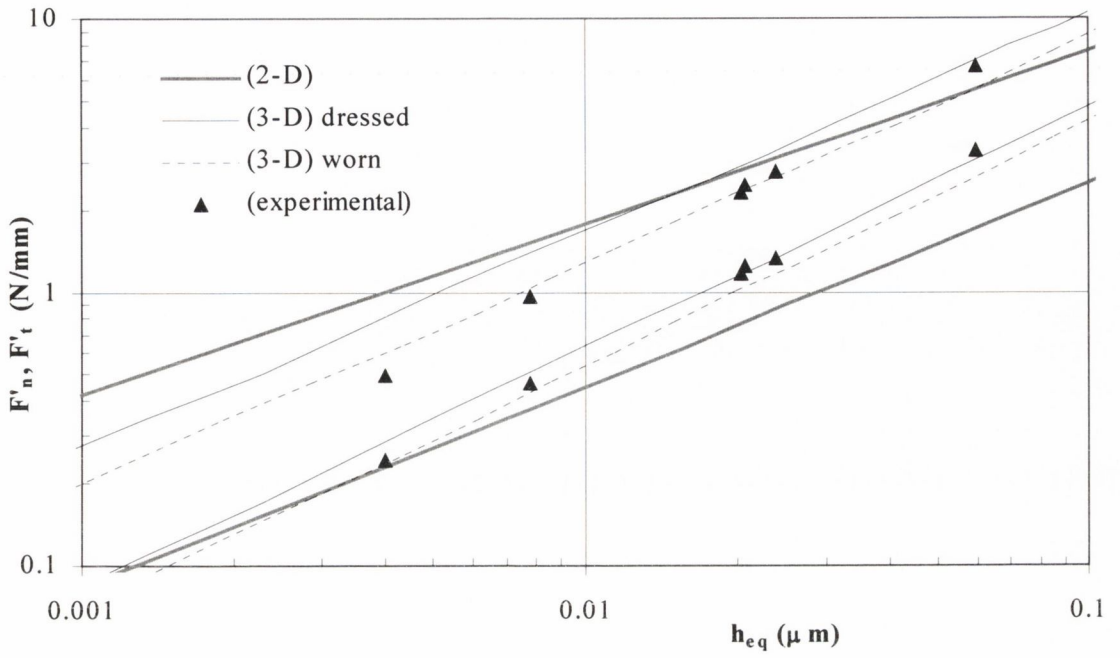
Figure 4.14. Predicted and measured forces for EN39B – Fine dress.
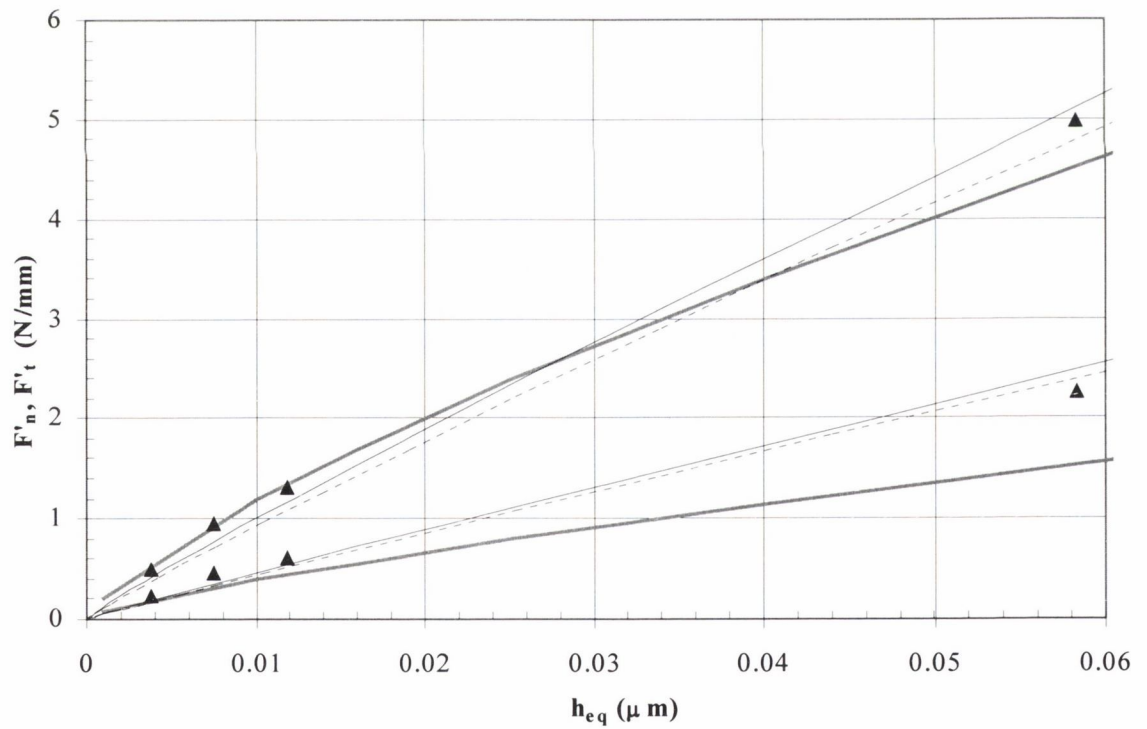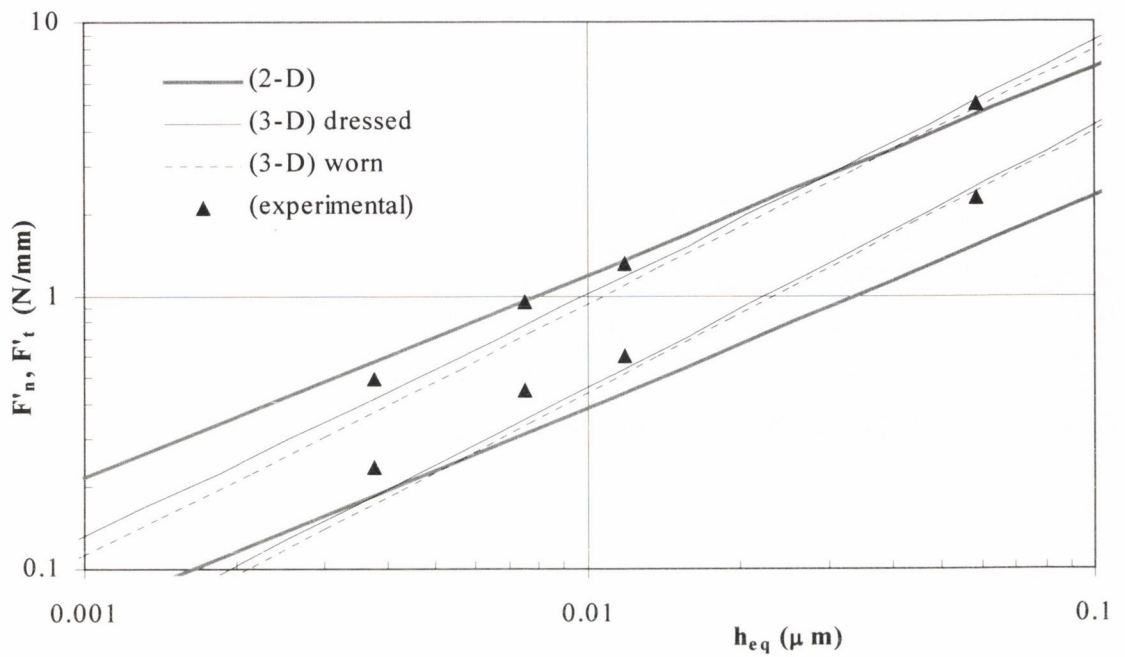
Figure 4.15. Predicted and measured forces for EN39B – Medium dress.
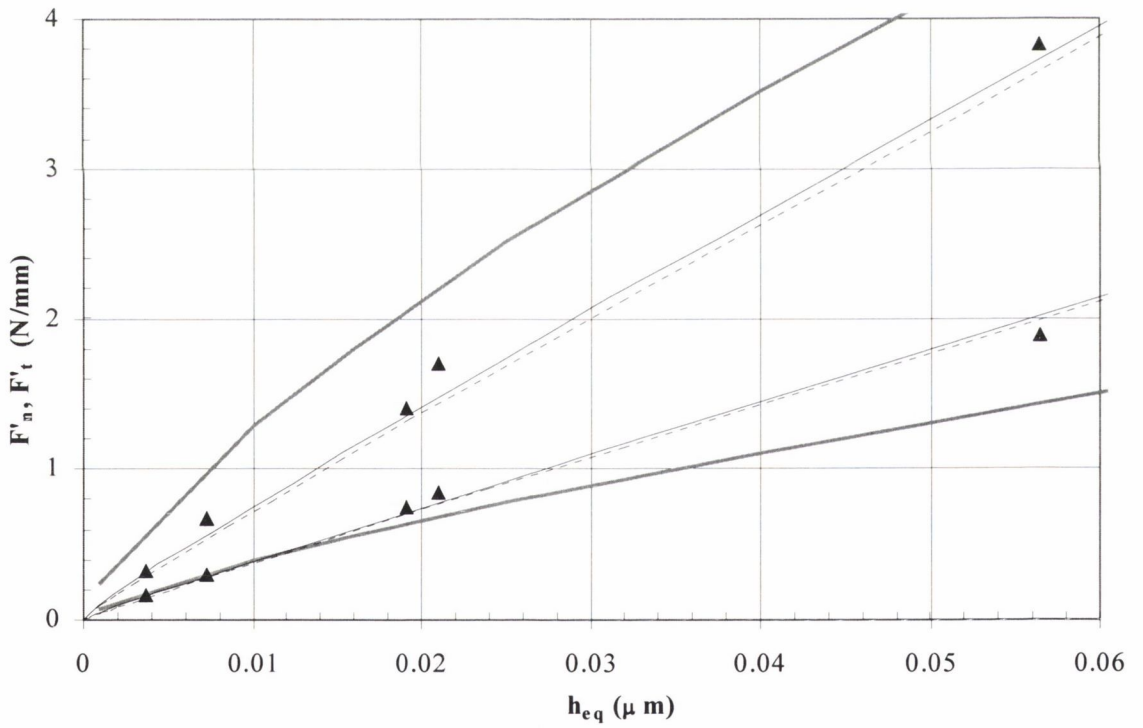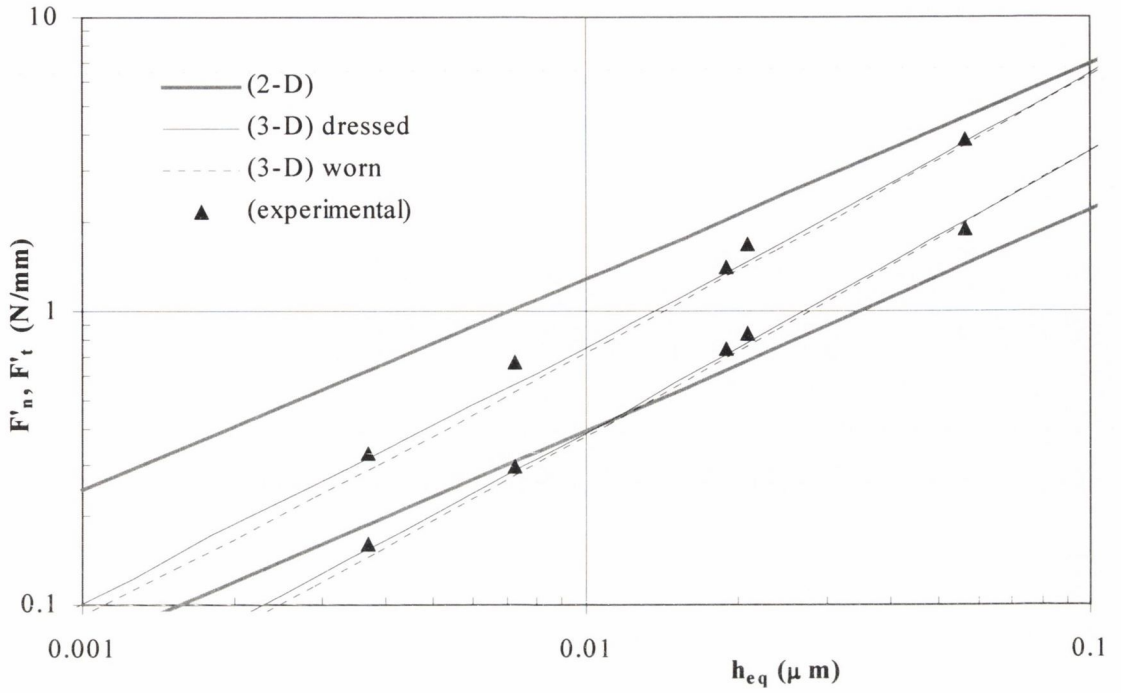
Figure 4.16. Predicted and measured forces for EN39B – Coarse dress.
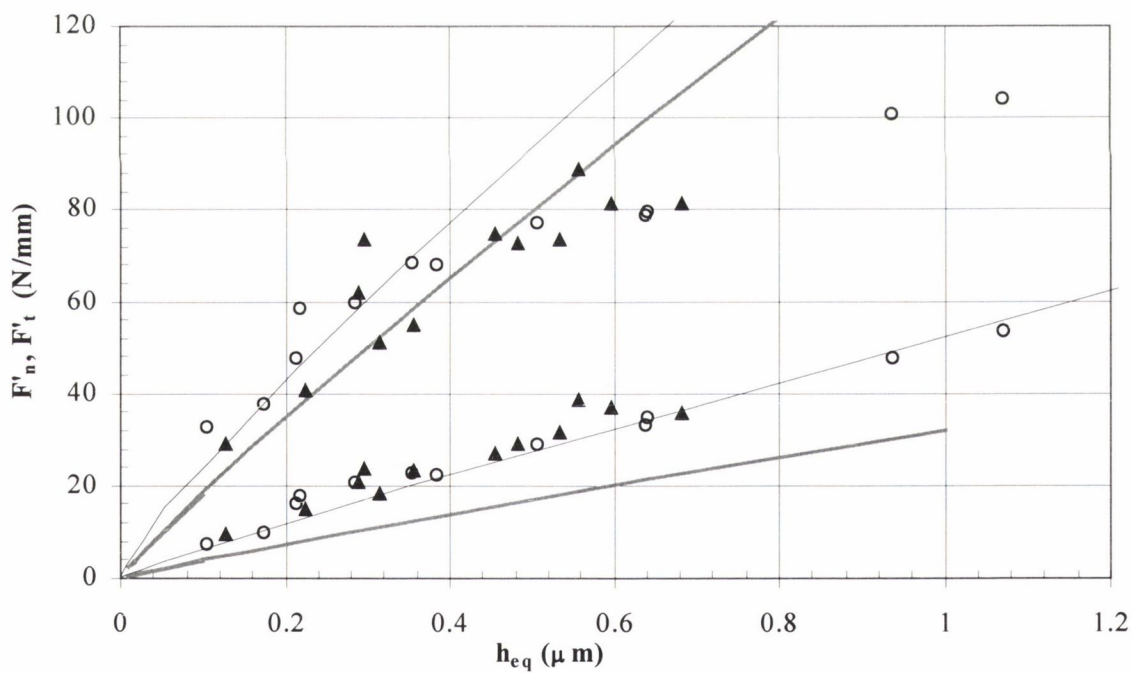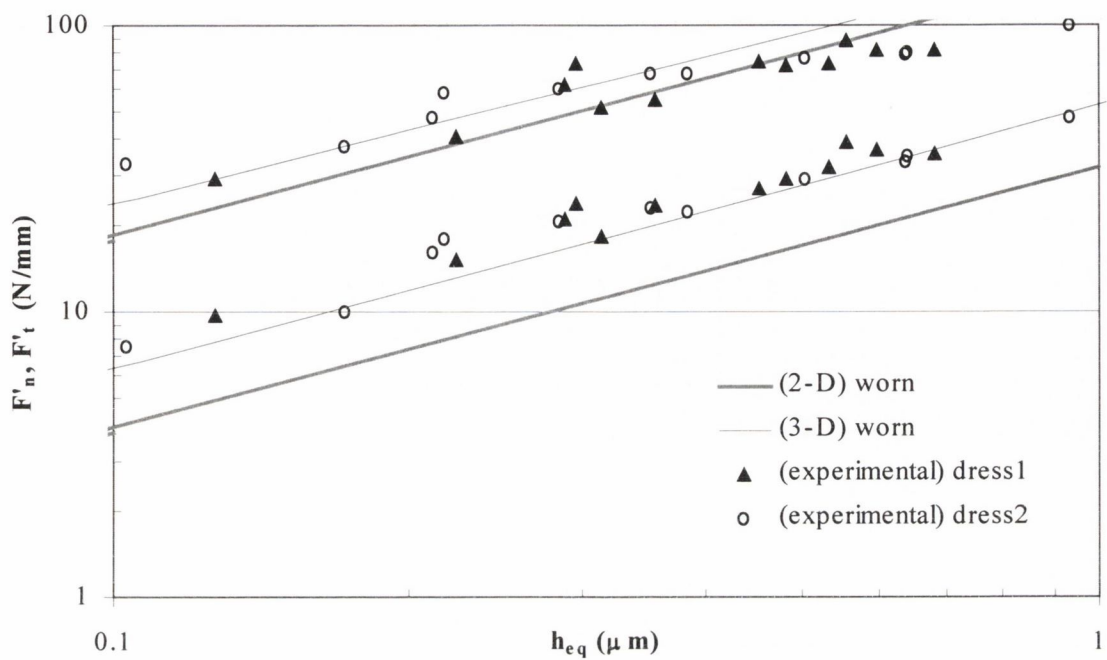
Figure 4.17. Predicted and measured forces for M2 – dressing 1 and 2.
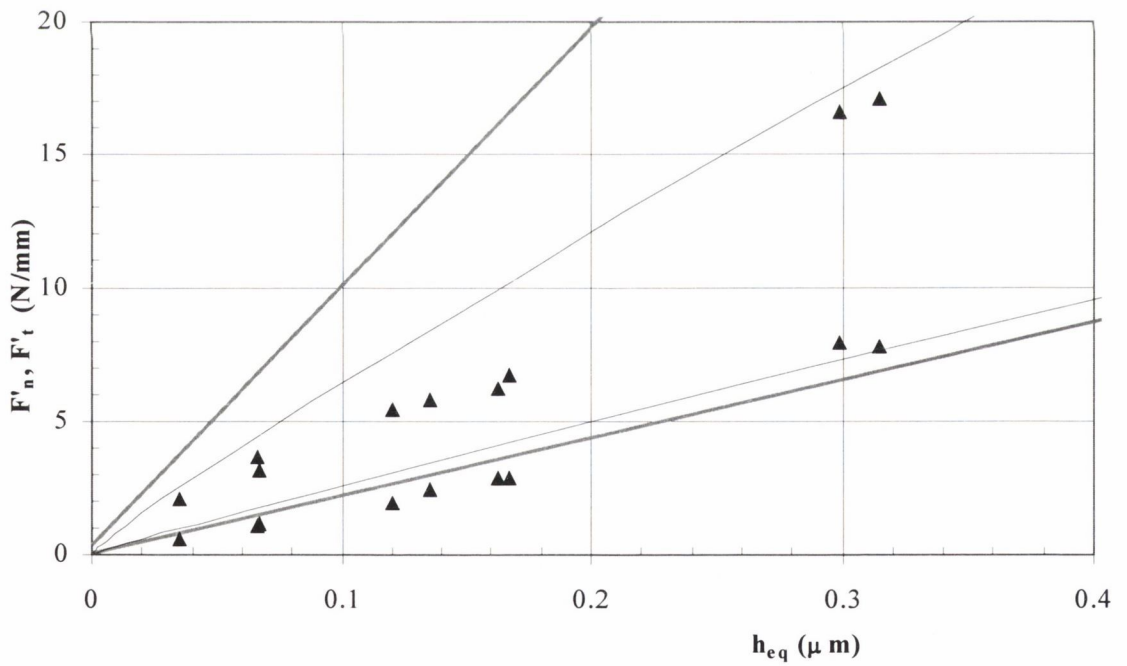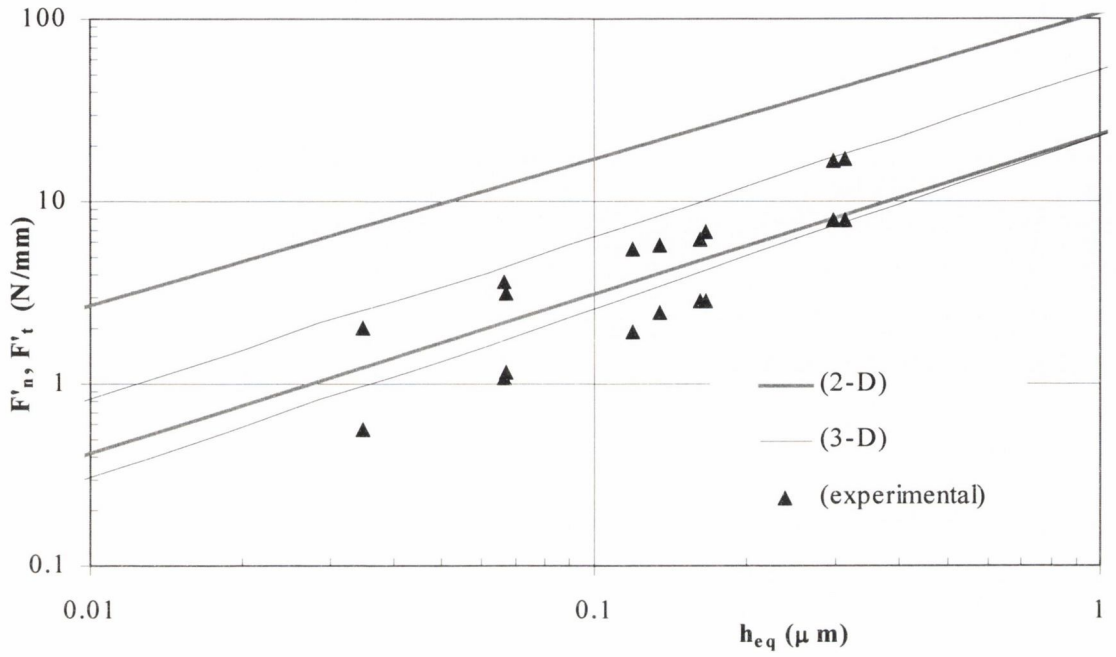
Figure 4.18. Predicted and measured forces for EN31 with CBN wheel.
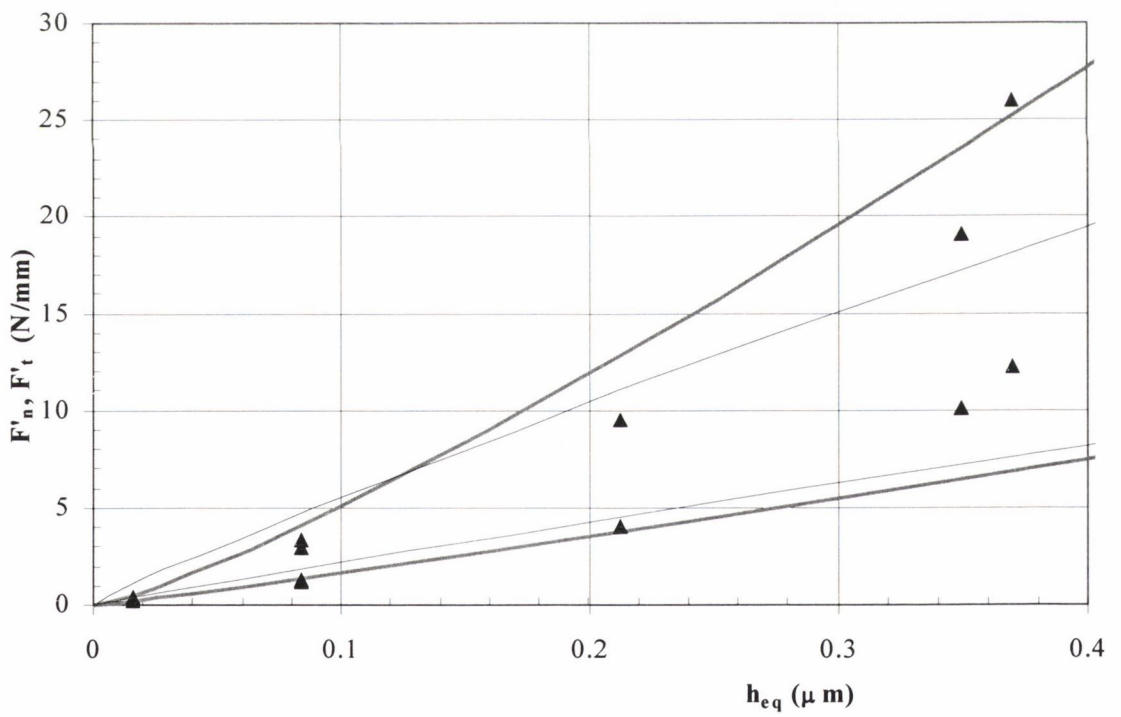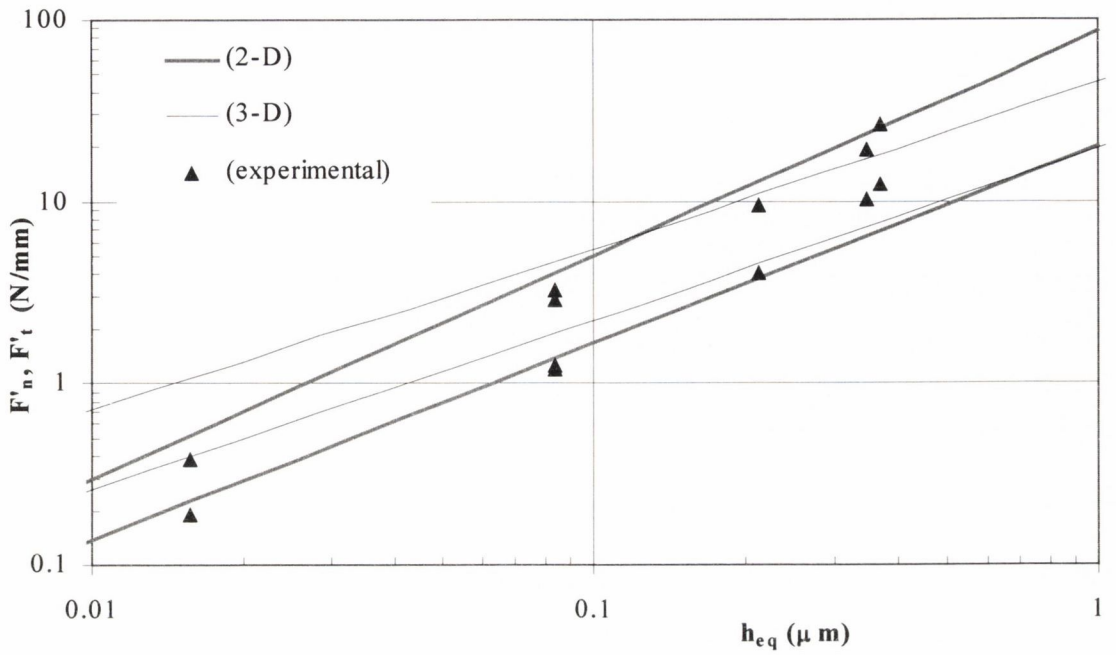
Figure 4.19. Predicted and measured forces for EN39B with CBN wheel.
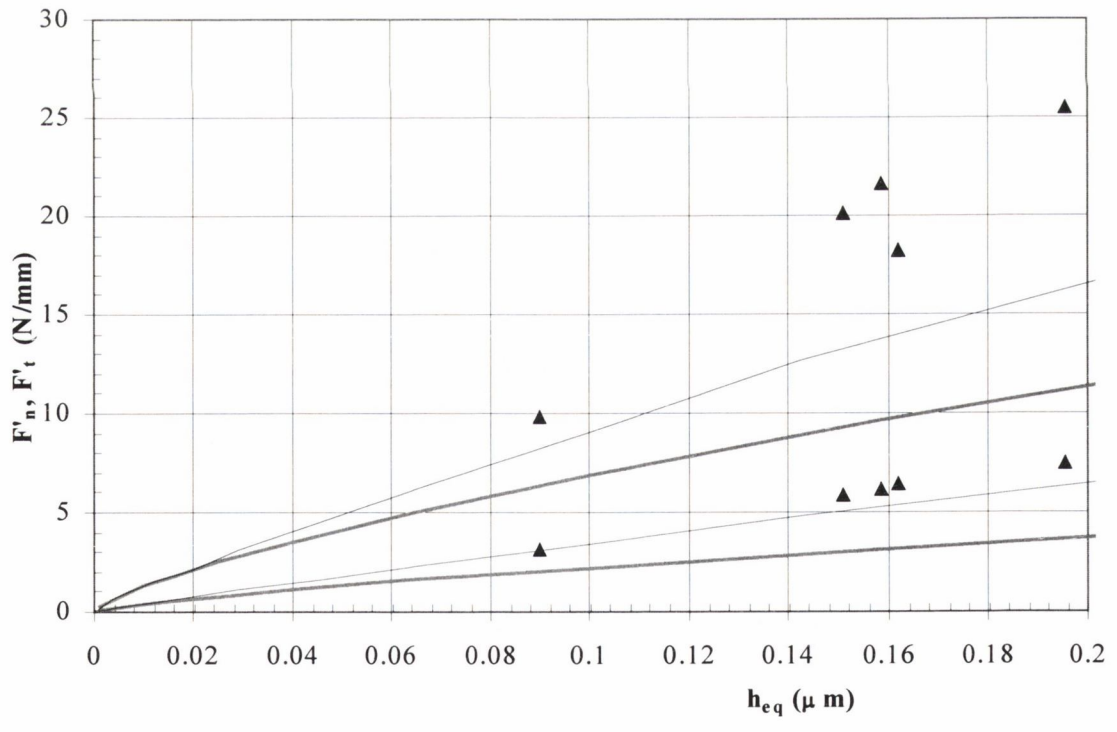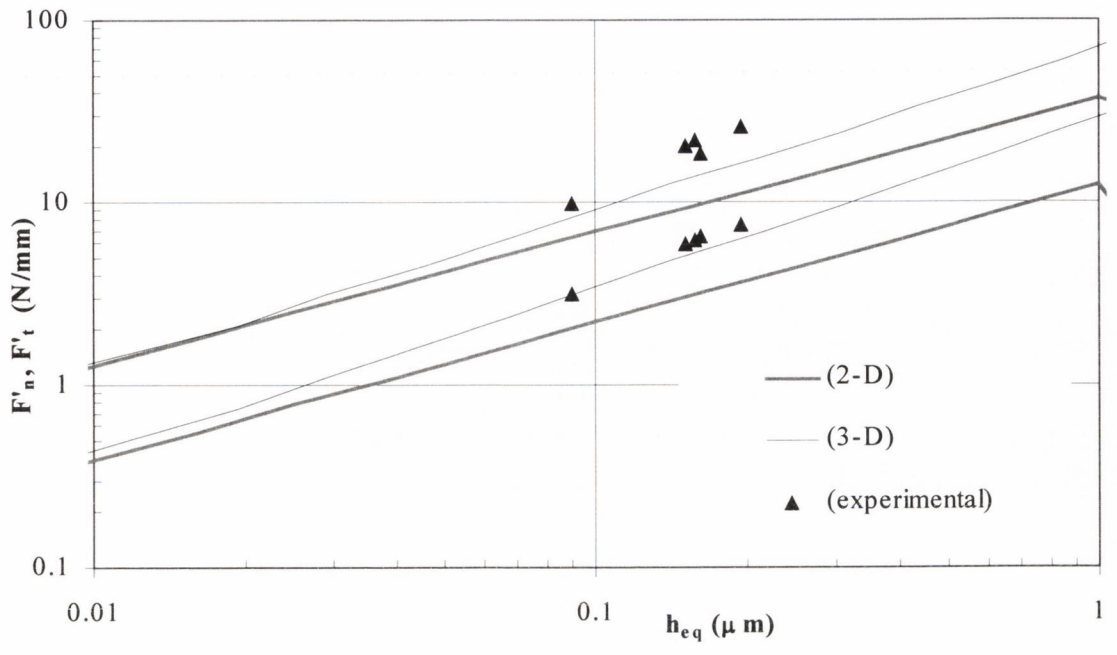
Figure 4.20. Predicted and measured forces for M2 with CBN wheel.

CHAPTER 5. DISCUSSION.

The results show that the grinding models proposed here are adequate in predicting the forces in a surface grinding operation on hard, low-alloy steel. The results obtained from the three-dimensional model based on Xie and Williams were much more accurate than those obtained from the two-dimensional model based on Challen and Oxley.

5.1. Predicted and Measured Values – 2-D and 3-D Model.

5.1.1. Set 1: EN31 with VA Wheel.

The correlation between predicted and experimental forces shown in Figure 4.11 (page 101, fine dress, $a_d = 5$ μm) was adequate for the 2-D model and excellent for the 3-D model. For the 3-D model, the experimental results fell into the predicted range between the dressed and worn wheel throughout. The 2-D model exhibited a slope that was not consistent with the experimental results. Because the dressed and worn profiles exhibited different asperity densities and slopes with wheel wear, predictions were made from both the dressed and worn profiles for the 3-D model. Predicted forces were lower for the worn wheel. As seen in Section 4.2 (page 86), asperity densities dropped with wheel wear – which would cause forces to drop – and asperity slopes dropped with wheel wear – which would cause forces to rise. From the drop in predicted forces with wheel wear, it is evident that the drop in asperity density had more effect on the predicted forces than the drop in asperity slope. A given set of grinding tests was made with increasing values of speed and in-feed throughout – i.e. tests at small value of h_{eq} were done before tests with large values of h_{eq}. Therefore, the experimental points which lie to the left of the graph were made with a wheel whose topography was created from dressing and those to the right with a wheel whose topography was created from wear and self-sharpening. Evidence of self-sharpening is also seen for the medium and coarse dress with the drop in experimental forces at higher values of h_{eq} where forces on the grits are largest and self-sharpening most likely. Therefore, the model is most

reliable if the wheel does not change significantly during grinding – neither attritious wear at the grit tips or grit/bond fracture.

Overall, for the fine dress, the slope and the predicted values from the 3-D model were in very good agreement with the measured values and much better than the results of the 2-D model.

The measured forces for the medium dress (Figure 4.12, page 102, $a_d = 30$ μm) were lower than those of the fine dress. This is expected as the more aggressive dress will yield a sharper wheel and was corroborated by the measured larger slopes and lower asperity densities as seen in Section 4.2 (page 86). Again, the 3-D model was better at predicting forces than the 2-D model and also yielded a slope much closer to the experimental slope. The forces of the coarse dress (Figure 4.13, page 103, $a_d = 60$ μm) were much the same as those of the medium dress with the tangential forces dropping slightly. This indicates that the increase in dressing in-feed from $a_d = 30$ μm to $a_d = 60$ μm does not significantly affect wheel sharpness. The distribution of asperity density as seen in Figure 4.5 (page 90) showed only a small change in values between medium and coarse dressings – particularly at low values of h_{eq}. The distribution of asperity slopes seen in Figure 4.7 (page 93) also showed less of a change when compared to the fine dressing. These small changes may account for the slight drop in tangential forces between medium and coarse dressings. Again, the 3-D model was more accurate at predicting forces. The normal forces were somewhat under-predicted for the coarse dress. It is interesting to note there is not a significant difference in the predicted 3-D forces between the dressed and worn profiles. This is most likely due to the fact that the dressed topography of the coarsely dressed wheel was similar in asperity density (Figure 4.6, page 90) to the worn wheel indicating that the wheel was tending to a "natural topography" independent of dressing (as found by Rowe *et al.* [33]). Of the three dressings, the coarsely dressed wheel was closest to this value for the worn profile for asperity density. Therefore, there was not a significant change in the wheel topography and predicted forces throughout wear of the wheel.

The largest deviation between predicted and measured values in the 3-D model occurred in the medium and the coarse dress at small values of h_{eq}. This could be due to several factors. The slopes of the grits at small values of d_w are smaller and may approach the transitional region from cutting to plowing, making the assumption of cutting suspect for very small values of h_{eq}. However, the smallest experimental force was taken at h_{eq}=0.005 which corresponds to an attack angle in the model of $\alpha>19°$. This is well within the region of cutting even with large values of f and large values of H_s/H_b. A more probable explanation is that accurate measurement of F_n is more difficult for small forces because of the presence of coolant forces acting on the dynamometer along with other sources of noise in addition to the possibility of hydrodynamic pressure lubricant film support both of which become more obtrusive at smaller force values.

For the medium dress, the tangential forces are somewhat over-predicted at larger values of h_{eq}. The relative drop in experimental forces is most likely due to re-sharpening of the wheel. Why this is not reflected in the predicted values – as a profile was taken immediately after these tests – is unclear. It is possible that grinding was halted at a point in the wear flat/re-sharpening cycle just before grit pullout where re-sharpening would have occurred.

5.1.2. Set 2: EN39B with VA Wheel.

The predicted values for grinding of case-hardened EN39B with a VA wheel and fine dressing (Figure 4.14, page 104) were much better with the 3-D model than with the 2-D model. The 3-D model predictions were very accurate with experimental forces falling between the dressed and worn predictions except at low values of h_{eq}. The 3-D predictions for the medium dress (Figure 4.15, page 105) and the coarse dress (Figure 4.16, page 106) were also very good. Both normal and tangential forces were under-predicted at small values of h_{eq}. The predicted slopes were also much more accurate for the 3-D model than with the 2-D model. Considering the varying hardness throughout grinding of EN39B, predicted values were fair for the 2-D model and are excellent for the 3-D model.

5.1.3. Set 3: Creep-feed Grinding of M2 with RA Wheel.

The measured forces for creep-feed grinding of M2 in Figure 4.17 (page 107) for both dressing conditions are well predicted. The 2-D model under-predicted the tangential forces throughout. The 3-D model accurately predicted both the normal and tangential forces. Normal forces were over-predicted at large values of h_{eq}. Experimental forces did not show any change with the different wheel dressing indicating that the resin alumina wheel was self-sharpening throughout. This was indeed what was observed as, during grinding, a significant amount of smoke was seen as the high temperatures caused melting of the resin which exposed fresh cutting grits. Tangential forces are slightly under-predicted for most values of h_{eq}. There are several possible explanations for this. First, during creep-feed grinding with a RA wheel, self-sharpening of the wheel was present with the generation of wear flats and grit pullout. This means that the topography of the wheel was changing throughout. Wheel profiles were taken after grinding when the wheel was in a single condition. Second, it is more difficult to obtain constant forces in creep-feed grinding. Lastly, the motor attached to the wheel head was pushed to its limit of power so that the wheel was slowing down. It was assumed that the wheel velocity was constant as measured under no-load conditions. This means that the actual values of h_{eq} would be higher than those calculated because $h_{eq}=Z'/V_s$ so when V_s decreases, h_{eq} increases. Therefore, the actual experimental points should lie slightly further to the right bringing them closer to the predicted values for the tangential forces although increases the error for the normal forces.

5.1.4. Set 4: EN31, EN39B, M2 with CBN Wheel.

Predicted and measured forces for tests with a CBN wheel with neat oil are shown in Figure 4.18 (page 108) for EN31, Figure 4.19 (page 109) for case-hardened EN39B, and Figure 4.20 (page 110) for creep-feed grinding of M2. Again, predictions are much better with the 3-D model than with the 2-D model.

For the 3-D predictions of grinding of EN31, forces are over-predicted – although the predictions are better for the tangential forces. For grinding of case-hardened EN39B forces are over-predicted although there is significant scatter in the experimental points. In addition, the slope of the experimental points is extremely large suggesting a loss of hardness with further grinding into the case. For creep-feed grinding of M2, tangential forces were very well predicted and normal forces were over-predicted. The reason for the discrepancy is unclear. It is possible that the increased sharpness of the CBN grits was not well measured using the profilometry spacing of 8 μm. As seen in Section 4.2.2 (page 87), an increase in the resolution, although unlikely to affect asperity density, might increase asperity slopes slightly. This would bring down the forces, particularly at small values of h_{eq} where they were consistently over-predicted.

5.2. Discussion of Parameters Used in Models.

5.2.1. Coefficient of Friction.

The success of both models is partly due to the correct choice of disposable constants in the predictive equations. The two main constants which are not determined independently are the friction factor (f) used in both models and the "contact ductility" used in the 2-D model. The contact ductility is the strain required to produce a wear particle in the wave model regime - which determines the metal removal rate. Of these two parameters, it is the friction factor which has the most influence on the results. Raising the friction factor has the effect of raising both normal and tangential forces for a given metal removal rate and generally of increasing the ratio of tangential to normal force. The present results – specifically those from the 3-D model – are sufficiently encouraging to warrant further development and, clearly, one of the first priorities must be to develop a suitable method for the independent determination of the friction factor. Previous experience suggests that the friction factor should lie between 0.1 for a good oil coolant and 0.4 for a water-based coolant. According to Johnson [50] and Tabor [42] who researched the shear strengths of thin organic films between sliding surfaces, the

boundary films associated with conventional liquid lubricants yields a value of approximately $f=0.1$. Our models achieved good correlation with $f=0.4$ for soluble oil and $f=0.1$ for neat oil. The choice of the interfacial friction is based on the work of Lacey and Torrance [25] and Torrance and Parkinson [63]. Xie and Williams [4] used values of $f=0.5$ for shell Tellus 37 oil and turbine oil 68, and $f=0.6$ for base oil which seem exceptionally high. They also used $f=1.0$ for dry contact. Those values from Challen *et al.* [58] and Black *et al.* [66] are closer to those we chose. A comparison of values for f is given in Table 5.1.

Table 5.1. Values of f from different researchers and used in models.

Reference	f	Lubricant
Williams and Xie [3]	0.1	Ordinary lubricating oil
	0.12	Base oil with no additives packages
	1.0	Dry contact
Challen *et al.* [58]	0.028	Boundary lubricant tests with Dow Corning Molykote 321R, 10 µm thickness coating
	0.096	Shell Vitrea 68 straight mineral oil – no additives
Black *et al.* [66]	0.034	Boundary lubricant tests with Dow Corning Molykote 321R, 10 µm thickness coating
	0.088	Shell Vitrea 68 straight mineral oil – no additives
Values used in model	0.10	Castrol Vacmul 2105 Neat Oil
	0.40	Castrol Hysol X Soluble Oil, 4% dilution in water

Although there are published values of f for various lubricants, there are not any published values for water or soluble oil in water. We chose a value of $f=0.4$. This choice can be substantiated as follows. Ye and Pearce [136] compared grinding forces and specific energies in grinding using water and oil coolants. They measured the ratio of forces using oil coolant to forces using water coolant and found the following ranges.

$$\frac{F_{n,oil}}{F_{n,water}} \approx 2.1 \text{ to } 2.6 \tag{74}$$

$$\frac{F_{t,oil}}{F_{t,water}} \approx 1.2 \text{ to } 1.5 \tag{75}$$

We can plot the theoretical ratio F_n/F_t from the 3-D model for values of f=0.1 and f=0.4 along with the experimental ratio from the grinding results. This is shown in Figure 5.1 below. The top graph gives the values from h_{eq}<0.1 where the EN31 experimental points lie for soluble oil. The bottom graph gives values for h_{eq}<0.8 where the M2 experimental points lie for neat oil. For the EN31 results, we can see that as the equivalent chip thickness increases, the theoretical ratio decreases until it approaches a steady-state value where the experimental points lie. This decrease in the ratio is because larger values of h_{eq} lead to more efficient grinding with larger proportions of cutting and smaller proportions of rubbing and plowing. The same trend can be seen for the theoretical values in the bottom graph for M2. We can see that oil coolant lead to higher ratios than water-based coolants. The experimental points also show the same trend. The plots also indicate that Xie and Williams model is not as accurate at extremely low and extremely high values of h_{eq}.
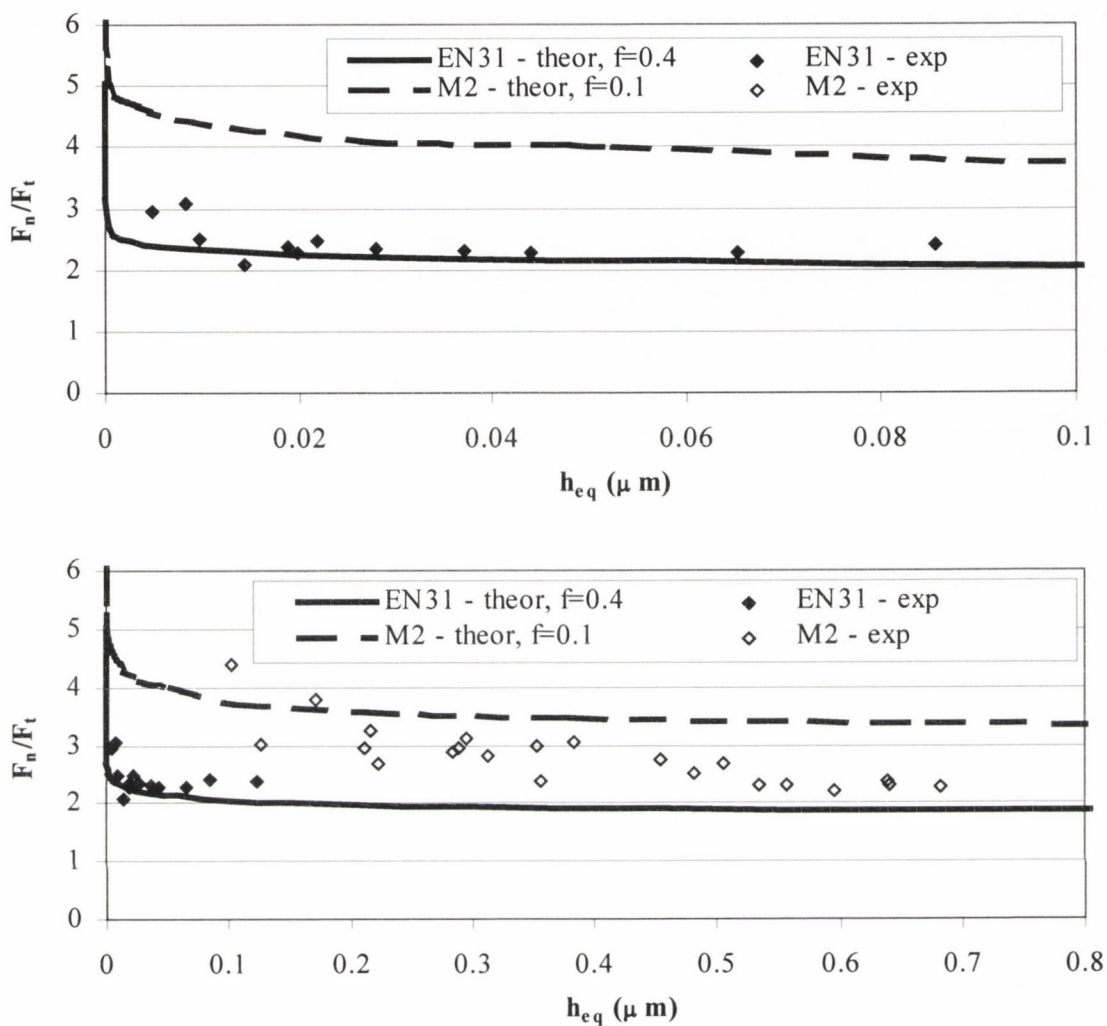
Figure 5.1. Ratio F_n/F_t – theoretical and experimental.

We can use Ye and Pearce's values for the ratios of oil and water and compare them to the experimental results to justify the use of $f=0.4$ for soluble oil. If we divide the first ratio by the second ratio from above and rearrange the terms, we get

$$\frac{\dfrac{F_{n,oil}}{F_{n,water}}}{\dfrac{F_{t,oil}}{F_{t,water}}} = \frac{\dfrac{F_{n,oil}}{F_{t,oil}}}{\dfrac{F_{n,water}}{F_{t,water}}} \tag{76}$$

This gives two ratios that were measured and are shown in the figures above. If we use the values of Ye and Pearce and take a mean value for each we get

$$\frac{\dfrac{F_{n,oil}}{F_{n,water}}}{\dfrac{F_{t,oil}}{F_{t,water}}} = \frac{mean-value(2.1...2.6)}{mean-value(1.2...1.5)} = \frac{2.35}{1.35} = 1.74$$

(77)

Similarly, if we take the ratio from the experimental values for oil and water at $h_{eq}=0.1$ which is in a range of h_{eq} where there is good agreement between the theoretical and the experimental forces for both materials we get

$$\left. \frac{\dfrac{F_{n,oil}}{F_{t,oil}}}{\dfrac{F_{n,water}}{F_{t,water}}} \right|_{h_{eq}=0.1} = \frac{3.6}{2.05} = 1.76.$$

(78)

which is reasonably close to the value of 1.74 from Ye and Pearce. Because previous researchers have given measured values of f for oil but not for water, the agreement between the above two ratios indicates that the value of f=0.4 for water is a reasonable choice.

If we look at the effect of using different values of f on the predicted forces, we can see that, as shown in Figure 5.2, below (Set 1, EN31, VA wheel, coarse dress, dressed profile), using a value of f=0.3 or f=0.5 does have a significant effect and choosing the correct value of f significantly affects the predicted forces. In addition, the scatter of the experimental points crosses over several values of f indicating that, even if an exact measurement of f could be obtained, the predicted values would still fall within the region of experimental scatter.
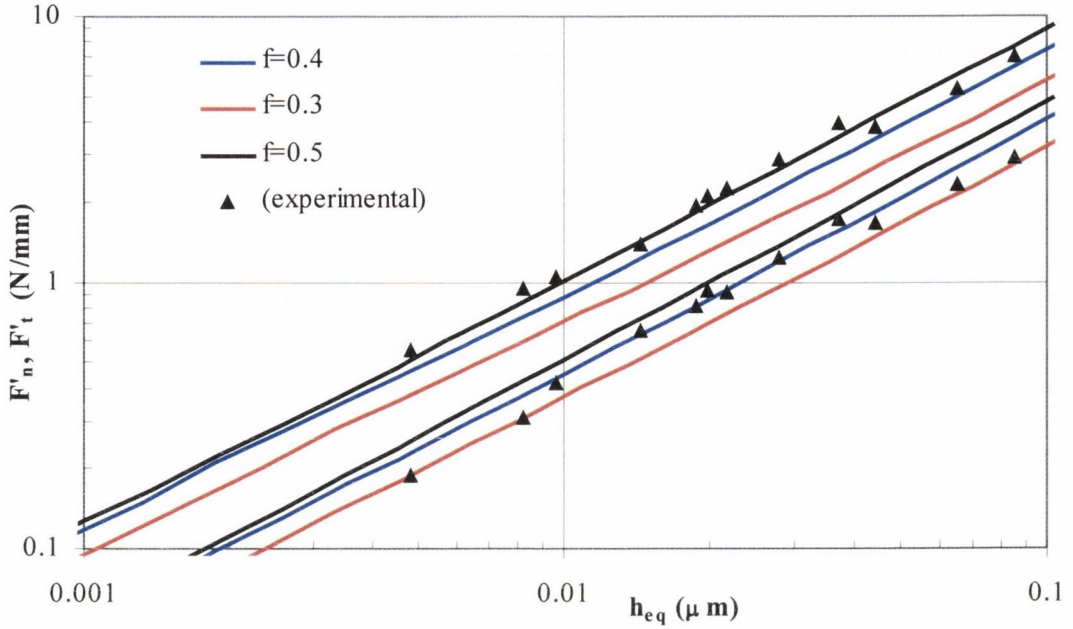
Figure 5.2. Effect of *f* value on predicted forces.

5.2.2. Profilometry.

Another area which needs attention is the measurement of the wheel profile. Firstly, the stylus method used here is rather slow and is also wasteful of data storage space. Only a small part of the profile actually intervenes in the grinding process - the top 1% to 5% of the wheel surface. Bhattacharyya and Hill [138], in their use of profilometry, found that measurement of the first 50 μm of the profile was more than adequate. As seen in Figure 4.10 (page 96) of the change in slopes with wheel wear, the effected area is only in a very small region. This occurred in the first 7 μm of the wheel depth. For a profile with a peak to valley distance of 280 μm, this accounts for only the top 2.5% of the wheel. Thus, most of the data acquired by standard profilometry is largely irrelevant. This has an unfortunate side effect: the sample size used in determining the effective grit slopes is rather small. In the present work, several profiles were used in an attempt to improve this, but there is clearly much room for further improvement.

The traverse speed used for taking profiles was 0.2 mm/s. At this speed the profiles did not seem to exhibit any degree of "bounce". Bhattacharyya and Hill [138] successfully used a speed of 0.5 mm/s with a similar method of taking circumferential wheel profiles. The spacing between profilometer samples was 8 μm for the VA wheel and 4 μm for the RA wheel. This corresponds to roughly half the scratch width. Greater accuracy could be achieved with a finer spacing. Bhattacharyya and Hill [138] used a spacing of 1 μm in the radial direction. For the slope of 0.2 measured at the surface for all wheel types, this corresponds to a spacing of 5 μm (1μm/0.2=5 μm). As was discussed in Section 4.2.2 (page 87), a finer grit spacing should not significantl affect grit density or grit slope calculations.

Lastly, it should be noted that profilometry is an imperfect method for analyzing the surface of the wheel. Profilometry is still the most widely used method for surface analysis and its limitations have been widely documented since Abbott *et al.* first did a review of it in 1938 [118]. As the stylus traces out a path along the surface, it will record peaks along its path but will only very occasionally encounter a summit. This is accounted for in the calculation of areal density (Section 1.8.2, page 53) but is, nevertheless, an imperfect representation of the surface of the wheel. Also, because of the geometry of the stylus tip with an included angle of 90°, attack angles of greater than 45° cannot be measured. Although angles of this magnitude occur at larger depths, they are less likely to occur at the grain tips.

Profilometry methods have been extensively used and have proven effective for a variety of tasks [134] – yet are difficult and time-consuming to use on-line and prone to contamination on the shop floor. Other methods which could be incorporated into an on-line device to measure wheel topography are radar, laser, and other optical methods. Maksoud *et al.* correlated measured wheel profiles using a stylus with an on-line air flapper nozzle transducer [139]. Laser methods can be used on-line and are gaining more acceptance, but the difficulties with coolant and loading noise have created difficulties [140]. Brinskmeier and Werner [141] developed an optical sensor based on laser triangulation to measure wheel wear. However, the device sampled the wheel randomly and it seems unlikely that genuine slope values could be obtained. More recently, Gotou and co-workers

[142,143,144,145] developed a laser system for measuring the extent of wear flats which can measure 50 mm^2 of wheel surface in 1.9 seconds while the wheel is running at 30 m/s. The device can be used for both dry and wet conditions, but greater accuracy was achieved under dry conditions. It should by possible to translate the wear flat area measurements to asperity densities. If the measurements could also be translated into slope distributions, then an on-line method for assessing when grinding forces and temperatures become dangerous could be implemented.

5.2.3. Criteria for Asperity Cutting Point Selection.

The criterion used to distinguish between a grit and an asperity also needs to be considered. As shown in the SEM photo in Figure 1.3 (page 11) and found by others [16,124,135,46], a single grit may have several cutting asperities. For our analysis, a peak is considered an asperity if its height is greater than all values a minimum distance (d_p) on either side. If this distance is small, then a single grit can have multiple asperities. A CIRP co-operative study [128] discussed defining a cutting point it if protruded at least 5 μm above adjacent valleys and two cutting points as belonging to the same grain if they were spaced closer than one grain dimension apart. Figure 5.3 shows the effect of smoothing and also how d_p affects the asperity density for a VA wheel with a mean grit diameter of 251 μm. A least square fit was made though each set of data points and is represented by a line. The effect of smoothing is also shown in the case of d_p=32 μm. It is evident that the distance between asperities has a significant affect. A value of d_p=32 μm is most likely too low and a value of d_p=192 μm is most likely too high considering the mean grit diameter. Considering this and taking into account the mean grit diameter ($D_{g,mean}$), a value of d_p=64 μm was chosen for the VA wheel ($D_{g,mean}$=250 μm), a value of d_p=40 μm was chosen for the RA and CBN wheels ($D_{g,mean}$=152 μm). This gave a consistent value of $D_{g,mean}/d_p \approx 4$ for all cases. Considering this, and that Verkerk [128] stated that about 40% of active cutting points are spaced closer than the mean grain diameter, a value of $D_{g,mean}/d_p \approx 4$ was considered reasonable.
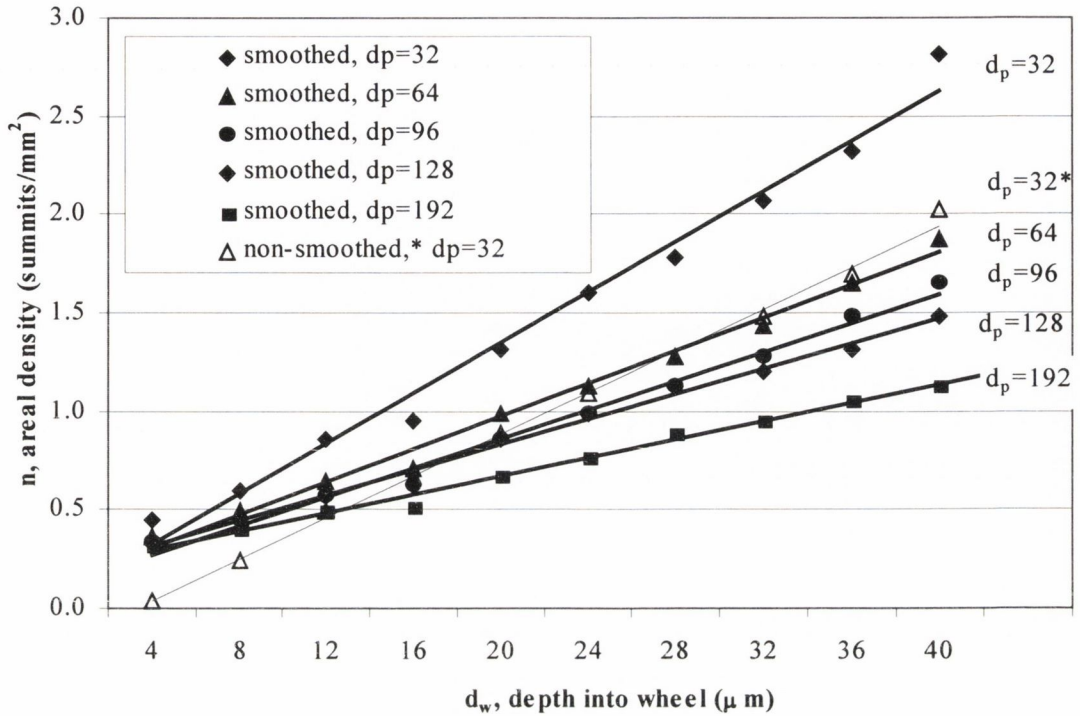
Figure 5.3. Relationship between n and d_p – medium dress.

5.2.4. Average Slope and Normalized Slope Distribution.

The final assumption that needs to be addressed is the use of an average slope used in the slope distribution. In reality, at a given depth there will be a distribution of slopes. However, the length of a profile required to obtain a meaningful statistical sample at each depth is enormous. Therefore, an average value was chosen and assumed to fit a normal distribution. This was applied to the non-linear relationship with specific wear rate, $K \propto \tan^3 \alpha$, as explained in Section 2.2.3 (page 68). For the example shown in Figure 2.2, the distribution increased the specific wear rate by 66%. Therefore, it was considered prudent to include the assumed distribution in the calculations.

5.2.5. Attack Angle for Transition between Cutting and Plowing.

Kopalinsky [72], in her model of the cutting regime in grinding using slip-line fields, used a mean attack angle of $\alpha_{trans}=35°$ based on the findings of Doyle and

Samuels [74], Opitz *et al.* [75] and Rubenstein *et al.* [76]. This corresponds to a slope of 0.70 which seems extremely large even for the sharpest wheel at any depth. Kopalinsky, in her application of chip-formation slip-line fields to temperature calculations in grinding [77], used values of asperity angles of $\alpha=60°,56°,52°,48°$ (slope=1.7,1.5,1.3,1.1) corresponding to different degrees of wheel wear. These values were calculated based on assumed orthogonal cutting using slip-line fields on an initially flat workpiece. For the angles found experimentally here and by others [126,127] for grit slopes, particularly at the grit tips, these values of transitional attack angle seem exceptionally large if applied to grinding.

More recent work by Suzuki and Inasaki [127] found values ranging from 7° to 43° with an average of 30° (corresponding to a slope of 0.58). This is almost identical to the slope calculated by profilometry at large depths – although there is no mention of the wheel type or depth at which measurements were taken. In addition, the grains in a polycrystal tend to take the shape of a tetrakaidekahedron [146], where the corner included angle is 120°. A perfectly sharp tetrakaidekahedron would therefore have an attack angle of 30° on average, which corresponds to the average value measured here in Sets 1 and 2 (Figure 4.7, page 93) and also by Suzuki and Inasaki [127].

Research from orthogonal cutting has yielded values for critical attack angles much larger than the angles found on a grinding wheel. Research from oblique cutting yielded values of critical attack angles smaller than those found by orthogonal cutting yet still somewhat larger than those encountered in grinding wheels. However, models of oblique cutting have not typically taken into account strain-hardening of the workpiece which lowers the transitional attack angles – nor have they taken into account parallel wear tracks which lowers the transitional attack angle significantly. The use of parallel wear tracks by Xie and Williams yielded much lower values than those of oblique cutting in flat surfaces. The values of α_{trans} found by them approach more closely the angles found in a grinding wheel. If we examine the map of transitional angles found in Figure 1.17 (page 47) and Figure 2.3 (page 71), we see that, as stated by Xie and Williams [4], for conditions of

overlapping wear tracks virtually all attack angles will produce some degree of micro-cutting and metal removal.

Considering this, the fact the specimens tested here will not work-harden appreciably, the fact that Xie and Wiliams found critical attack angles close to those encountered at the grain tips for grinding [4] (Figure 1.17, page 47 and Figure 2.3, page 71), and the fact that grinding will produce a high degree of overlapping tracks, it was considered reasonable to assume that the angles measured here correspond to a region above the transition from plowing to cutting so that the assumption of micro-cutting is valid.

5.2.6. Indenter Geometry.

The geometry used in Xie and Williams model of abrasion assumes an indenter geometry of only one variable – the attack angle – the included and dihedral angle being dependent on the attack angle. Although real grits do often resemble this scenario, as illustrated in Figure 1.3 (page 11), in reality grits will have some variation of attack angle, dihedral angle and included angle. In addition, the dressing process does not necessarily create an isotropic surface. The action of the dressing diamond, with contact tangential to the surface, may produce grit fracture that could lead to different characteristics in the tangential and axial directions. In order to investigate the variation of grit shapes in both the axial and circumferential directions, a three-dimensional map of the grinding wheel would be necessary that is beyond the scope of this work. Stout *et al.* [147] have created such a map of a ground workpiece using a standard profilometer with the workpiece affixed to a table which was capable of moving perpendicular to the direction of motion of the stylus. Inasaki created a map of the topography of the grinding wheel using an optical device [126] and used it to measure asperity density and slopes. If the results from such a map were analyzed in both directions, the anisotropy of the wheel could be measured and the relationship between attack angle and included angle could be investigated. For the analysis here, the surface was assumed to be isotropic as research has not been encountered to indicate otherwise.

5.2.7. Surface Hardness.

The 3-D model takes into account the strain-hardening of the workpiece in the H_s/H_b term in the specific wear rate equation. The 2-D model does not take into account strain-hardening. Estimates can be made of this value, although the range is quite large. Kopalinsky, Oxley and Young [67] developed a slip-line field model of strain-hardening that could be used, although implementation could be time-consuming. However, for the measured surface hardness values given in Table 4.3 (page 97), it is clear that by using some method for correcting the values for the 2-D model, the accuracy would not be improved significantly enough to compare to the more accurate 3-D model. Figure 5.4, below, shows the effect of strain-hardening on the normal and tangential forces for the 3-D model (EN31 with VA wheel). It is evident that strain-hardening does have a significant effect and cannot be ignored. The measured values of surface hardness after grinding for the hardened steel specimens had a value of $H_s/H_b \approx 1.1$. From the figure we can see that any errors resulting from neglecting strain-hardening or estimating it would not be inconsequential but would also not be detrimental to the predictions.

As noted by Torrance [103], hardened high carbon steel does not work-harden a great deal. Considering that chip formation is predicted to be suppressed in materials which work harden strongly so that plowing will dominate over cutting, materials with high ductility would lie higher on the curve, would be harder to grind – as found in practice [10,11] – and strain-hardening could not be neglected in force predictions for them. However, for the hardened steels tested here, the measured values of surface hardness after grinding used in the 3-D model were more than adequate for the calculations.
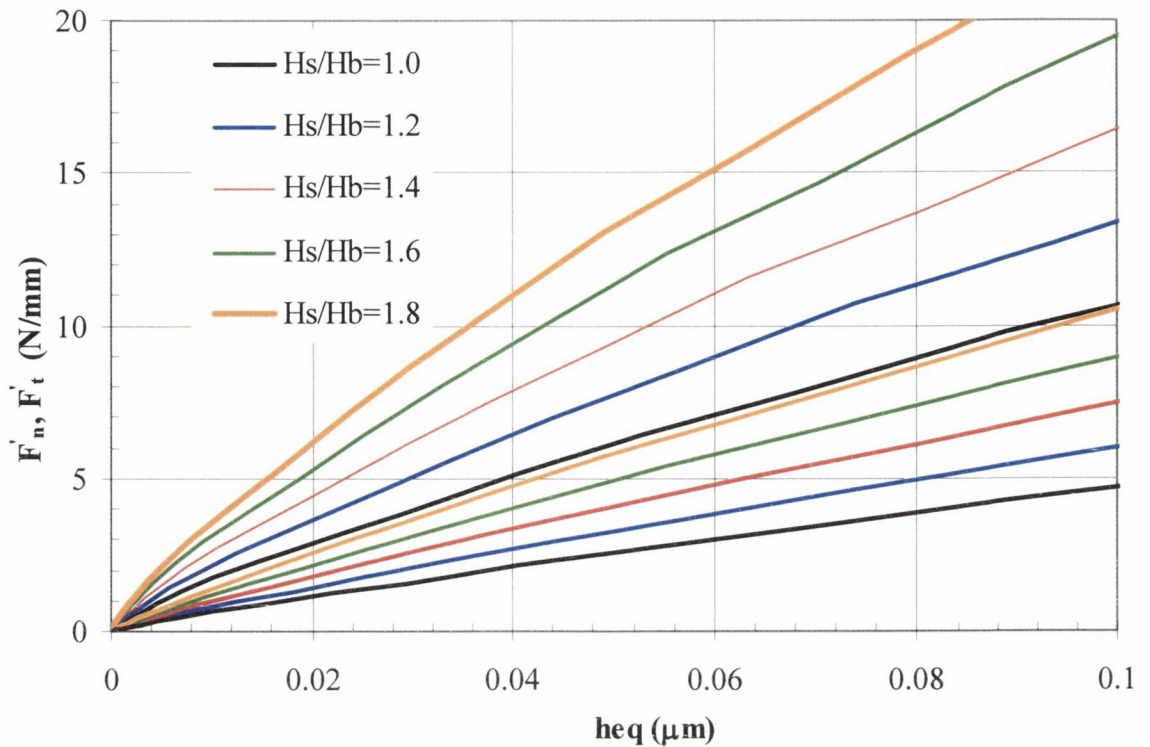
Figure 5.4. Effect of strain hardening of forces.

5.2.8. Surface Hardness, Grindability, and Carbide Distributions.

The hardness of the workpiece is a good indicator of the grindability of a material. However, materials of similar hardness values may have significant variations in grindability due to the presence and distribution of carbides. Morgan and Salter [148] measured specific energies of hard and soft steels in creep-feed grinding and found that materials of similar hardness may have very different specific energies due to blunting of the wheel by carbides. The ASP steels are made from atomized powder, so their primary carbides are about an order of magnitude smaller than those in M2 which is made by conventional casting and forging. The effect of this is illustrated in Figure 5.5, below, from grinding tests performed at Trinity College.
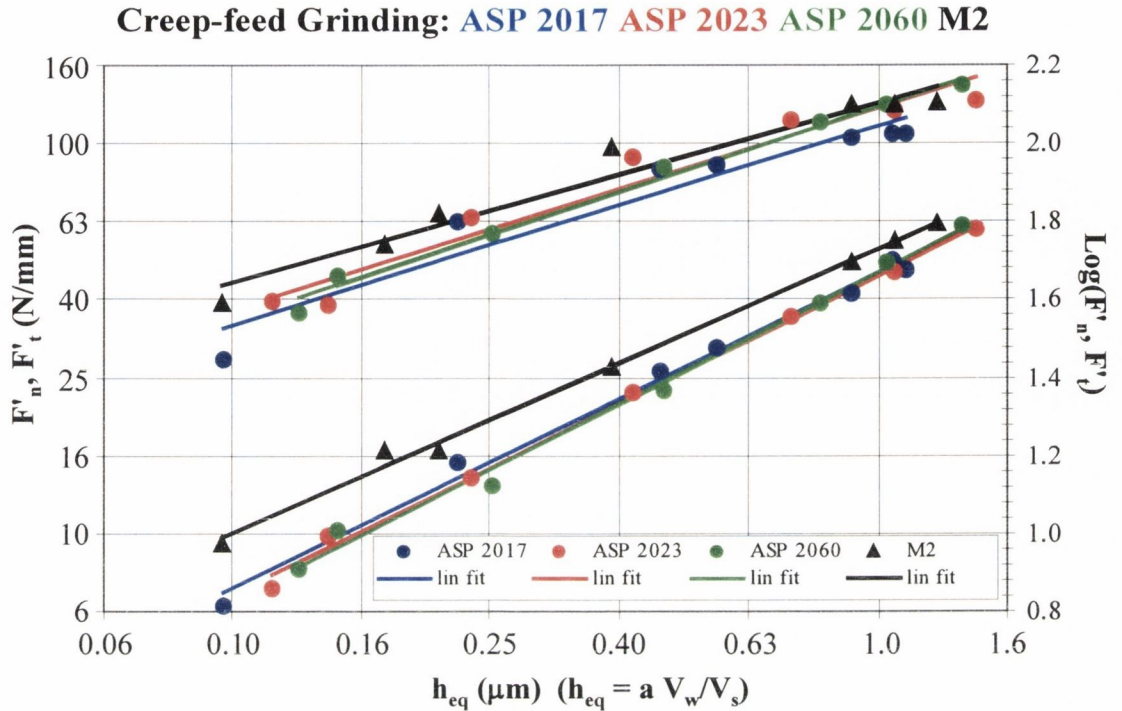
Figure 5.5. Creep-feed grinding of ASP and M2 steels.

Peters suggested a relationship between the grindability of a material and the slope of an F'_t versus h_{eq} curve plotted on log-log scale [11]. He stated that a smaller value of the slope of the F'_t curve indicates a material that is more difficult to grind From Table 5.2 below, it is evident that all three grades of ASP have approximately the same slope. The M2 steel has a lower slope than the ASP grades indicating that it is harder to grind. However, the ASP 2060 has the highest hardness value. It is higher than the M2 in spite of being easier to grind. This is most likely because of the distribution of smaller sized carbides produced by the atomized powder. This indicates that hardness is not a perfect indicator of the grindability of a material. The primary inputs to the model are the bulk and surface hardness values. For materials with large carbide clusters, severe wear of the wheel may lead to a rapid change in forces which would need to be reflected in the slope and asperity distributions. However, for the tests performed here, the measurement of profiles after dressing and after grinding was adequate to account for this effect.

Table 5.2. ASP and M2 steel hardness and grindability values.

Steel	Hardness R_c	Slope of F'_t curve
ASP 2017	65.1	0.81
ASP 2023	65.7	0.82
ASP 2060	68.4	0.84
M2	65.9	0.73

5.2.9. Hardness at Elevated Temperatures and High Strain Rates.

Both models use hardness values taken from measurements at room temperature. During grinding, temperatures at the grinding interface can reach 800 °C or higher [149,45]. At these elevated temperatures, hardness will drop considerably. Conversely, very high strain rates are imposed on the workpiece during grinding. At these high strain rates, hardness values tend to increase. The relationship between the two is complex and data is typically not available for the temperature ranges and strain rates encountered during grinding. Hastings and Oxley [69] attempted to overcome this by using the flow stress data of Oyane *et al.* [133] from high-speed compression tests for a range of carbon steels. This had data for strain rates of about 450/s which is still much lower than those encountered in machining. They extrapolated these values to strain-rates encountered in machining (10^3 to 10^6/s). They then used the velocity modified temperature concept of Macgregor and Fisher [150] which gave a modified temperature based on the actual strain rates. While this approach is reasonable if the necessary data is available, the extrapolation into a region far outside the measurements make the estimates of hardness uncertain. Considering this, and that fact that data have not been encountered for the materials used here, it is assumed that the effect of higher temperatures acting to lower hardness values and the effect of high strain rates raising hardness values tend to cancel each other out and a standard hardness measurement taken at room temperature is adequate.

5.2.10. Changes in Wheel Topography with Wheel Wear.

For the VA wheel used here, 2-D predictions were made for profiles taken after dressing and 3-D predictions were made both with profiles taken after dressing and after grinding. The changes observed in wheel topography during grinding – in terms of asperity density and asperity slope – were significant and this was reflected in the predicted forces. In reality, the wheel topography will be dynamic throughout. Depending on the wheel grade and the extent of attritious wear and re-sharpening, the wheel will either become blunt until forces increase and high temperatures cause workpiece burning or the wheel will blunt and the forces will increase such that wheel re-sharpening will occur and the process will take on a cyclic nature. As found by Rowe *et al.* [33] and Chen *et al.* [151], the power consumed in grinding quickly drops and then gradually increases with wheel wear as shown in Figure 5.6. As seen in the distributions for the VA wheel, it appears that the topography approaches a "natural topography" as the wheel wears.
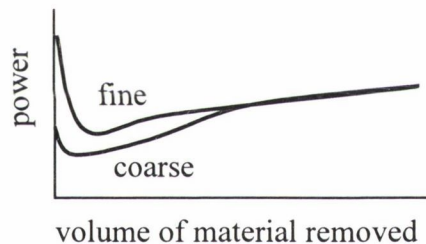
Figure 5.6. Change in power with metal removal.

The grinding models proposed here predict the forces for a given wheel topography. Once this topography is known, it can be used to predict forces for a wide range of conditions. However, attritious wear at the tips will cause forces to increase until the forces are large enough for grit/grain fracture and re-sharpening of the wheel. Currently, the model does not reflect these changes unless direct measurements are made of the wheel throughout the grinding tests. Further development of the model would take into account the complex process of wheel wear This change can be reflected in the predictions if consideration is given to the wear of the wheel – either in direct measurement of the wheel wear or in estimating how wheel wear will affect the density and slope predictions.

5.3. Application of 3-D Model to the Other Results.

The models proposed here predict forces for a given wheel topography. For the more accurate 3-D model, this requires a profile of the wheel for the calculation of asperity densities and slopes. In practice, measurement of such profiles is time-consuming and tedious. A method of determining the asperity slope and asperity density distributions without the need for time-consuming measurements would be of great assistance. In addition, this would allow the possibility to investigate different parameters to achieve optimum performance without the necessity of time-consuming experiments.

For a given wheel type, the variables in dressing are the dressing depth, the dressing lead and the diamond radius. Torrance and Badger [130] have developed a model of single-point or blade dressing based on the statistics of brittle fracture of bonds and grits and on the geometrical interaction between the grits and the dressing tool. It predicts the asperity density and slope distributions for a given set of dressing conditions and is called the "GRASP" program (Grinding forces from Asperity Slope Prediction). The derivation of the equations used in the model is rather lengthy and is given in Appendix 5.

To further validate the 3-D force model, it would be beneficial to apply the model to previously published grinding forces to see how well it can predict the forces. For this, we can use the dressing model to predict the slope and density distributions. For this, we need data on the material properties of the abrasive grain.

There is data on the way the characteristic force for grit removal varies with wheel grade [37], which allows the possibility of attempting to model some results published in the literature. The results of Snoeys and Peters [10] were chosen for this exercise because they included details of their grinding and dressing parameters used in their experiments. They ground hardened steel workpieces (100Cr6) of similar hardness to those ground here and performed grinding tests with both neat oil and soluble oil coolant. They prepared an experimental grinding chart for cylindrical grinding with

- wheel type: EK60L7VX
- workpiece: 100Cr6
- coolant : (i) 100% EPS12 , (ii) 3% SB-C in Water
- D_{wheel}=665 to 720 mm
- D_{work}=83 to 100 mm
- V_s=60 m/s
- V_w=1 m/s,
- s_d=0.2 mm
- a_d=0.05 mm

From Brecker [152] we find that the crushing strength of a single crystal alumina is only 85% of that of white alumina, whilst from Peklenik [37] it is evident that the bond strength of an L grade wheel is 67% greater than that of an H grade wheel. This gives almost enough information to predict Snoeys and Peters's results, but the diamond radius is missing. In the absence of any other information, a value of 0.46 mm was chosen which was measured from the diamond diameter of 0.92 mm used in Set 1 and Set 2.

Therefore, Torrance and Badger's method of predicting wheel asperity density and slope can be applied to the conditions used by Snoeys and Peters. Once the necessary distributions are known, they can be used in the 3-D model of grinding to predict the forces measured by Snoeys and Peters.

The derivation of the model is rather lengthy and is given in Appendix 5. The predicted density and slope distributions and force predictions from these using the 3-D model are given below along with the force measurements from Snoeys and Peters.

5.3.1. Application of Dressing Model to Predict Wheel Characteristics.

Snoeys and Peters gave plots of normal and tangential forces versus equivalent chip thickness for cylindrical grinding of 100Cr6 steel with a EK607VX wheel for both oil and water-based coolants. They used the following relationship between forces and equivalent chip thickness

$$F'_t = F'_1 \cdot h_{eq}^{\ f} \qquad\qquad (79)$$

$$F'_t = \frac{F'_1}{\mu} \cdot h_{eq}^{\ f} \qquad\qquad (80)$$

and fit values for F_1, f and μ to their grinding results. Details of the dressing conditions and force results are given in Table 5.3 below.

Table 5.3. Grinding and dressing conditions of Snoeys and Peters.

Wheel:	EX60LVX
Workpiece:	100Cr6 hardness: 62-63 $R_C \Rightarrow$ mean=62.5 R_c = 759 HV)
Coolant:	(i) 100% EPS12
	(ii) 3% SB-C in Water
Dressing:	s_d=0.2 mm/rev
	a_d=50 µm 3X

	(i) oil coolant	(ii) soluble oil coolant
µ	0.30	0.36
f	0.78	0.78
F_1 (N/mm)	17	28
$e_{0.1}$* (J/mm^3)	28	48
* $e_{0.1}$=specific energy when h_{eq}=0.1		

The required inputs to the dressing model are the wheel grade and grit size, the dressing lead, the dressing depth and the dressing diamond radius. Therefore, all the necessary parameters are known except for the diamond radius which was assumed to be 0.46.

If these parameters are used in the model, the asperity density and asperity slope distributions are predicted as shown in Figure 5.7 below.

133
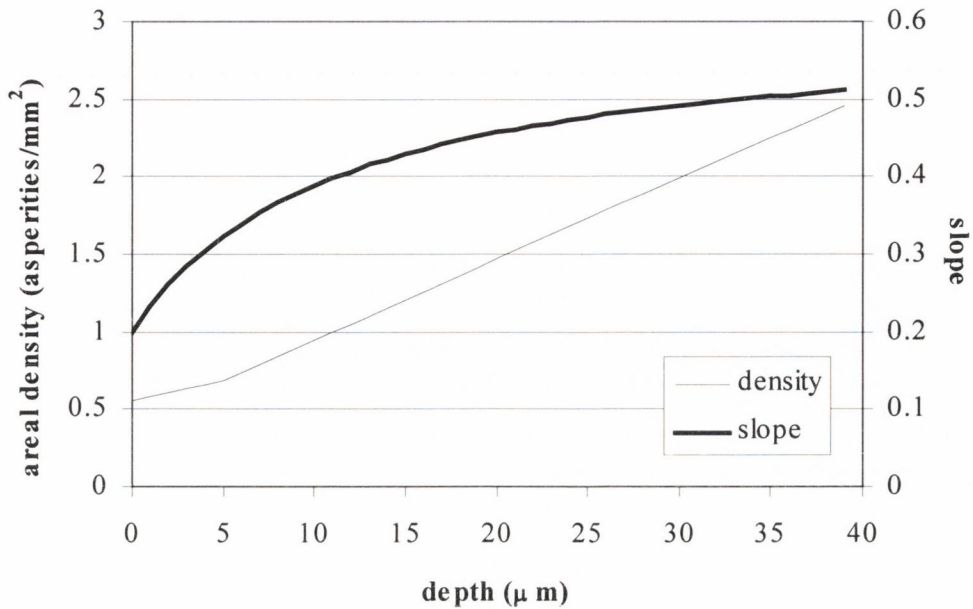
Figure 5.7. Predicted density and slope distributions for (i) and (ii).

5.3.2. Application of 3-D Model to Results of Snoeys and Peters.

Now that the density and slope distributions are known, they can be used in the 3-D model of grinding to predict the forces. The hardness was given by Snoeys and Peters for the workpiece. However, no data was given for the surface hardness after grinding. Since the material is hardened steel, we can assume that it does not have a great deal of strain hardenability. The ratio H_s/H_b from Set 1 with the EN31 was $H_s/H_b=1.11$. Therefore, we can use that to estimate a value of

$$H_s=1.11 \cdot 759 = 842.5 \text{ HV}.$$

The wheel and workpiece diameters are given. Therefore, the only unknown left is the friction factor f. The two coolant types are neat oil and soluble oil. The soluble oil is 3% solution which is not far from the percentage used in the soluble oil in Set 1 and Set 2. If we use the same values as those which were successfully used in the first tests we get

(i) $f=0.4$ EPS 12 100% neat oil

134

(ii) f=0.1   SB-C 3% soluble oil

which are reasonable assumptions for the data given.

Now we can use the 3-D model to predict the grinding forces for Snoeys and Peters. If we plot the empirical fit of the results of Snoeys and Peters using the constants they gave (μ, f and F_1) and the predicted values from the 3-D model we get the results as shown in Figure 5.8 for Set (i) with neat oil and Figure 5.9 for Set (ii) with soluble oil. Snoeys and Peters results are plotted from the empirical constants they published and does not show the experimental scatter. Again, results are given in log-log scale and linear scale.
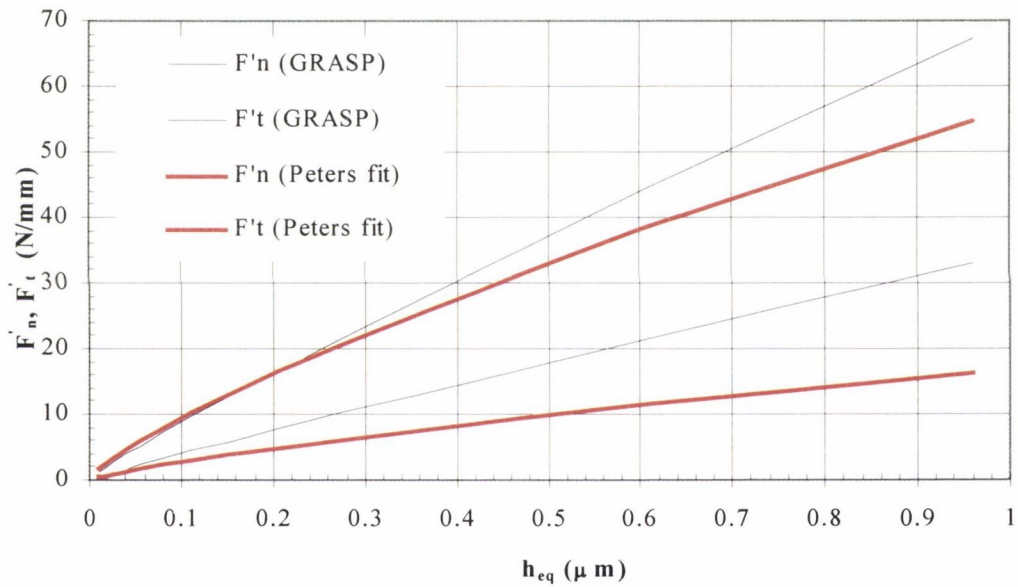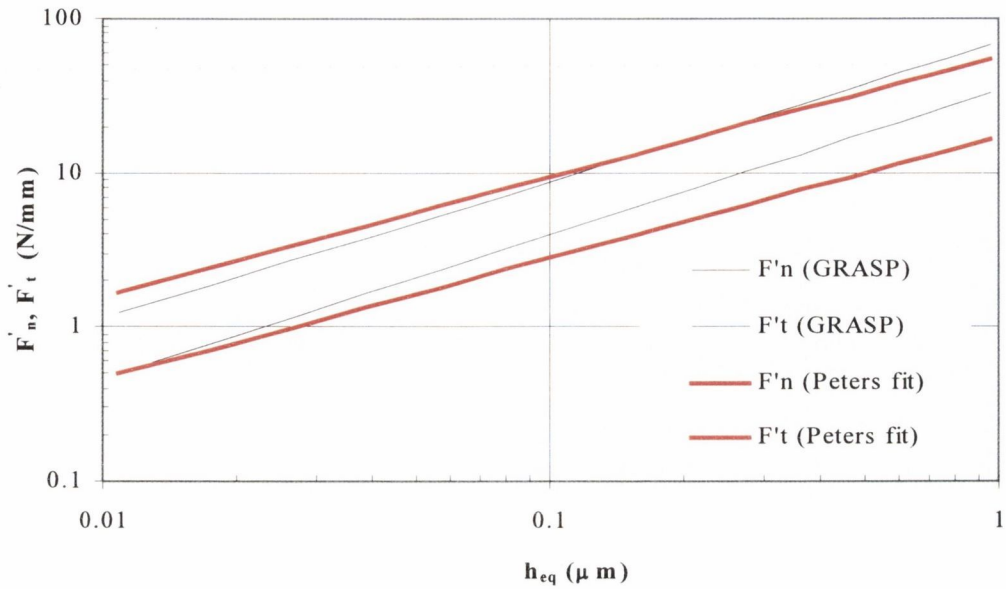
Figure 5.8. Predicted and measured forces for Snoeys and Peters, (i) neat oil.
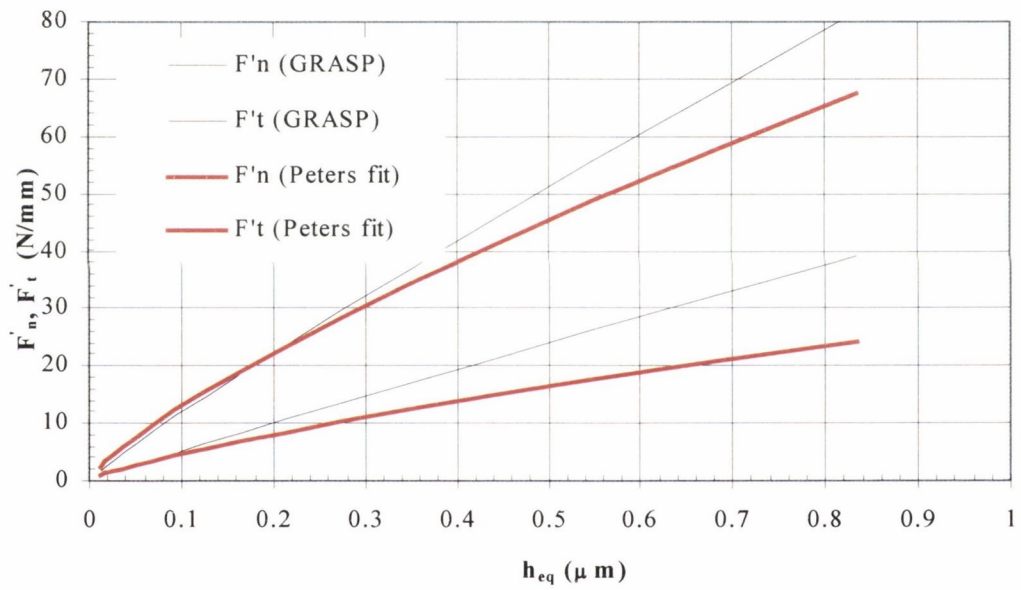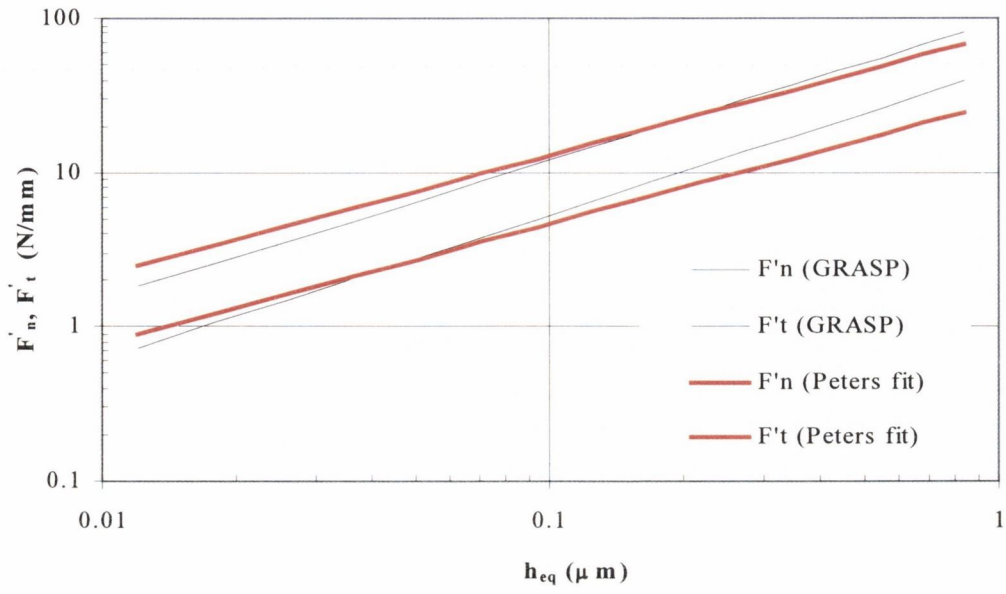
Figure 5.9. Predicted and measured forces for Snoeys and Peters, (ii) soluble oil.

5.3.3. Discussion of Predictions of Snoeys and Peters.

The results show that using the dressing model to predict density and slope distributions and applying the predictions to the 3-D force model to predict forces can achieve reasonably accurate results. This was achieved in spite of the numerous assumptions that were necessary because of the lack of information on the dressing and grinding conditions. Table 5.4 below shows the constants that were fitted to the predicted results compared to those found by Snoeys and Peters.

Table 5.4. Measured and predicted constants for Snoeys and Peters.

	(i) neat oil coolant		(ii) soluble oil coolant	
	Measured [10]	**Predicted**	**Measured** [10]	**Predicted**
F_1	17	34.3	28	44.2
f	0.78	0.93	0.78	0.92
μ	0.30	0.46	0.36	0.44
$e_{0.1}$ (J/mm3)	28	40	48	53

From the table and the figures we can see that the predictions are reasonably accurate, particularly in light of the assumptions made and for the region where the measured values are valid, $h_{eq}<0.6$. The slope constant (f – slope of log-log graph) is slightly over-predicted in both cases. The intercept (F_1 – intercept of the linear log-log graph) and the μ constant (F_n/F_t ratio) and the specific energy are all somewhat over-predicted – although all show consistent trends. This indicates that perhaps the dressing model under-predicted the sharpness of the wheel. On the other hand, the values of h_{eq} at the higher end of the plot are rather large for this grade of wheel indicating that perhaps re-sharpening was occurring which could not be accounted for in the dressing model. In fact, considering that forces were under-predicted at low h_{eq} and over-predicted at high h_{eq} indicates that this is likely.

5.3.4. Conclusions of Predictions of Snoeys and Peters with Models.

The predictions of the density and slope distributions of Snoeys and Peters from the dressing model were based on the following assumptions:

- Dressing diamond radius
- Abrasive properties
- Bond properties

Considering the errors introduced with the assumptions in the dressing model, the predicted forces correlated very well with the measured forces from the literature.

Therefore, if all the parameters for a given set of grinding conditions are known along with the material properties of the wheel, there is sufficient evidence that the force model proposed here, when used with the dressing model proposed here, can predict within reasonable limits the forces for any set of grinding conditions.

5.4. Application of Model to Estimate Workpiece Surface Roughness.

Since the dimensionless distance between tracks discussed by Xie and Williams [3, 4] represents, effectively, a series of scratches running parallel to the direction of contact and is similar to those found on ground surfaces by profilometry, it should be possible to apply the model to predict surface roughness values based on wheel topography and grinding conditions.

Malkin found a linear relationship between specific energy and surface roughness [82] indicating that increased efficiency in metal removal by grinding leads to larger values of surface roughness. Torrance and Badger applied Xie and Williams's model of a series of overlapping wear scratches and related it to the efficiency of the process to predict the surface roughness of the workpiece. This was published in [130] and the lengthy derivation of the model is given here in Appendix 5. This method for predicting surface roughness was applied to the results of grinding EN31. In these tests, the roughness of the workpiece was not measured systematically in this series of tests, but simply at the end of each test campaign; so there is only one result available for each dressing condition. These correspond to the highest metal removal rate in the campaign, and are shown in Table 5.5, below. As noted by Chen *et al.* [84], during spark-out, the cutting depth decreases and the proportion of plowing and rubbing increases. However, for the method of incrementing the in-feed before every pass that was used here, the sparkout phase of grinding was not allowed to occur so that the full depth of cut used in grinding can be applied to calculate the value of h_{eq} when grinding ceased.

Table 5.5. Measured and predicted roughness values.

Dressing condition	h_{eq} (μm)	Measured roughness	Theoretical roughness
Fine	0.06	0.42 μm	0.42 μm
Medium	0.12	1.02 μm	0.80 μm
Coarse	0.16	0.87 μm	0.86 μm

The results are very good – particularly for the fine and coarse dress – and fall within experimental error. However, it would be necessary to perform many more measurements under more carefully controlled conditions to validate properly this prediction method. For instance, the roughness measured will vary as a function of the way the data is filtered, something which was not particularly well controlled here, as the main purpose of the work undertaken was to predict forces as an aid to predicting the safe limits of the grinding process.

Nevertheless, the results shown here indicate that the method proposed can predict well the values of surface roughness. Since this is an important parameter in quality control in grinding and achieving low values of surface roughness while maintaining safe thermal grinding conditions is desirable, the incorporation of this into the grinding model is an important development and a useful tool in assessing the performance of the process.

5.5. Quantification of Wheel Sharpness.

The accuracy of the force predictions presented here suggests that the sharpness of a grinding wheel could be scientifically measured through the way its asperity slope and asperity density vary with depth into the wheel. Inspection of the figures of slope versus depth into the wheel shows that the slopes vary with depth in the same way as the slope of a hyperbola. If the slope versus depth distribution of a wheel could be described by the slope of a hyperbola, it would be possible to use the constants of the hyperbola to quantify the wheel sharpness.

The equation for a hyperbola is:

$$\left(\frac{y}{b}\right)^2 - \left(\frac{x}{c}\right)^2 = 1 \tag{81}$$

where y=d+b and d is the depth into the wheel. Differentiating we get:

$$\frac{dy}{dx} = \frac{b}{c}\frac{x}{\sqrt{x^2 + a^2}} = \frac{b}{c}\frac{\sqrt{y^2 - b^2}}{y} = \frac{b}{c}\frac{\sqrt{d^2 + 2db}}{d + b} = S \tag{82}$$

If we insert values of s and d into the equation, we can calculate b since we have assumed that the limiting slope (=b/c) is 0.6 (Figure 4.7, page 93). A sharp wheel would be characterized by a small value of b, which implies that the slope builds up rapidly as d increases, whilst a blunt wheel would be characterized by a large value of b implying a slow build up of slope with d. For the three dressing conditions used here, b was calculated for values of d between 1 and 20 μm. The following average values were found for the three dressings

- fine dressing: $b = 26$ μm
- medium dressing: $b = 13$ μm
- coarse dressing: $b = 13$ μm

Curves of slope versus depth were then calculated from equation (82) using these values and were found to be virtually indistinguishable from curves in Figure 4.7 (page 93).

The other parameter that affects the wheel sharpness is the areal asperity density, n. If we take the value of n at a depth into the wheel of 4 µm we get

- fine dressing: $n_{4 \, \mu m} = 0.45 \; /mm^2$
- medium dressing: $n_{4 \, \mu m} = 0.35 \; /mm^2$
- coarse dressing: $n_{4 \, \mu m} = 0.25 \; /mm^2$

so that a sharp wheel would be characterized by a small value of $n_{4 \, \mu m}$ and a blunt wheel would be characterized by a large value of $n_{4 \, \mu m}$. Therefore, if we multiply b by the square root of $n_{4 \, \mu m}$ we get a dimensionless sharpness number defined as

$$\text{Sharpness} = \frac{1}{b\sqrt{n_{4 \, \mu m}}} \tag{83}$$

In the equation, the slope value has a greater effect than the density which has also been observed in research on wear flat area [17]. If we correct for the units and substitute the values for b and for $n_{4 \, \mu m}$ from above, we get

- fine dressing: Sharpness=57.3
- medium dressing: Sharpness=130.0
- coarse dressing: Sharpness=153.8

If we compare these values to the specific energy at h_{eq}=0.1 we get

- fine dressing: $e_{0.1} = 57.3$ J/mm^3
- medium dressing: $e_{0.1} = 37.0$ J/mm^3
- coarse dressing: $e_{0.1} = 32.0$ J/mm^3

For both the sharpness value and the specific energy, there is large difference between the fine and medium dressing. The difference is not as large for both values between the medium and coarse dressing. This indicates that this parameter is a good indicator of the sharpness of the wheel. If this could be incorporated into the force model, a threshold value could be placed on the limit for safe grinding. As the attritious wear of the wheel increased, the value of b would increase. Unless this was countered by a corresponding decrease in of $n_{4\ \mu m}$ with resharpening of the wheel, forces would increase until thermal damage would occur. This would correspond to a threshold value for the sharpness number.

Therefore, a quantifiable value for the sharpness of the wheel has been developed that is supported by experimental measurements. Clearly, additional experiments and measurements would need to be made to validate the procedure. If this could be accomplished, limits of safe grinding could be established based upon this sharpness number.

CHAPTER 6. CONCLUSIONS.

Two methods for calculating grinding charts from wheel profiles have been proposed and experimental and predicted results were compared. The first method is based on Challen and Oxley's two-dimensional slip-line field model of the contact between grit and workpiece. The second is based on Xie and Williams's three-dimensional quasi-upper bound energy minimization model of a three-dimensional asperity generating a series of grooves on the workpiece. The primary input to both models is the measured wheel profile. The other inputs required are readily available (machine settings, material properties) or can be easily measured (hardness of the workpiece, *etc.*).

Both models were capable of predicting grinding forces. However, the results were much more accurate for the three-dimensional model than for the two-dimensional model. All three sets for the three different dressings of the VA wheel for grinding of EN31 fell into the range of experimental error and the fine and medium dress fell into the band between the predicted forces for the dressed and worn wheel. The slight under-prediction of normal forces for the coarse dress could possibly be due to the decrease in temperature in the workpiece from the coarse dress leading to less reduction in workpiece hardness. Therefore, the material would in fact be harder to grind leading to higher experimental forces not reflected in the model. However, the tangential forces were well-predicted and both fell within the range of experimental error.

The forces for EN39B were surprisingly well-predicted considering the varying hardness throughout the case. All three sets fell within experimental error.

The forces for M2 for the two dressings were well-predicted with the exception of values at high values of h_{eq}. There are several factors to consider here. First, at high values of h_{eq}, the wheel is experiencing a large degree of self-sharpening that may not be well-reflected in the profile measurements taken after grinding. This would lead to an over-prediction of forces. Secondly, the large power required for grinding

will lead to a slowing down of the wheel. In the calculation of h_{eq}, a constant wheel speed measured for no-load was assumed. Therefore, actual experimental values of h_{eq} will be at lower wheel speeds so that actual experimental values of h_{eq} should be higher than those calculated and lie further to the right on the graph. This would lead to an even greater over-prediction. Lastly, the long arc of cut and high temperatures during creep-feed grinding will lead to a softening of the material ahead of the grinding zone. Therefore, actual grinding forces would be lower than those predicted. Considering that two of these points will lead to over-prediction and one will lead to under-prediction, this may partly account for discrepancy at large values of h_{eq}.

The predictions for grinding with a CBN wheel were the least successful – although still reasonably accurate. For EN31 the forces were over-predicted, for EN39B they were over-predicted except at high values of h_{eq} and for M2 they were over-predicted for the normal forces but well-predicted for the tangential forces. The reasons given above for M2 are also applicable here. However, the most notable characteristic is the difference in slope values – which were too low in all cases. This indicates that the stylus may not be picking up the larger slopes in the grits. Considering that CBN grits tend to retain their sharpness – and the limitations in the stylus included angle and the sampling interval, both discussed earlier – this appears to be a likely explanation.

In any case, the results show that the 3-D method proposed here is capable of predicting the forces in grinding. The primary advantage of this method is that once the distributions of cutting asperities for a given dressing condition are measured, various workpiece characteristics, grinding machine settings and wheel grades can be rapidly assessed without the need for time-consuming trials. Then, the most effective way of handling a particular job can be found. Both programs generated a theoretical grinding chart within 20 seconds using a standard IBM 486 PC. Therefore, computation time is not a significant hindrance, and numerous combinations of grinding conditions can be quickly calculated.

Further developments which could be beneficial would be to determine how different dressing conditions – particularly dressing lead – affect slope and asperity

density distributions and also how slope and density distributions change with wear of the wheel. The dressing model given in the Appendix which predicts density and slope predictions shows promise but clearly further development and verification with additional wheel types would be necessary. Then, knowing the effect of wear on the distributions would be necessary to determine the entire grinding cycle. Once this is accomplished, it would be possible to predict wheel topography and, in turn, grinding forces, based on dressing parameters.

It is evident from the results presented here that the three-dimensional model of abrasion applied to grinding is far more accurate at predicting forces than the two-dimensional model. The primary reasons for this are as follows:

- The 2-D model assumes plane-strain – an unrealistic assumption for the complex geometry of the wheel.

- The 3-D model is based on three-dimensional energy minimization – although an indirect method compared to the direct plane-strain model, it is more realistic in terms of the actual geometry at the grit/workpiece interface.

- The 3-D model allows for the simultaneous plowing of side ridges, wedge formation in front of the grit and cutting in the form of chip formation to the sides along with plastic deformation beneath the grit. This is more realistic than the either/or scenario of rubbing, plowing or cutting of the 2-D model.

- The 3-D model takes into account parallel wear tracks. This has significant implications on transitional attack angles and wear modes. The consideration of parallel wear tracks led to smaller transitional attack angles that were closer to those measured here and by previous researchers.

- The theoretical transitional attack angles from plowing to cutting for orthogonal plane-strain models are too high to be realistic for grinding. The values for oblique models are closer but are still too high when considering their neglect of the dimensionless distance between tracks. The orthogonal model of Xie and Williams with its consideration of strain-hardening and parallel wear tracks – both of which act to lower the transitional attack angle and increase wear rates – predicts transitional attack angles which are closer to those angles observed in actual grinding wheels.

147

The two-dimensional model, although a reasonable place to begin because of its simple and direct application, does not accurately reflect the true nature of grinding. Any further development should focus on the three-dimensional model.

It would be advantageous if the following aspects of the model could be investigated.

- Additional grinding experiments which include different dressing conditions – particularly the effect of dressing lead and its effect on asperity density and asperity slope distributions.
- Additional grinding experiments for different workpiece materials – particularly for materials with high ductility. The materials tested here were hardened steel in accordance with the request of the industrial sponsors.
- An examination of the mechanisms behind attritious wear and grit/bond fracture and the effect of wheel wear on asperity slope distributions.
- An examination of the effect of strain-hardening for materials with high strain-hardenability and the effect of elevated temperature and high strain-rates on workpiece hardness.
- A method of directly measuring the friction coefficient, f.

In addition, it was demonstrated here that the model can be used to predict surface roughness values – although additional tests with a greater focus are needed to validate this technique. The sharpness number proposed here is very useful in quantifying the sharpness of the wheel and could be further applied to predict safe levels of grinding.

Further development of the three-dimensional model, while taking into consideration the additional points discussed above and further validation for different workpiece types and abrasive types, will results in even greater accuracy and confidence in predicting forces for a variety of grinding conditions.

The model developed in this thesis, while accurately accounting for the complexities and peculiarities of abrasive wear, is a valuable addition to the understanding of the complex grinding process and is an effective practical tool for the grinding engineer.

REFERENCES

1.   Challen, J.M. and Oxley, P.L.B. An explanation of the different regimes of friction and wear using asperity deformation models. *Wear*, 1979, **53**, p. 229-243.

2.   Williams, J. A. and Xie, Y. The Generation of wear surfaces by the interaction of parallel grooves. *Wear*, 1992, **155**, p. 363-379.

3.   Xie, Y. and Williams, J. A. The generation of worn surfaces by the repeated interaction of parallel grooves. *Wear*, 1993, **164**, p. 864-872.

4.   Xie, Y. and Williams, J. A. The prediction of friction and wear when a soft surface slides against a harder rough surface. *Wear*, 1996, **196**, p. 21-34.

5.   Badger, J. A. and Torrance, A. A. A Comparison of two models to predict grinding forces. Recently accepted for publication by *IMechE Journal of Engineering Manufacture*. Publication date not yet known.

6.   Lindsay, R.P. Dressing and its effect on grinding performance. *Technical paper MR 29-568, American Society of Tool Manufacturing in Engineering*, 1969.

7.   Lindsay, R.P. Principles of grinding. In R.I. King and R.S. Hahn. Handbook of Modern Grinding Technology, Chapman and Hall, London, 1986.

8.   Lindsay, R.P. The effect of wheelwear rate on the grinding performance of three wheel grades. *Ann. CIRP*, **32/1**, p. 247-249. 1983.

9.   Lindsay, R.P. The effect of contact time on forces, wheelwear rate and G-ratio during internal and external grinding. *Ann. CIRP*, **33/1**, p. 193-198.

10.   Snoeys, R. and Peters, J., A. The significance of chip thickness in grinding. *Annals of the CIRP*, **23**(2), 1974, p. 227-237.

11.   Peters, J. Contribution of CIRP Research to Industrial Problem in Grinding. *Ann CIRP*, 1984, **33**/1, p. 193-197.

12.   Torrance, A.A. The Correlation of Process Parameters in Grinding, *Wear*, **139**, 1990, p. 383-401.

13.   Malkin, S. Grinding Technology. Ellis Horwood Ltd. 1989.

14.   Joseph, N. and Malkin, S. Minimum Energy in Abrasive Processes. *Wear*, 1975, **32**, p. 15-23.

15. Marshall, E. R. and Shaw, M. C., Forces in Dry Surface Grinding, *Trans. ASME*, 1952, **74**, p. 51.

16. Backer, W.R., Marshall, E.R., and Shaw, M.C. The Size Effect in Metal Cutting. *Trans. ASME*, 1952, **74**, p. 61.

17. Malkin, S. and Cook, N. H. The Wear of Grinding Wheels: Part 1 –Attritious Wear. *Trans ASME J. Eng Ind.* 1971, **933**, p. 1120-1128.

18. Matsuo, T., Toyoura, S., Oshima, E., and Ohbuchi, Y. Effect of Grain Shape on Cutting Force in Superabrasive Single-Grit Tests. *Annals of the CIRP*. 1989, **38**/1, p. 323-327.

19. Younis, M., Sadek, M. M., and El-Wardani, T. A New Approach to Development of a Grinding Force Model. *Trans ASME Jrnl. Eng for Ind*, 1987, **109**, p. 306-313.

20. McAdams, H.T. The Role of Topography in the Cutting Performance of Abrasive Tools. *Trans ASME Jrnl. Eng for Ind.* 1964, p. 75-81.

21. Shaw, M.C. A New Theory of Grinding, Harold Armstrong Conference on Production Science in Industry, Melbourne, The Institution of Engineers, Australia, p.1.

22. Merchant, M.E. Basic Mechanics of the Metal Cutting Process, *J. of Applied Mechanics*, **15**, 1944, p. A168.

23. Brenner, N. and Torrance, A.A. Wheel Sharpness Measurement for Force Prediction in Grinding. *Wear*, 1992, **32**, p. 15-23.

24. Badger, J. A. and Torrance, A. A. A computer program to predict grinding forces from wheel surface profiles using slip-line fields. *Proceedings of the Int. Sem. on Improving Machine Tool Performance.* San Sebastian, Spain. 1996, p. 445-456.

25. Lacey, P. and Torrance, A.A. The calculation of wear coefficients for plastic contacts. *Wear*, 1991, **145**, p. 367-383.

26. Torrance, A.A. and Buckley, T.R. A Slip Line Field Model of Abrasive Wear. *Wear* 1996, **196**, p. 35-45.

27. Malkin, S. and Cook, N. H. (1971). The Wear of Grinding Wheels: Part 2 – Fracture Wear. *Trans ASME J. Eng Ind.* 1971, **933**, p. 1129-1133.

28. Verkerk, J. *Ann. CIRP*, **28**(2), 1979, p. 487.

29. Malkin, S. Specific Energy Mechanisms in Abrasive Processes. *Proc. 3rd N. American Metal Working Research Conf.* Carnegie Press, 1975, p. 453.

30. Narayanaswamy, K. Radhakrishan, V. and Narayanamurthy, R.G. Analysis of surface reproduction characteristics of different replica materials, *Wear*, **57**, p.63-69. 1979.

31. Pande, S.J. and Lal, G.K. Effect of dressing on grinding wheel performance. *Int. J. MTDR*, **19**(3), 1979, p. 171-179.

32. Pattinson, E.J. and Chisholm, A.W.J. The effect of dressing techniques on grinding wheel wear. *Proc. Int. Conf. On Manufacturing Technology.* A.S.T.M.E. p. 601.

33. Rowe, W.B., Chen, X. and Mills, B. Towards an adaptive strategy for dressing in grinding operations. *Proceedings of the 31st Int. MATADOR conference, UMIST*, 1995. p. 415-420.

34. Pacitti, V. and Rubenstein, C. The influence of the dressing depth of cut on the performance of a single point diamond dressed alumina grinding wheel. *Int. J. MATADOR.* **12**, p.267, 1972.

35. Verkerk, J. Characterization of wheel wear in plunge grinding. *Annals of the CIRP*, **26/1**, p.127, 1977.

36. Pandit, S. M. and Sathyanarayanan, G. A model of surface grinding based on abrasive geometry and elasticity. *Journal of Engineering for Industry.* **104**, November 1982, p. 349-357.

37. Peklenik, J. Lane, R. and Shaw, M.C. Comparision of static and dynamic hardness of grinding wheels. *Trans. ASME*, **86**B, 1964, p. 294-298.

38. Wetton, A.G. *Wear*, **13**, 1969, p. 331.

39. Komanduri, R. and Shaw, M.S. *Phil. Mag.* **32**, 1975, p. 225.

40. Briscoe, B.J., Scruton, B. and Willis, F.R. The shear strength of thin lubricant films. *Proc. Roy. Soc, Series A*, **333**, p. 99-114, 1973.

41. Black, K.J., Kopalinsky, E.M. and Oxley, P.L.B. Sliding metallic friction with boundary lubrication: An investigation of a simplified friction theory and of the nature of boundary lubrication. *Wear*, **137**, p. 161-174, 1990.

42. Tabor, D. The role of surface and intermolecular forces in thin film lubrication, *Proc. 34th Int. Meet. Societe de Chimie Physique: Microscopic Aspects of Adhesion and Lubrication,* Elsevier, Amsterdam, 1981, p. 651-682.

43. Yuen, M.F. Dynamics of Grinding, Ph.D. Thesis, Univ. of Bristol, 1977.

44. Yossifon, S. and Rubenstein, C. The Grinding of Workpieces Exhibiting High Adhesion, Part 1 and 2. *Transactions of the ASME*, **103**, 1981, p. 14-15.

45. Johnson, K.L. Contact Mechanics, Cambridge University Press, Cambridge, 1985.

46. Powell, J.W. (1979) The application of grinding fluid in creep-feed grinding, Ph.D. Thesis, University of Bristol.

47. Rowe, W.B., Chen, X. and Morgan, M. N. The identification of dresssing strategies for optimal grinding wheel performance. *Proc. 30th Int. MTDR Conf.*, **30**, p. 195-202.

48. Torrance, A.A. The Statistics of the Extrema of Surfaces as a Means of Assessing Their Mechanical Performance. *Wear*, 1992, **156**, p. 281-299.

49. Werner, G. Influence of Work Material on Grinding Forces, *CIRP*, **25**, 1976, p. 243-248.

50. Rowe, W.B., Black, S.C.E., Mills, B., Mogan, M.N. and Qi, H.S. Grinding temperatures and energy partitioning. *Proc. R. Soc. Lond.* **453**, 1997. p. 1083-1104.

51. Rentsch, R. & Inasaki, I. Molecular Dynamics Simulation for Abrasive Processes. *Annals of CIRP.* **43/1**, 1994, p. 327-330.

52. Green, A.P. The plastic yielding of metal junctions due to combined shear and pressure. *J. Mech. Phys. Solids*, **2**, p.17-211. 1954.

53. Collins, I.F. *Int. J. Mech. Sci*, **14**, 1. 1972.

54. Johnson, R.W. and Rowe, G.W. *Proc. Instn. Mech. Engrs*. **182**, 521. 1968.

55. Bowden, F.P. and Tabor, D. The friction and lubrication of solids. Clarendon Press, Oxford, Part 1 – 1950, Part 2 – 1964.

56. Johnson, K.L. *Proc. 7th Leeds-Lyon Symposium on Tribology*, Leeds, Westbury House. 1980.

57. Challen, J.M. and Oxley, P.L.B. A slip-line field analysis of the transition from local asperity contact to full contact in metallic sliding friction. *Wear*, **100**, p.171-193. 1984.

58. Challen, J.M. McLean, L.J. and Oxley, P.L.B. Plastic deformation of a metal surface in sliding contact with a hard wedge: its relation to friction and wear. *Proc. R. Soc. Lond.* **A394**, 1984, p. 161-181.

59. Y. Yang and A.A.Torrance. Wear by plastic ratchetting: an experimental evaluation. Wear, 196, 1996, p. 147-155.

60. Yang, Y., Torrance, A.A. and Oxley, P.L.B. Modeling mechanical wear processes in metallic sliding friction J. Phys. D Appl. Phys. **29**,1996, pp 600-608.

61. Kapoor, *A. Fatigue Fract. Eng. Mater. Struct.* **17**, p.201-209. 1994.

62. Moalic, H., Fitzpatrick, J.A. and Torrance, A.A. The correlation of the characteristics of rough surfaces with their friction coefficients, *Proc. I. Mech. E.*, **201**, 1987, p.321-329.

63. Torrance, A.A. and Parkinson, A. Towards a Better Surface Finish for Bearing Materials in 19th Leeds-Lyson Sympoium, 1993, Ed. D Dowson and M. Godet Elsevier.

64. Mulhearn, T. O. and Samuels, L.E. The abrasion of metals: a model of the process, *Wear*, **5**, p.478, 1962.

65. Black, A.J., Kopalinsky, E.M. and Oxley, P.L.B. An investigation of the different regimes of deformation which can occur when a hard wedge slides over a soft surface: the influence of wedge angle, lubrication and prior plastic working of the surface. *Wear*, **123**, p. 97-114. 1988.

66. Black, A.J., Kopalinsky, E.M. and Oxley, P.L.B. Asperity Deformation Models for Explaining the Mechanisms Involved in Friction and Wear - a Review. 1993. *Proc. I. Mech. E.* **207**, p. 335-353.

67. Kopalinsky, E.M., Oxley, P.L.B.and Young, H.T. A strain-hardening slip-line field analysis of the plastic deformation observed in a model asperity interaction experiment. *J. Mech Phys Solids*, **38**/6,1990, p. 765-785.

68. Kopalinsky, E.M. Investigation of surface deformation when a hard wedge slides over a soft surface. *Transaction of the ASME Jrnl of Tribology*. **14**, 1992. p. 100-106.

69. Hastings, W.F. and Oxley, P.L.B. Mechanics of chip formation for conditions appropriate to grinding. *Proc. 17th Int. Machine Tool Design and Research Conf. Birmingham*, 1976, Halsted, New york, 1977, p.203.

70. Fenton, R.G. and Oxley, P.L.B. Mechanics of orthogonal machining: predicting chip geometry and cutting forces from work material properties and cutting conditions. *Proc. Inst. Mech. Engr.* **184**, p.927.

71. Hastings, W.F., Oxley, P.L.B and Stevenson, M.G. Predicting a Material's Machining Characteristics Using Flow Stress Preoperties Obtained from High Speed Compression Tests, *Proc. Inst. Mech Engrs.* **188**, p.245, 1974.

72. Kopalinsky, E.M. Modeling of material removal and rubbing processes in grinding as a basis for realistic determination of workpiece temperature distributions. *Wear*, **81** (1982), p. 115-134.

73. Hastings, W.F. PhD. Thesis, University of New South Wales, 1975.

74. Doyle, E.D. and Samuels, L.E. *Proc. Int Conf. On Production Engineering, Tokyo*, 1974, Japan Society of Prec. Engineering and Intern. Inst. For Production Engineering Research, Tokyo, 1974, p. 45.

75. Opitz, W. König, and Werner, G. in M.C. Shaw (ed.) New Developments in Grinding, Carnegie Press, Pittsburgh, 1972, p. 259.

76. Rubenstein, C., Groszman, F.K. and Koenigsberger, F. *Proc Int. Industrial Diamond Conf.*, Oxford, 1966, Industrial Diamond Information Bureau, London, 1966, p. 161.

77. Kopalinsky, E.M. A new approach to calculating the workpiece temperature distributions in grinding. *Wear*, **94,**1984, p. 295-322.

78. Samuels, L.E. Metallographic Polishing by Mechanical Methods, Sir Isaac Pitman and Sons Ltd. 1967.

79. Kruschev, M.M. Resistance of metals to wear by abrasion as related to hardness. *Proc. Conf. On Lubrication and Wear*, Institution of Mechanical Engineers, London, 1957, paper 46.

80. Bowden, F.P. and Tabor, D. *The Friction and Lubrication of Solids, Part II.* Clarendon, Oxford, 1964.

81. Rabinowicz, E. Friction and Wear of Materials, Wiley, New York, 1965.

82. Jacobson, S. Wallen, P. and Hogmark, S. *Wear*, **115**, 1987, p. 987-994.

83. Jacobson, S. Wallen, P. and Hogmark, W. *Rep. UPTEC-87-17R*, 1987, University of Uppsala.

84. Chen, X. and Rowe, W.B. Modeling surface roughness improvement in grinding. *14th National Conference on Manufacturing Research, University of Derby*, 7-9 September, 1998, p.37-42.

85. Chen, X. Strategy for the selection of grinding wheel dressing conditions. PhD. Thesis. Liverpool John Moores University. April 1995.

86. Chen, X., Rowe, W.B., Mills, B. and Allanson, D.R. Analysis and simulation of the grinding process – {Part IV, Effect of wheel wear. *International Journal of Machine Tools and Manufacture*, **38**, No.1-2, p.41-49, 1998.

87. Antler, M. Tribological properties of gold for electrical contacts. *IEEE Trans. Parts, Hybrids, Packag*, **9**, 1973, p. 4-14.

88. Miyoshi, K. Spalvins, T. and Buckley, D.H. Tribological characteristics of solid films deposited on metals by ion plating and vapor deposition, *Wear*, **108**, 1986, p. 169-184.

89. Tian, H. Saka, N. and Rabinowicz, E. Friction and failure of electroplated sliding contacts. *Wear*, **142**, 1991. P. 57-85.

90. Antler, M. and Drozdowicz, E. Fretting failure of electroplated gold contacts, *Wear*. **142**, 1991, p. 265-289.

91. Sedriks, A.J. and Mulhearn, T.O. The mechanics of cutting and rubbing in simulated abrasive processes. *Wear*, **6**, p.457, 1963.

92. Sedriks, A.J. and Mulhearn, T.O. The effect of work hardening on the mechanics of cutting in simulated abrasive processes. *Wear*, **7**, p. 451, 1964.

93. Torrance, A.A. A new approach to the mechanics of abrasion. *Wear*, **67**, 1981, p.233-257.

94. Buttery, T.C. and Archard, J.F. Grinding and abrasive wear, *Proc. Inst. Mech. Eng.*, London, **185**, 1970-1971. p. 337.

95. Childs, T.H.C. The sliding or rigid cones over metals in high adhesion conditions. *Int. J. Mech. Sci* **12**. 1970, p.393-403.

96. More, M.A. Abrasive wear. Treatise on Materials Science and Technology, *Wear*, **13**, Academic, New York, 1979, p. 217-258.

97. Childs, T.H.C. Proc. Inst. Mech. Eng. 202, Part C, 1988, p. 379-395.

98. Lavine, A.S., Jen, T.C. and Malkin, S. Thermal aspects of grinding with CBN wheel. *CIRP Annals*, **38**, 1989, p.557-560.

99. De Vathaire, M., Delamare, F. and Felder, E. An upper bound model of plowing by a pyramidal indenter. *Wear*, **66**, p.55, 1981.

100. Gilormini, P. and Felder, E. Theoretical and experimental study of the plowing of a rigid-plastic semi-infinite body by a rigid pyramidal indenter. *Wear*, **88**, 1983, p. 195-206.

101. Kudo, H. and Tsubouchi, M. Development of a simulation testing machine for friction and wear characteristics of lubricant and tool for extrusion and forging. *Ann. CIRP*, **24**, p.185, 1975.

102. Kato, Hokkirigawa, T. Kayaba, T. and Endo, Y. Three dimensional shape effect on abrasive wear. *J. Tribol.* **108**, 1986, p. 346-351.

103. Torrance, A.A. An Approximate Model of Abrasive Cutting, *Wear*, 1987, **118**, 217-232.

104. Kayaba, T., Hokkirigawa, K. and Kato, K. Analysis of the abrasive wear mechanism by successive observations of wear processes in a scanning electron microscope. *Wear*, **110**, p. 419, 1986.

105. Kato, K. and Hokkirigawa, K. Abrasive wear diagram. *Proc. Eurotrip '85, Ecully*, September 9-12, 1985, Elsevier, Amsterdam, Paper 5.3.

106. Peters, J., Snoeys, R. and Decneut, A. The proper selection of grinding conditions in cylindrical plunge grinding, *Proc. 16ʰ Machine Tool Design and Research Conf.*, Macmillan, London, p. 387, 1976.

107. Buttery, T. Grinding Force Predictions Based on Wear Theory. p. 283-289.

108. Hillan, W., Kranz, O. and Eckolt, K. Reliability of roughness measurement, *Wear*, **97**, p.27, 1984.

109. Torrance, A.A. A three-dimensional cutting criterion for abrasion. *Wear*, **123**, p.87-96. 1988.

110. Grunzweig, J., Longman, I.M. and Petch, N.J. Calculations and measurements on wedge-indentation. *J. Mech. Phys. Solids*, **2**, p.81-86, 1954.

111. Lortz, W. A model of the cutting mechanism in grinding. *Wear*, **53**, p.115-128, 1979.

112. Inasaki, I. Application of Simulation Technologies for Grinding Operations. **VD** Berichte Nr. 1276, p. 197-211. 1996.

113. Kato, K. Wear Mechanisms. <u>New Directions in Tribology. IMechE.</u> September 1997. p.39-56.

114. Atkins, A.G. and Tabor, D. *Journal of Mech. Phys. Solids*, **13**, p.149-164, 1965.

115. Xie, Y. The generation of worn surfaces in sliding contacts with hard asperities. *Ph.D. Thesis*, University of Cambridge, 1994.

116. Nayak, P. R. Random Process Model of Rough Surfaces. *Trans ASME Jnl Lub Tech*, 1971. p. 398-407.

117. Terry, Andrew J. & Brown, Christopher A. A Comparison of Topographic Characterization Parameters in Grinding. . *Annals of CIRP*. **46/1**, 1997, p. 497-500.

118. Abbott, E.J., Bousky, S. and Williamson, D. E. (1938), The profilometer, *Mech. Engng*, 60, p. 205-216.

119. Whitehouse, D.J. Comparison between stylus and optical methods for measuring surfaces. *Annals of the CIRP* **27/2**, 1988, p. 649-653.

120. Thomas, T. R. Rough Surfaces. Chapter 9: Tribology, by Greenwood, J. A., Longman Inc., 1982, p. 191-194.

121. Steffensen, H. & Wanheim, T. (1976) Asperities on Asperities, *Wear*, 1976, pp 87-98.

122. Longuet-Higgins M.S. Phil. Trans. R Soc. London, **A250**, 1957, p. 157-174.

123. Shaw, M. C. and Komanduri, R. The Role of Stylus Curvature in Grinding Wheel Surface Characterization. *Annals of the CIRP*, 1977, **25**/1, p. 139-141.

124. Reichenback, G.S., Mayer, J.E., Kalpakcioglu, S., and Shaw, M.C. *Trans. ASME*, 1956, **78**, 847.

125. Shaw, M. C. Principles of Abrasive Processes. Oxford University Press, 1996.

126. Inasaki, I. Grinding Process Simulation Based on the Wheel Topography Measurement. *Annals of the CIRP*, 1996, **45**, p. 347-350.

127. Suzuki, M. and Inasaki, I. Surface Topography Measurement of Super Abrasive Wheels. *Transactions of the Japan Society of Mechanical Engineers*. 1995. **61**, 249-256.

128. Verkerk, J. Final Report concerning CIRP Cooperative Work on the Characterization of Grinding Wheel Topography. *Annals of the CIRP*, 1977, **26**/2, 385.

129. Abebe, M. and Appl, F.C. *Wear*, **126**, 1988, p.267-283.

130. Torrance, A. A. and Badger, J.A The relation between the traverse dressing of vitrified grinding wheels and their performance. Submitted for Publication, 1999.

131. Maan, N. and Broese van Groenu, A. Low speed scratch experiments on steel, *Wear*, **42**, p.365, 1977.

132. McAdams, H.T. A statistical polyhedron model of abrasive grains. *Trans. ASME*, **86**B, 1964, p. 388.

133. Oyane, M. Takashima, Osakada, K. and Tanaka, H. The Behavior of some Steels under Dynamic Compression. *10th Japan Congress on Testing Materials*. 1967, p.72.

134. Thomas, T. R. Rough Surfaces. J. A., Longman Inc., 1982.

135. Powell, J.W. and Howes, T.D. A study of the heat flux at which burn occurs in creep-feed grinding. *Proceedings 19th International MTDR Conference, Manchester*, p. 629-36, 1978.

136. Andrew, C. (1979) Coolant application in creep-feed grinding. *International Conference on Creep-feed Grinding, Bristol,* p. 167-183.

137. Ye, N.E. and Pearce, T.R.A. A comparision of oil and water as grinding fluids in the creep feed grinding process. *Proc. Instn Mech Engrs.* **198B/4**, 1984, p. 229-237.

138. Bhattacharyya, S. and Hill, C. Characterisation of Grinding Wheel topography and Wear.p. 171-180.

139. Maksoud, T.T.A., Mokbel, A.A. and Morgan, J.E. In-process detection of grinding wheel truing and dressing conditions using a flapper nozzle arrangement. *Journal of Engin. Manufacture*. **211,** 1997.

140. Gotou, E. Kumamoto Institiute of Technology. Personal Correspondance.

141. Brinksmeier, F. and Werner, I. Monitoring of Grinding Wear. *Annals of the CIRP*, **41/1**, 1992. p.373-376.

142. Gotou, E. and Touge, M. In-process Measurement of Wear of Abrasive Grain (1st Report) – Development of Measuring Apparatus and Investigation of Output Wave-form. *Journal of the Japan Society for Precision Engineering,* **60/8**, 1994. p.1149-153.

143. Gotou, E. and Touge, M. In-process Measurement of Wear of Abrasive Grain (2nd Report) – Binary Image-Acquisition System for Wear Flat of

Cutting Edge. *Journal of the Japan Society for Precision Engineering,* **61/12**, 1995. p.1735-1740.

144. Gotou, E., Mutsumi, T. and Yoshifumi, O. In-process Measurement of Wear of Abrasive Grain (3rd Report) – Evaluation of Image Acquired under Wet Condition. *Journal of the Japan Society for Precision Engineering,* **62/9**, 1996. p.1320-1324.

145. Gotou, E. and Touge, M. Monitoring of Wear of Abrasive Grains. Personal correspondence.

146. Ashby, M.F. and Jones, D.R.H. Engineering Materials. Perhamon, Oxford. 1986.

147. Stout, K.J., Sullivan, P.J. and Rowe, W.B. The analysis of the three dimensional topography of the grinding process. *Annals of the CIRP,* **38/1**, 1989. p.545-547..

148. Morgan, J. E., Salter, N.D. The creep-feed grinding of hard and soft steels. *Journal of Engineering for Industry.* **106**, August 1984, p. 229-233.

149. Black, S.C.E., Rowe, W.B., Qi, H.S. and Mills, B. Temperature measurement in grinding. *MATADOR Conference*, p. 20-21 April 1995.

150. Macgregor, C. and Fisher, J. A Veloctiy-Modified Temperature for the Plastic Flow of Metals. *J. Appl. Mech, Trans ASME,* **13**, p.A11, 1946.

151. Chen, X., Allanson, D.R. and Rowe, W.B. Life cycle model of the grinding process. *Computers in Industry,* **36**, p. 5-11, 1998.

152. Brecker, J.N. The fracture strength of abrasive grains. *Trans. ASME, J. Engng. For Ind.* **96**, 1974, p. 1253-1257.

153. Chen, X. and Rowe, W.B. Analysis and simulation of the grinding process. Pt I: Generation of the grinding wheel surface. *Int J. Mach Tools & Manufactur.* **36**, 1996, p. 871-882.

154. Suto, T. and Sata, T. Simulation of grinding processes based on wheel surface characteristics, *Bull Jap Soc. Prec. Engng.* **15** (1), 1981, p. 27-33.

155. Steffens, K. and König, W. Closed loop simulation of grinding. *Ann. CIRP,* **32** (1), 1983, p. 225-259.

156. Baul, R.M. and Shilton, R. Mechanics of metal grinding with particular reference to Monte Carlo simulation. *Proc. 8th MTDR Conf.* **8**(3) Pergamon, Oxford, 1967, p. 923-946.

157. Yoshikawa, H. and Sata, T. Simulated grinding process by Monte Carlo method. *Ann. CIRP*, **16**, 1968, p. 297-302.

158. Yoshikawa, H. and Peklenik, J. Three dimensional simulation techniques of the grinding process II. Effect of grinding conditions and wear on the statistical distribution of geometrical grit parameters. *Ann. CIRP*, **18**, 1970, p. 361-365.

159. Pahlitzch, G. and Brinswick, A.J. Effect of truing conditions on circular grinding, *Ind. Diamond Review*, **14**, 1954, p.185-89 & 212-217.

160. Vickerstaff, T.J. Diamond dressing – its effect on work surface roughness. *Ind. Diamond Review*, **30**, 1970, p. 260-267.

161. Hahn, R. S. and Lindsay, R.J. The influence of process variables on material removal surface integrity, surface finish and vibration in grinding. *Proc. 10th Int. MTDR Conf.*, **10**, p. 95-117. Macmillan, New York, 1969.

162. Kirk, J.A. An evaluation of grinding performance for single and polycrystal grit aluminum oxide grinding wheels. *Trans. ASME J. Engng for Industry*, **98**, 1976, p. 189-195.

163. Vickerstaff, T.J. The influence of wheel dressing on grinding wheel performance. *Int. J. mach Tool Des. Res.* **16**, 1976, p. 145-152.

164. Timoshenko, S.P. and Goodier, J.N. Theory of Elasticity. McGraw Hill, New York, 1970.

165. Sayles, R.S. and Thomas, T.R. A stochastic explanation of some structural properties of a ground surface. *Int. J. Prod. Res.*, **14/6**. p. 651-655. 1976.

BIBLIOGRAPHY

1. Azarkhin, A. and Richmond, O. *Wear*, **157**, 1992, p. 409-418.

2. Malkin, S. and Murray, T. Comparison of Single Point and Rotary Dressing of Grinding Wheels. *Proc. 5th N. American Metal Working Research Conf.* p. 278-83, 1977.

3. Murray, M.J., Mutton, P.J. and Watson, J.D. *J. Lubr. Technol.* **104**, 1982, p. 9-16.

4. Sakamoto, T. and Tsukizoe, T. Friction and scratch deformation of metals. In T Sakurai (ed.), *Proc. JSLE-ASLE Int. Lubrication Conf., Tokyo,* June 9-11, 1975, Elsevier, Amsterdam, p. 49, 1976.

5. Shaw, R.S. and Chawla, R. Experimental Investigation of Wheel Loading in the Grinding of Various Material. *Journ. Eng. Prod.* **3** 1979, India, p. 27-38.

6. Torrance, A.A. The influence of surface deformation on mechanical wear, *Wear*, **200**, p. 45-54., 1996.

7. Torrance, A.A., Galligan, J. and Liraut, G. A model of the friction of a smooth hard surface sliding over a softer one. *Wear,* **212**, 1997, p. 213-220.

APPENDIX 1. FORCES IN CREEP-FEED GRINDING.

Because of the large depth of cut present in creep-feed grinding, the forces measured by the dynamometer are not the true normal and tangential forces relative to the grinding wheel. Therefore, consideration must be given to the actual geometry and corrections must be made to calculate the true normal and tangential forces. Figure A1 shows the geometry of the grinding wheel and workpiece for a given wheel diameter (D_{wheel}), depth of cut (a_c), length of arc of cut (l_a), angle of arc of cut (θ) and offset angle (α).
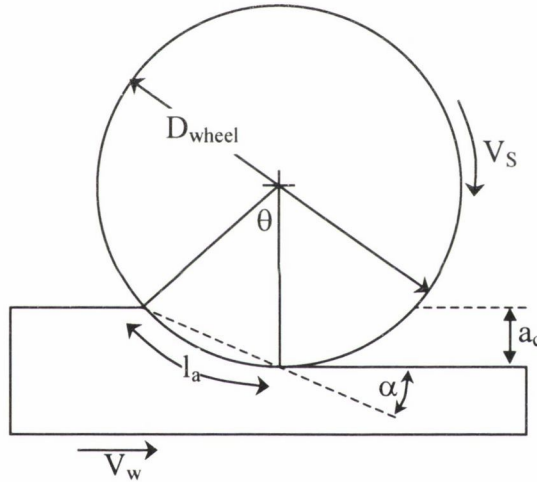

Figure A1. Geometry of wheel and workpiece in creep-feed grinding.

Considering the that

$$l_a = \sqrt{a_c D_{wheel}}$$ (A1)

and

$$\alpha = \frac{\theta}{2} = \frac{360° \dfrac{\sqrt{a_c D_{wheel}}}{\pi D_{wheel}}}{2}$$ (A2),

it follows that the actual normal and tangential forces, $F_{n,a}$ and $F_{t,a}$ can be calculated from the projection of the measured normal and tangential forces, $F_{n,m}$ and $F_{t,\ m}$, from

$$F_{n,a} = F_{n,m} \cos\alpha + F_{t,m} \sin\alpha \qquad (A3)$$

and

$$F_{t,a} = F_{t,m} \cos\alpha - F_{n,m} \sin\alpha \qquad (A4)$$

as shown in Figure A2. This resulted in actual normal forces that were up to 4% higher than the measured forces and actual tangential forces that were up to 25% lower than the measured forces.
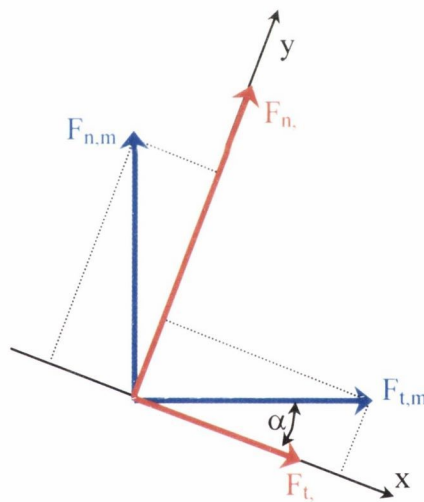

Figure A2. Resolution of normal and tangential forces.

APPENDIX 2. CALIBRATION OF PROFILOMETER.

Calibration of the profilometer was performed in two ways. The first was to rest the tip of the stylus on the top of the wheelhead on the grinding machine and increment the in-feed while recording the voltage output. A plot of displacement versus output voltage yielded a linear relationship and, therefore, a calibration constant (μm /volt) was determined. The wheelhead calibration was verified using a dial gauge. This value was verified by a second calibration using a standard roughness calibration card and traversing the stylus across the card and recording the signal. The RMS roughness was then calculated and a calibration constant was determined to match the known RMS roughness of the card. Both methods yielded constants very close to each other and the constant determined from the former method was used. Results are shown in Table A1and Figure A3.

Table A1. Calibration readings of Profilometer.

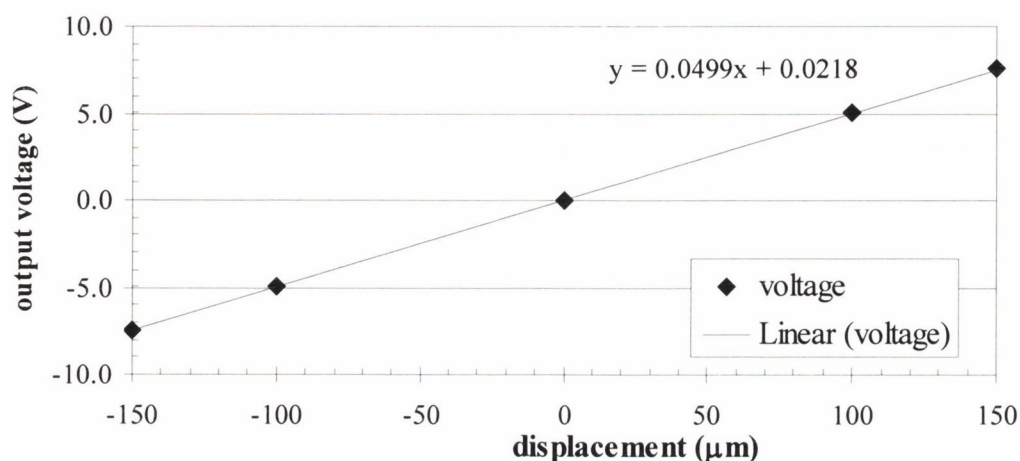| displacement (μm)	output voltage (V)
0	0.000
150	7.531
-150	-7.435
100	5.004
-100	-4.991

Figure A3. Calibration of profilometer.

APPENDIX 3. CALIBRATION OF DYNAMOMETER.

The calibration of the dynamometer was performed by placing weights on top of it and by hanging weights from it and recording the output voltages. As seen from the results in Table A2 and Figure A4, the results were largely linear throughout and a calibration constant (N/V) was calculated.

Table A2. Calibration readings of dynamometer.

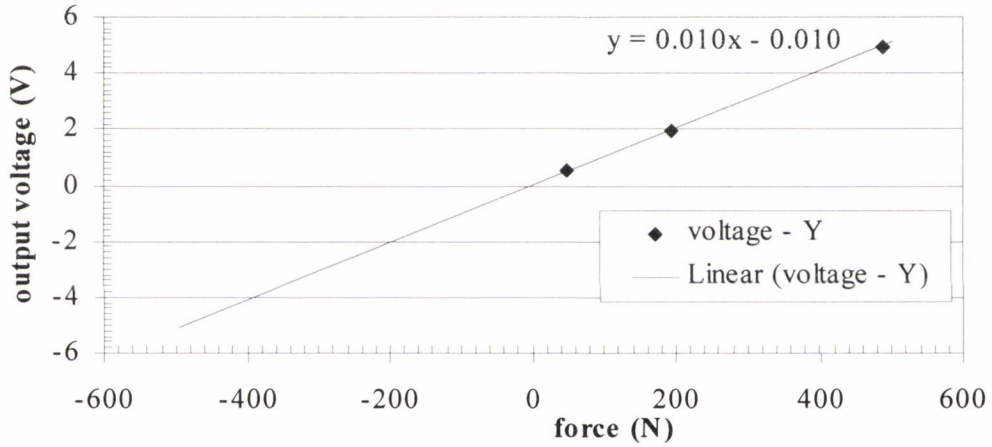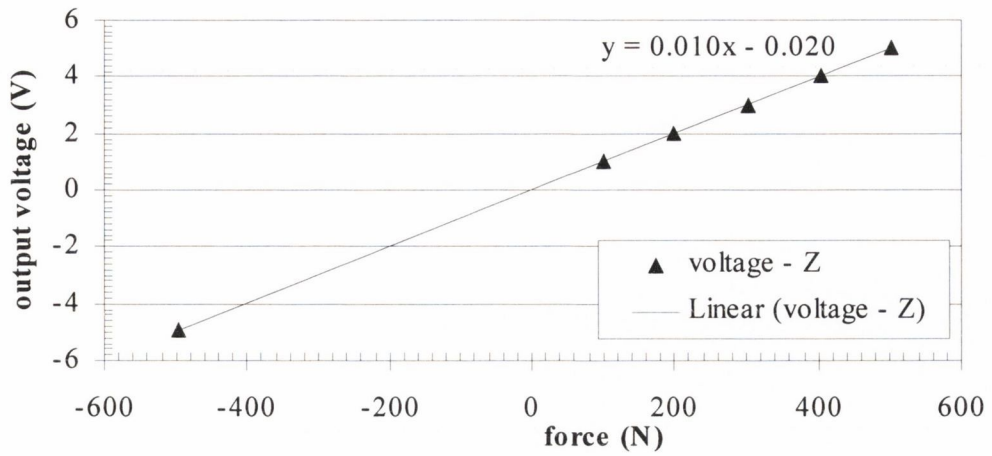| z force (N)	output voltage (V)	y force (N)	output voltage (V)
-495.992	-4.970	49.933	0.500
200.200	1.978	487.150	4.970
101.864	0.997	487.150	4.970
302.605	3.000	487.150	4.970
402.806	4.000	194.694	1.980
503.006	5.000	487.150	4.970

Figure A4. Calibration of dynamometer – normal and tangential forces.

APPENDIX 4. CALIBRATION OF LVDT.

The calibration of the LVDT was performed by displacing it at several incremental distances and measuring the output forces. As seen from the results in Table A3 and Figure A5, the results were largely linear throughout and a calibration constant (mm/volt) was calculated.

Table A3. Calibration readings of LVDT.

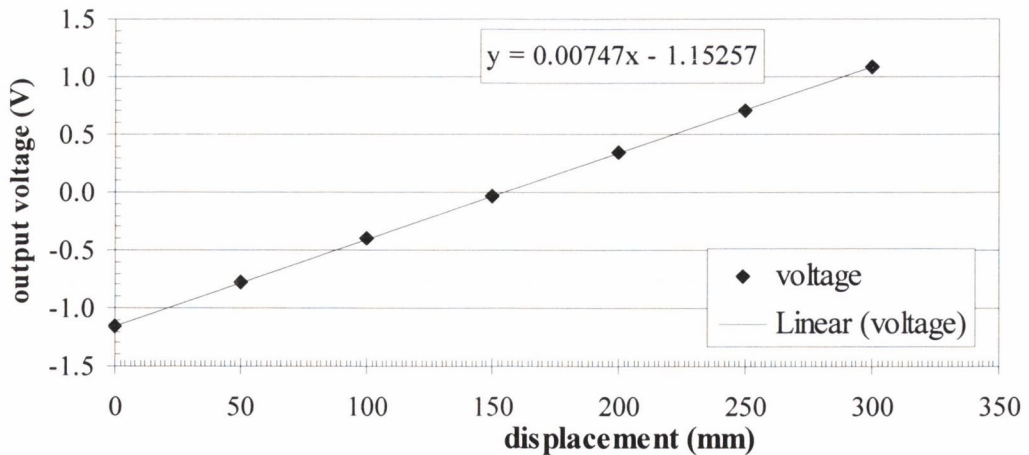| displacement (mm)	output voltage (V)	displacement (mm)	output voltage (V)
0	-1.157	300	1.089
50	-0.776	200	0.341
100	-0.405	100	-0.405
150	-0.034	0	-1.152
200	0.341	300	1.084
250	0.713		

Figure A5. Calibration of LVDT.

APPENDIX 5. A MODEL OF GRIT FRACTURE TO PREDICT WHEEL TOPOGRAPHY.

A5.1. Introduction to Dressing Model.

Vitrified grinding wheels consist of abrasive particles held together by a ceramic glass. Their performance can be partly controlled by varying the size, hardness and strength of the abrasive, by varying the strength of the glass, and by varying the proportions of glassy bond, abrasive and porosity in the wheel [13]. However, for the wheel to function properly, and to achieve optimal performance from the wheel, it must be dressed, usually with single-point diamond tool or rotary tool, to condition the surface. The machine parameters chosen during dressing – most notably dressing lead, dressing depth, the type of dressing tool and the diamond geometry have a significant effect on the performance of the wheel. However, the mechanisms behind the process are not well understood [153].

On approach is the measure the wheel topography– either by stylus methods or optical methods – and to relate the topography of the wheel with empirical grinding tests. Malkin and Cook [17] optically measured percentage wear flat area and correlated it with measured grinding forces. They measured how percentage wear flat area increased with the amount of metal removed in grinding and correlated it with the increase in grinding forces. They found forces increased linearly with percentage wear flat area until reaching a critical value after which they increased rapidly. Suto and Sata [154] measured the worn area and the number of cutting edges, and related these empirically to forces, while Steffens and König [155] calculated grinding chip shape from the measured radii and distribution of cutting edges which they then used as the basis for a simulation of forces and temperature. However, the values obtained depended on the way the wheel was measured which highlighted the experimental difficulties involved in this approach. Other authors have attempted to circumvent the measurement problem to some extent by using a Monte Carlo simulation of the grinding process [156,157,158], but this still requires a cutting edge distribution function which must either be assumed or measured.

Another approach is to predict the topography of the grinding wheel after dressing by either a single point diamond or a diamond roll. Most authors [159,160,6,161] who have modeled single point contact have assumed it to be a cutting process. However, these assumed that the wheel was comprised of ductile material and this assumption is questionable in view of the brittleness of the grinding wheel. The actual mechanisms of material removal are grit and bond fracture. Malkin and Cook [27] found that 50% to 80 % of the wheel volume removed during dressing of 46 grit alumina wheels of G to K grade was by means of dislodgment of entire grains through bond fracture. Other researchers [13,47,162] examining wheel dressing have found brittle fracture to be the dominant mode of wear. Vickerstaff [163] attempted to combine cutting and brittle fracture into a comprehensive dressing model and showed that the path traced by the dressing tool on the wheel is reflected on the work surface. Malkin and Murray [82] showed that fine dressing could produce flat areas on the tips of the grains when the bond was sufficiently strong enough to resist fracture.

The model of abrasion based on Xie and Williams and discussed in this thesis uses as its primary inputs the asperity density and asperity slope as a function of depth into the wheel. These were measured by means of profilometry. In the work presented here, these parameters are predicted from the dressing conditions and wheel properties and are compared to the measured values. These predicted values are then used in the 3-D model of abrasion to predict forces and compared to the measured values from grinding tests.

A5.2. Dressing and Topography.

A5.2.1. A Model of Single-Point Dressing.

If the grits in the wheel are assumed to be on average spherical and randomly distributed in the wheel, the number of grains per unit area (*n*) within the wheel can be written as:

$$n = \frac{3V_g}{2\pi r^2} \qquad (A5)$$

where V_g is the volume fraction of grit in the wheel and r is the average grit radius. As the dressing diamond passes over the surface of the wheel, it will interact with the grits, either crushing them (grit deformation and fracture) or breaking them out of the wheel (bond fracture). By considering the relative strengths of grit and bond, and the geometry of the overlap of the diamond with the grits, it can be shown that a fraction, f_s, should survive on pass of the diamond where:

$$f_s = \frac{1}{2a_d \cdot C^2}\left[1 - \frac{1}{e^{2C^2 a_d}}\right] \qquad (A6)$$

and

$$C = \frac{42\sigma_c r s_d}{F_0 \sqrt{a}} \qquad (A7)$$

where s_d is the dressing lead, a_d is the dressing depth, F_0 the "characteristic strength" of the bond, a the tip radius of the diamond and σ_c the crushing strength of the grit.

The equation for C above indicates that the dressing lead should have a more significant effect than the dressing depth on the wheel sharpness. It also indicates that wheel sharpness should increase as the sharpness of the diamond increases in accordance with experience. In addition, the sharpness is also dependent on the ratio of grit strength to bond strength, and on the values of s_d and a_d in relation to grit size.

However, the final topography will be the result of many dressing passes and if a grit survives the first dressing pass it may be acted upon by a subsequent pass if struck again by the diamond. Under certain circumstances, the diamond may not

strike all the grits on the wheel surface in a pass. Figure A6 shows the cusp-shaped envelope of the diamond's path across the wheel.
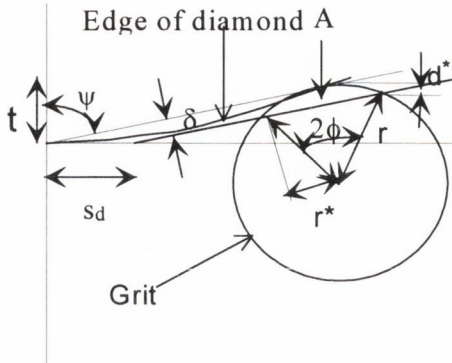

Figure A6. Geometry of diamond and grit.

If the height of a cusp (h) is less than the dressing depth (a_d), all the grits will be struck, so that after j passes, the number of grits per unit area in the wheel surface (n_o) is given by:

$$n_0 = \frac{na_d}{2r} \sum_{j=1}^{j=i} f_s^j \tag{A8}$$

where if $h > a_d$, a fraction f_g of the grits within the compass of the diamond will be missed, and:

$$n_0 = \frac{na_d}{2r} \left[\sum_{j=0}^{j=i-1} \left\{ f(1-f_g) + f_g \right\}^j \right] \tag{A9}$$

with

$$f_g = 1 - \frac{a_d^2}{s_d \cdot a} \tag{A10}$$

172

There is the possibility that raising s_d may decrease the wheel sharpness by increasing f_g. This could explain the conflicting opinions in the literature about the effect of dressing lead [28,29,31], especially since the cases where increasing lead led to decreasing wheel sharpness were for large values of s_d.

The inputs to the 3-D model are the RMS slope versus depth into the wheel and the areal density versus depth into the wheel. The assumption that the grits are randomly distributed within the wheel implies that the grit concentration will rise linearly with depth into the wheel which is also what was found from wheel profiles in the plots of n versus d_w in Section 4.2 (page 86). When d^* is less than h, the number of grits exposed at depth d^* is:

$$n = n_0 + \frac{nd^*}{4r} \tag{A11}$$

$$n = n_0 + \frac{n}{2r}\left(d^* - \frac{h}{2}\right) \tag{A12}$$

when d^* is greater than h.

To get the variation of slope with depth, we assume that when a grit is crushed, its crushed surface will have an RMS slope=s_0; but when it in not crushed, its RMS slope (s_m) will depend on its shape. Using equations (A11) and (A12), we can find the projected area of crushed grits (A_f) and of pointed grits (A_p) as a function of depth. From this, we can show that the slope (s) should vary with depth into the wheel as follows:

$$s = \frac{s_0 A_f + s_m A_p}{A_f + A_p} \tag{A13}$$

In this work, s_0 was set to 0.2 and s_m to 0.6, based upon the arguments given in the next sections.

A5.2.2. Interaction between Grit and Dressing Diamond.

In Figure A6 we have a dressing diamond of semi-angle ψ which interacts with a grit of radius r. The lead is s_d and the dressing depth is a_d. If the diamond just misses the grit on the first pass and if the summit of the grit is a distance a_d above the tip of the dressing tool, then on a second pass it will interact with the grit over an area A as shown. The chord defining A subtends an angle 2ϕ at the center of the grit.

If the diamond tip is circular in section, we can relate ψ to the tip radius and dressing conditions. The equation of the section of the tip of the diamond of radius a can be written:

$$\left(\frac{y}{a}\right)^2 + \left(\frac{x}{a}\right)^2 = 1 \tag{A14}$$

hence,

$$y = \sqrt{a^2 - x^2} \tag{A15}$$

where y=a-a$_d$.

$$\frac{dy}{dx} = \frac{x}{\sqrt{a^2 - x^2}} \tag{A16}$$

$$= \frac{\sqrt{a^2 - y^2}}{y}$$

$$= \sqrt{\left(\frac{a}{y}\right)^2 - 1}$$

$$= \sqrt{\left(\frac{a}{a - a_d}\right)^2 - 1}$$

$$= \cot \psi$$

$$\sin \psi = 1 - a_d/a \tag{A17}$$

$$\cos \psi = \sqrt{\frac{2a_d}{a} - \left(\frac{a_d}{a}\right)^2} \tag{A18}$$

$$\approx \sqrt{\frac{2a_d}{a}}$$

We solve for r^* as follows:

$$\delta = s_d \cos \psi \tag{A19}$$

$$r^* = r \sin \phi \approx \sqrt{2r\delta} = \sqrt{2rs_d \cos \psi} \tag{A20}$$

hence

$$\delta = s_d \cos \psi = \frac{r^{*2}}{2r} \tag{A21}$$

and substituting for ψ.

$$r^* = \sqrt{2rs_d \cos\psi} = \sqrt{2rs_d\sqrt{\frac{2a_d}{a}}} \qquad (A22)$$

moreover:

$$d^* = \delta\sin\psi - \sqrt{2r\delta}\cos\psi = \delta\left(1 - \frac{a_d}{a}\right) - 2\sqrt{\frac{ra_d\delta}{a}} \qquad (A23)$$

A5.2.3. Force on Grit.

If the grit is to crush so that the area A is removed, then the stress a distance r^* from the point of impact must reach the crushing stress for the grit (σ_c). Using Bousssinesq's formula [164] for the stress around a point load, this will give a force F where:

$$F = \frac{\sigma_c x 2\pi r^{*2}}{1-2\nu} \approx 21\sigma_c r^{*2} = 42\sigma_c r\delta \tag{A24}$$

A5.2.4. Statistics of Grit and Bond Fracture.

$$F = 42\sigma_c r l \sqrt{\frac{2a_d}{a}} \tag{A25}$$

For $a_d \ll a$.

where a_d is the interaction depth for a given grit. The statistics of bond fracture follow a Weibull distribution [37], so this gives a probability of fracture:

$$P_f = 1 - \frac{1}{e^{\left(\frac{F}{F_0}\right)^m}} \tag{A26}$$

where F_0 is the characteristic force for the distribution and m the Weibull modulus. The number of grits per unit area struck with an interaction depth between a_d and $a_d + da_d$ is:

$$dn = \frac{n}{2r} da_d \tag{A27}$$

and the number removed dn_r is given by:

$$dn = \frac{n}{2r} da_d \tag{A28}$$

and the number removed dn_r is given by:

$$dn_r = \left[1 - \frac{1}{\exp\left(\dfrac{42\sigma_c r s_d \sqrt{\dfrac{2a_d}{a}}}{F_0}\right)^m} \right] \frac{n}{2r} da_d \tag{A29}$$

Hence, the total number per unit area remaining (n_0) would be:

$$n_0 = n\frac{a_d}{2r} - \frac{n}{2r}\int_0^{a_d}\left[1 - \frac{1}{e^{\left(C\sqrt{2a_d}\right)^m}} \right] da_d \tag{A30}$$

and the fraction remaining of those struck (f_s) is:

$$f_s = 1 - \frac{1}{a_d}\int_0^{a_d}\left[1 - \frac{1}{e^{\left(C\sqrt{2a_d}\right)^m}} \right] da_d \tag{A31}$$

where

$$C = \frac{42\sigma_c r s_d}{F_0 \sqrt{a}} \tag{A32}$$

If $m=2$ (The results of Peklenik *et al.* [37] indicate $m \sim 1.8$ to 1.9),

$$n_0 = n\frac{s_d}{2r} - \frac{n}{2r}\left[a_d + \frac{1}{4C^2}\left(\frac{1}{e^{2C^2 a_d}} - 1 \right) \right] \tag{A33}$$

178

$$f_s = \frac{2rn_0}{na_d} = \frac{1}{2a_dC^2}\left(1 - \frac{1}{e^{2C^2a_d}}\right) \tag{A34}$$

for the first dressing pass, f_s being the fraction of grits actually struck which remain.

A5.2.5. Grits/mm^2 Against Scratch Depth.

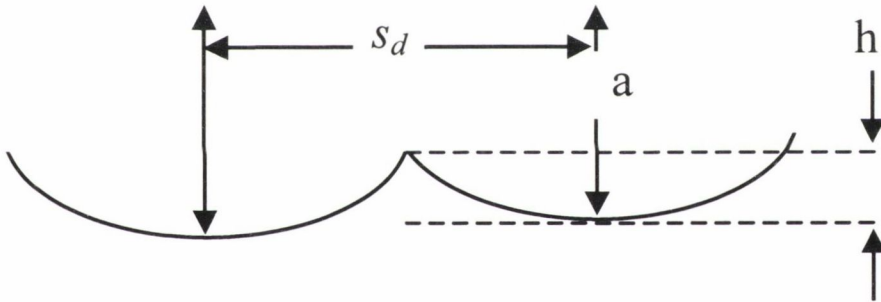How the dressing diamond leaves a track on the wheel surface is shown in Figure A7.

Figure A7. Dressing diamond track on wheel surface.

The height h of the peaks is given by:

$$h = \sqrt{s_d a} \tag{A35}$$

To calculate how the number of grits per mm^2 changes with depth into the wheel, we note first that we must sum the effects of repeated dressing passes on the grits. The first case is when h is less than a_d. Each grit which survives a particular pass will be subject to the following pass. If a grit suffers j passes, it will have a chance of

survival f_s^j. The number of grits, crushed and remaining in the surface layer of the wheel after i passes is therefore:

$$n_0 = \frac{na_d}{2r} \sum_{j=1}^{j=i} f_s^j \qquad \text{(A36)}$$

Raising s_d has a powerful effect on n_0 and the wheel sharpness.

However, if h is greater than t_m, the diamond will miss a fraction f_g of the grits which are within its compass, where:

$$f_g = 1 - \frac{a_d^2}{s_d a} \qquad \text{(A37)}$$

This leads to a different equation for n_0:

$$n_0 = \frac{na_d}{2r} \left[\sum_{j=0}^{j=i-1} \{ f(1 - f_g) + f_g \}^j \right] \qquad \text{(A38)}$$

Raising s_d may now decrease the wheel sharpness by increasing f_g. When d^* is less than h, the number of grits exposed at depth d^* is:

$$n_d = n_0 + \frac{nd^*}{4r} \qquad \text{(A39)}$$

When d^* is greater than h, the number of grits exposed at depth d^* is:

$$n_d = n_0 + \frac{n}{2r} \left(d^* - \frac{h}{2} \right) \qquad \text{(A40)}$$

A5.2.6. Slope Distributions.

The grains in a polycrystal tend to take the shape of a tetrakaidekahedron [146], where the corner included angle is 120°. A perfectly sharp tetrakaidekahedron would therefore have an attack angle of 30° on average. If the grain is crushed by the dressing tool, it will then have a different slope on the crushed part which will depend on the grit type. For 60 grit H grade white alumina wheels, measurements have found that for all dressing conditions the RMS slope at the outermost points of the wheel is around 0.2 (Section 4.2.4, page 92). Taking this slope as the slope when the grits are crushed fits the results well when we use a value of $F_0 = 48$ N [37] and a value of $\sigma_c = 528$ MPa [152].

To find the average slope down to a depth d, we must calculate a weighted average of the two mean slopes above, weighted by the area of grit in contact. When the grit is crushed, its top will be flattened to a circle of radius between 0 and r^*. The average area of the flats is therefore:

$$a_f = \pi \left(\frac{2}{3} r^* \right)^2 \tag{A41}$$

These grits are actually spread over a depth 0-δ beneath the surface.

If $d < \delta$,

$$A_f = n_0 \frac{d}{\delta} \frac{4}{9} \pi r^{*2} \tag{A42}$$

If $d > \delta$,

$$A_f = n_0 \frac{4}{9} \pi r^{*2} \tag{A43}$$

The area of pointed grits is given by:

$$A_p = \frac{d}{2r}(n - n_0)\pi\left(\frac{2}{3}\sqrt{2rd}\right)^2 = \frac{4}{9}\pi d^2(n - n_0) \tag{A44}$$

The average slope s is then given by:

$$s = \frac{s_0 A_f + s_m A_p}{A_f + A_p} \tag{A45}$$

A5.2.7. Roughness.

The scratch shape produced by a pyramidal grit is shown in Figure A8. As shown in the main text, the efficiency is then
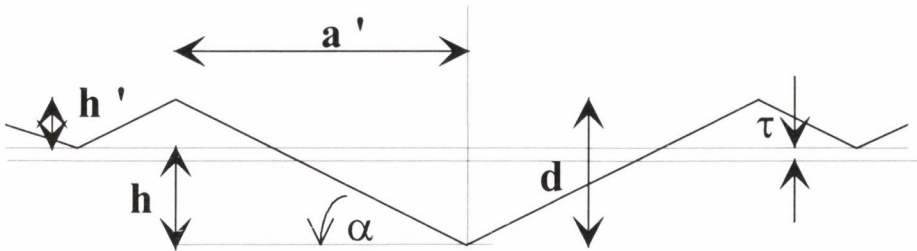
$$e = \frac{K \tan\alpha}{H_s} \tag{A46}$$

Figure A8. Scratch made by pyramidal indenter.

The amount of material per unit width removed by an array of contiguous scratches like that in the figure is given by:

$$A_s = \frac{ed^2}{\tan\alpha}\frac{\tan\alpha}{2(h'+d)} = \frac{ed^2}{2(h'+d)} \qquad (A47)$$

so the number of times this must be repeated to remove a depth d is given by;

$$N_s = \frac{2(h'+d)}{ed} \qquad (A48)$$

The height, h' is also related to the efficiency.

$$e = \frac{\dfrac{h^2}{\tan\alpha} - \dfrac{2h^2}{\tan\alpha}}{\dfrac{d^2}{\tan\alpha}} \qquad (A49)$$

$$= \frac{(d - h') - 2h'^2}{d^2}$$

$$= -\left(\frac{h'}{d}\right)^2 - 2\left(\frac{h'}{d}\right) + 1$$

$$\left(\frac{h'}{d}\right) = \sqrt{2 - e} - 1 \tag{A50}$$

To get the roughness, we need to find the mean line of an array of scratches such as those in the figure.

$$\text{Area above the mean line} \quad = \frac{1}{\tan \alpha}\left(2h'^2 + 4h'\tau + \tau^2\right) \tag{A51}$$

$$= \frac{1}{\tan \alpha}\left(d - \left(h' + \tau\right)^2\right)$$

Equating:

$$2h'^2 + 4h'\tau + \tau^2 \qquad = d^2 - 2\left(h' + \tau\right)d + \left(h' + \tau\right)^2 \tag{A52}$$

$$= d^2 - 2dh' - 2d\tau + h'^2 + 2h'\tau + \tau^2$$

$$h'^2 + 2h'\tau + +2d\tau + 2dh' - d^2 = 0 \tag{A53}$$

$$2\tau\left(h' + d\right) = d^2 - h'^2 - 2dh' \tag{A54}$$

$$\tau = \frac{d^2 - h'^2 - 2dh'}{2\left(h' + d\right)} \tag{A55}$$

Equations (A46) to (A55) can now be used to find R_a, noting that the effect of N_s scratches over the same area is to reduce the roughness as $\sqrt{N_s}$ [165].

$$R_a \qquad = \frac{\left(h' + \tau\right)}{2\sqrt{N_s}} \tag{A56}$$

$$= \frac{\left(h' + \tau\right)}{2\sqrt{\dfrac{2\left(h' + d\right)}{ed}}}$$

$$= \frac{\left(h' + \tau\right)}{2}\sqrt{\frac{ed}{2\left(h' + d\right)}}$$

A5.2.8. Workpiece Roughness.

With the grinding mechanics model that has been assumed with the pyramid-shaped asperity, the grits will leave triangular scratches in the workpiece as shown in Figure A8. To get the roughness of the workpiece as a function of scratch depth d, we first need to find a relationship between d and h', which is related to the efficiency e as follows:

$$\frac{h'}{d} = \sqrt{2-e} - 1 \tag{A57}$$

We next need to find τ, the distance of the mean line of an array of scratches such as those in the figure below the top of the side ridges. This is given by:

$$\tau = \frac{d^2 - h'^2 - 2dh'}{2(h' + d)} \tag{A58}$$

For an array of such scratches, the surface roughness will then be given by:

$$R_a = \frac{(h' + \tau)}{2} \tag{A59}$$

However, for a depth d to be removed from the workpiece, this pattern of scratches must be repeated N_s times where:

$$N_s = \frac{2(h' + d)}{ed} \tag{A60}$$

If the scratches are superimposed randomly, this will lead to a reduction in the roughness proportional to $\sqrt{N_s}$, so that:

$$R_a = \frac{(h' + \tau)}{2\sqrt{N_s}} = \frac{(h' + \tau)}{2\sqrt{\dfrac{2(h' + d)}{ed}}} = \frac{(h' + \tau)}{2}\sqrt{\frac{ed}{2(h' + d)}} \qquad\qquad \text{(A61).}$$

A5.3. Predictions and Experiments.

A5.3.1. Predictions of Wheel Topography.

The model of dressing was applied to the grinding experiments performed in the main section of the thesis for Set 1 – Vitrified Alumina wheel with EN31 workpieces. The tip radius of the diamond was measured using a coordinate microscope yielding a tip radius of 0.46 mm. This was used in the model for the characteristic diamond tip radius a. The experimental values of asperity density and asperity slope were used from the profilometry results discussed in the Section 4.2 (page 86). The further parameters required by the dressing model were calculated from the wheel specification using the data of Peklenik *et al.* [37] on bond strength and that of Brecker [152] on grit strength. Then the wheel topography was predicted for each of the dressing conditions employed. The results are shown in the three figures below (Figure A9., Figure A10. and Figure A11). For the fine dressing condition, the predictions of grit density agree well with the measurements, but the agreement for slope is not so good overall. For the medium and coarse conditions, the reverse is the case. However, in all cases, the predictions of both slope and grit density are best close to the wheel surface, which is the active part of the wheel. There are two possible reasons for the deviation between the theoretical and measured grit densities at larger depths. Firstly, the dressing model assumes that only single grits are broken from the surface, whereas there is always the possibility that two or more grits might be broken out by a sufficiently strong impact with the dressing tool. Secondly, there is the possibility that the grit density deduced from the profile may be an underestimate for the reasons already given. However, the agreement in the active part of the wheel is good enough to hold out the possibility of good prediction of force and roughness.
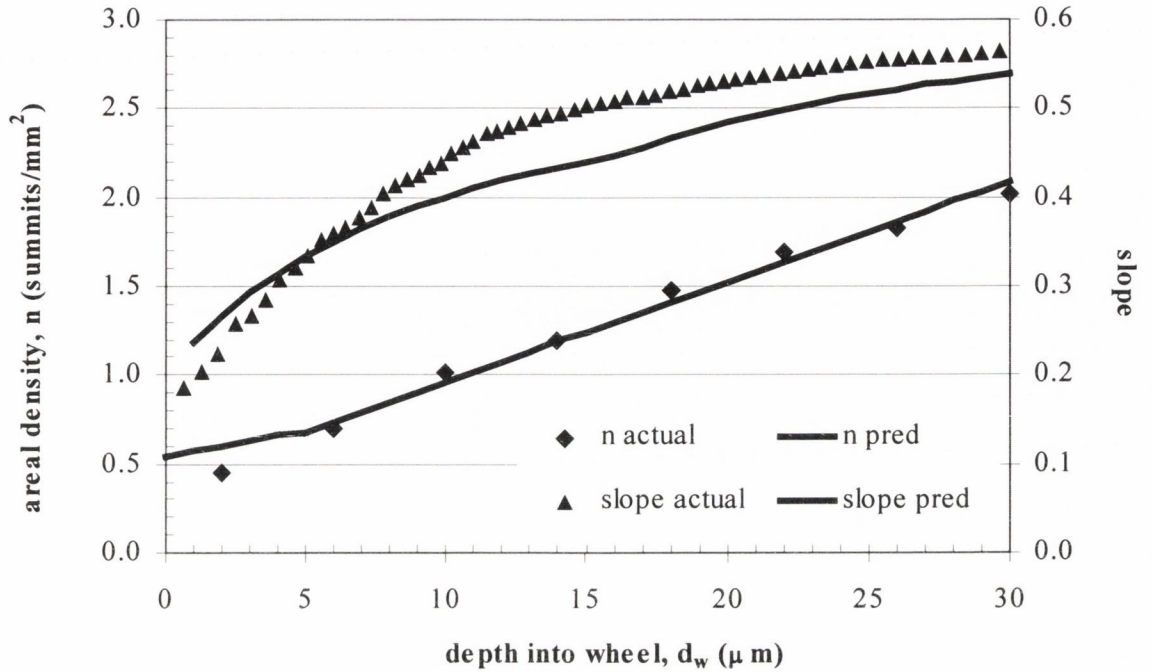
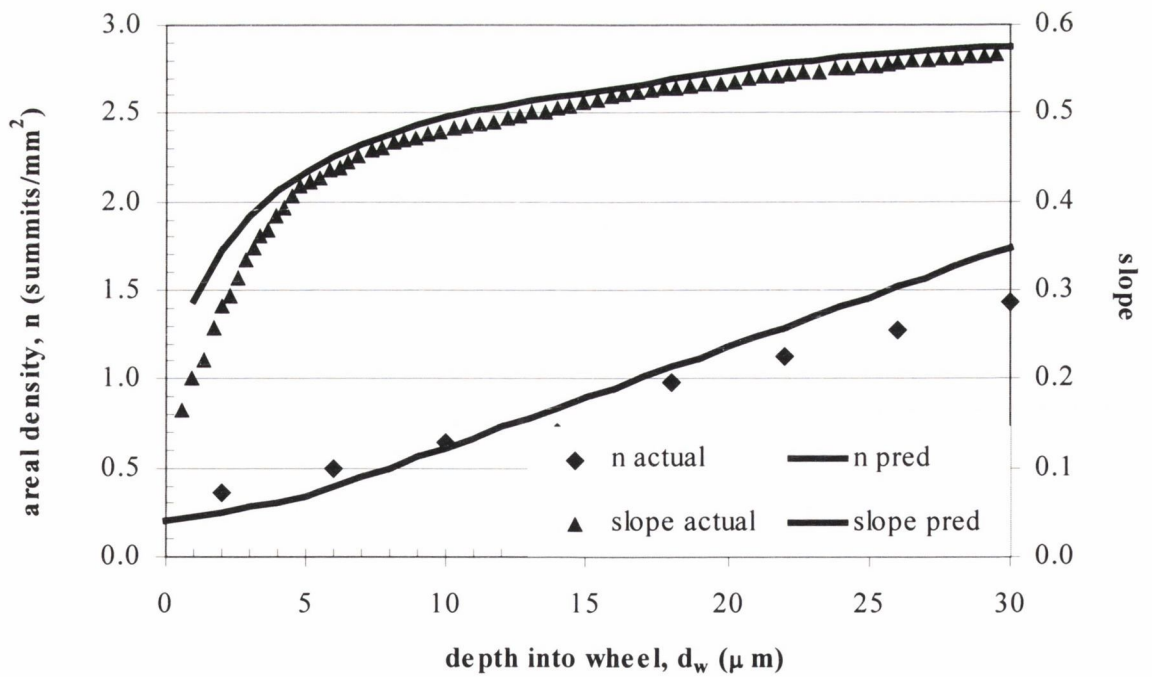Figure A9. Predicted and measured values for fine dressing.

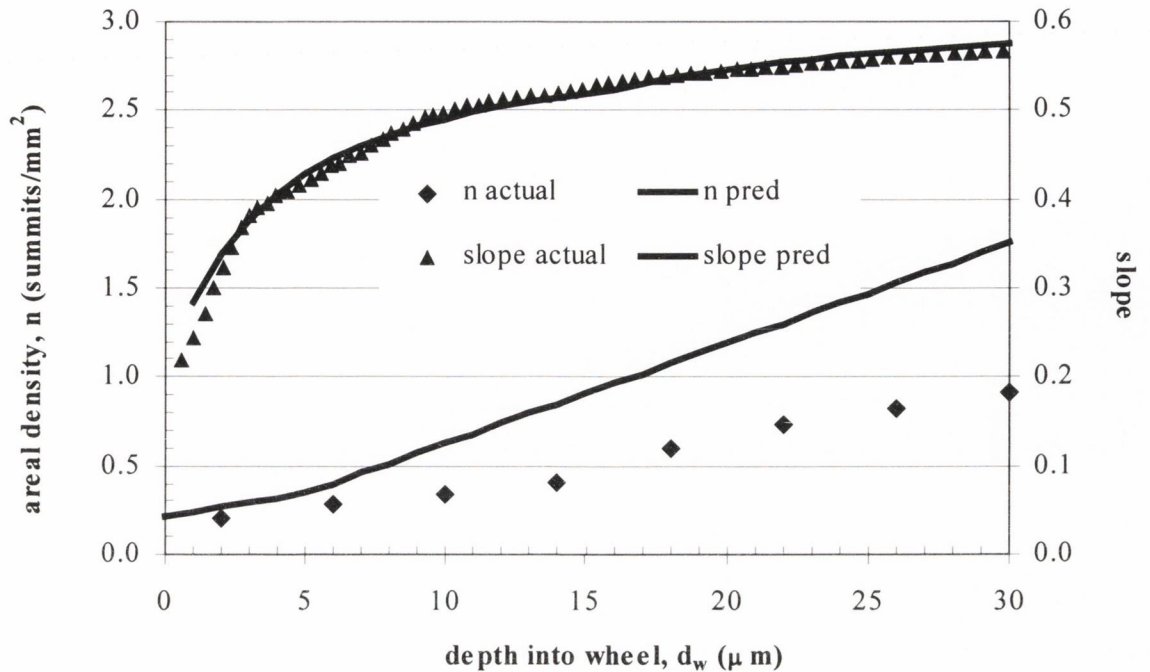Figure A10. Predicted and measured values for medium dressing.

Figure A11. Predicted and measured values for coarse dressing.

A5.3.2. Prediction of Grinding Forces.

For each of the three dressing conditions used in the experiments with the vitrified alumina wheel, the dressing model was applied with the dressing parameters used to predict the asperity density and slope distributions along with surface roughness values. These, in turn, were used in the 3-D Xie and Williams model in lieu of the measured profiles and force predictions were made using these predicted values from the dressing model. Last, the forces predicted with the dressing model were compared to the forces measured during grinding tests.

Results of the force predictions using the predicted slope and asperity density values applied to Xie and Williams's 3-D model are shown in the three figures below.
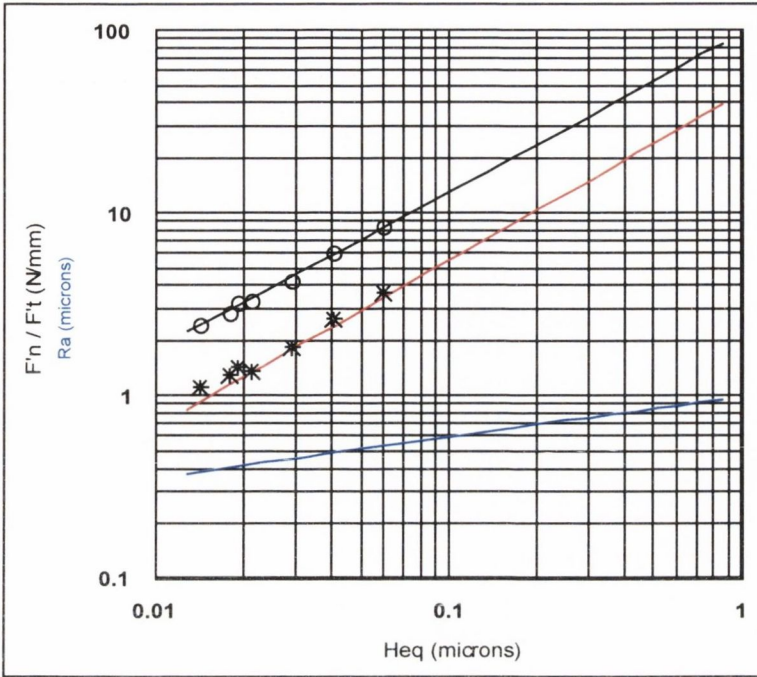
Figure A12. Predicted and measured forces for fine dress.

Predicted	Dressing Conditions
μ=0.42	a = 0.92 mm
$\dot{f}$=0.89	a_d = 5 μm
F_1 = 43.1 N/mm	s_d = 200 μm
$e_{0.1}$ = 56 J/mm^3	

At low metal removal rates, the theoretical curves predict the experimental results very well, but as h_{eq} rises, the tangential forces tend to be lower than predicted by up to 10% at the highest metal removal rates. The scratch depth, d, is then quite high (12-15 μm), and there is a considerable difference between the predicted and measured wheel topography. Also, at the higher metal removal rates, the wheel will wear faster; its topography will change, and force predictions made from the original dressed topography may not be so reliable.
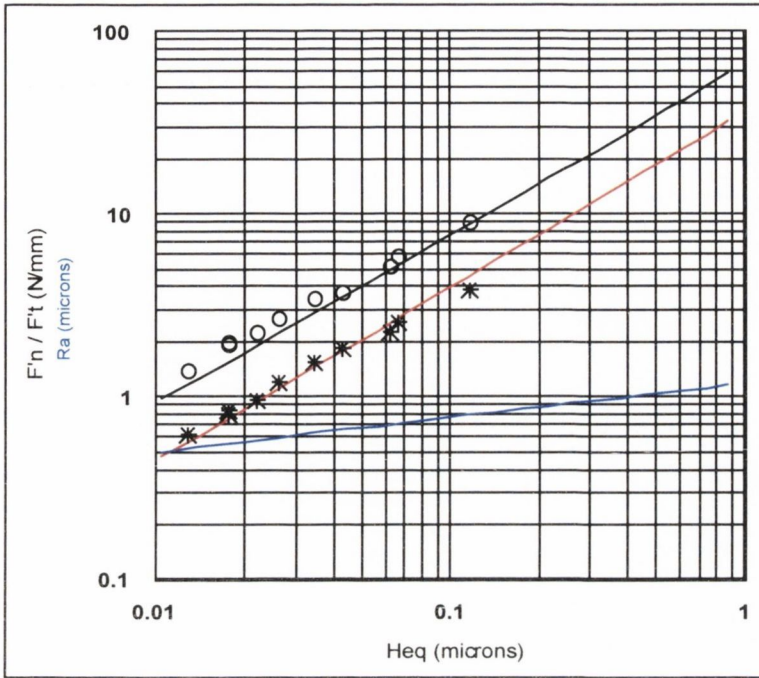
Figure A13. Predicted and measured forces for medium dress.

Predicted	Dressing Conditions
$\mu = 0.51$	$a = 0.92$ mm
$f = 0.93$	$a_d = 30$ μm
$F_l = 33.2$ N/mm	$s_d = 200$ μm
$e_{0.1} = 39$ J/mm^3	

191
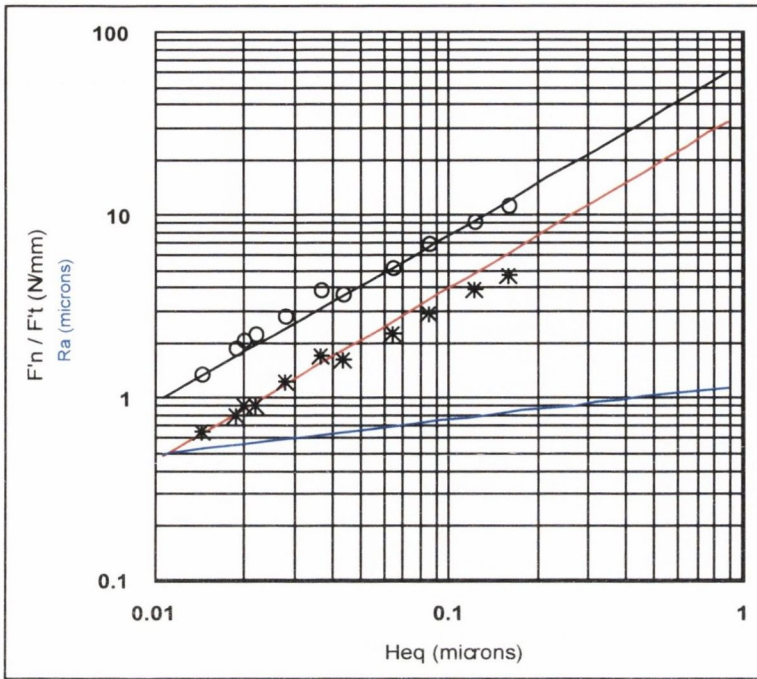
Figure A14. Predicted and measured forces for coarse dress.

Predicted	Dressing Conditions
$\mu=0.5$	$a = 0.92$ mm
$f'=0.92$	$a_d = 60\ \mu m$
$F_l = 33.5$ N/mm	$s_d = 200\ \mu m$
$e_{0.1} = 40$ J/mm^3	

A5.4. Discussion.

As a first step towards the prediction of the performance of the grinding process, the results reported here are quite encouraging. Treating the dressing of the grinding wheel as a statistical process of brittle fracture seems to be a successful way of predicting wheel topography, and provided the dressing process is not too heavy, the simplified approach presented here gives good results. However, it is clear that a more refined theory may be needed to account for the more complex interactions which could occur when the dressing tool strikes the abrasive grits more firmly. It is also clear that a complete theory of grinding would normal have to account for the wear of the grinding wheel and the way this would change its topography. It may be possible to extend the statistical fracture mechanism proposed here for dressing to

this question as well, but such a development is beyond the scope of this present paper.

Considering the difference between the two processes, and the uncertainty of some of the values used in the calculations, the agreement is quite good, and gives us encouragement that the model described here may, with suitable inputs, be able to predict grinding performance over a wide range of conditions. Even without improved data for the inputs it requires, it is still able to show the likely effect on grinding performance of altering the various parameters at one's disposal, and in this respect, could be a useful tool for process planning.

Further progress could be made if better data on the fracture properties of grit sand bonds and more accurate data on the frictional properties of coolant could be obtained. Moreover, it would be relatively simple to combine the force predictions given here with models of the temperature in the arc of cut to define grinding conditions which will avoid metallurgical damage of the workpiece.

Potentially, the model proposed here could account for the effects of all variables (wheel, work, machine settings, dressing and coolant) in the grinding process on the forces and roughness, but there is not enough fundamental data available yet for this to be done.

A5.5. Conclusions.

1. A model of the dressing process, based on the statistics of brittle fracture has been proposed. It is successful in prediction the topography of the wheel which results from single point diamond dressing, and in combination with a model of abrasive wear, can predict successfully forces and workpiece roughness in grinding.

2. The model can be used to evaluate quickly the likely effects of changing machine settings, dressing conditions, wheel grade, coolant *etc* on the grinding forces and roughness of the workpiece.

3. There is much scope for improving the predictions of the model through better measurement of the fracture properties of the grit and bond, and of the lubricating properties of the coolant.